

LIMITED DISTRIBUTION

P-109  
NASA CR-179521  
R86AEB564



National Aeronautics and  
Space Administration

# **E<sup>3</sup> 10C COMPRESSOR TEST ANALYSIS OF HIGH-SPEED POST-STALL DATA**

by

**S.D. Dvorak  
W.M. Hosny  
W.G. Steenken**

**General Electric Company**

**Prepared for**

**National Aeronautics and Space Administration**

(NASA-CR-179521) E3 10C COMPRESSOR TEST  
ANALYSIS OF HIGH-SPEED POST-STALL DATA  
(General Electric Co.) 109 F CSCI 21E

N88-28929

G3/07 0164893  
Unclas

al,  
ler  
a  
is  
is  
of

Date for general release: October, 1988.

**NASA-Lewis Research Center  
Contract NAS3-24211  
October 1986**

## FOREWORD

The program described in this report was conducted by the Aircraft Engine Group of the General Electric Company, Cincinnati, Ohio, for the NASA Lewis Research Center, National Aeronautics and Space Administration under contract NAS3-24083.

The program was carried out under the technical cognizance of Mr. R. D. Hager of the NASA Lewis Research Center Turbine Engine Branch.

The contract effort was conducted at the Evendale Plant of the Aircraft Engine Group, Cincinnati, Ohio, under the technical management of Dr. W. G. Steenken with Mr. S. D. Dvorak being the prime technical contributor.

The technical support and direction provided by Dr. W. M. Hosny, as well as the expertise and contributions to the parameter estimation effort by Dr. J. H. Taylor of General Electric Corporate Research and Development are gratefully acknowledged.

Support was also provided by Mrs. H. T. Hogg in preparing the manuscript and Mrs. M. A. Banks in preparing the figures.

## TABLE OF CONTENTS

<u>Section</u>	<u>Page</u>
LIST OF FIGURES	v
LIST OF TABLES	xi
NOMENCLATURE	xiii
1.0 SUMMARY	1
2.0 INTRODUCTION	3
3.0 TEST INSTRUMENTATION	5
3.1 Airflow Rakes	5
3.2 ZOC System	11
4.0 AIRFLOW RAKE DATA REDUCTION	13
4.1 Digitization Hardware and Software Description	13
4.2 Data Reduction and Calibration Procedure	13
4.2.1 Electrical Calibration	14
4.2.2 Engineering Unit Calibration	14
5.0 AIRFLOW CALCULATIONS	17
5.1 Airflow-Calculation Procedure	17
5.2 Compressor Dynamic Response	18
5.3 Digital Filtering Techniques	28
6.0 COMPRESSOR CHARACTERISTICS IDENTIFICATION	37
6.1 Background	37
6.2 Estimation Model	39
6.2.1 Pressure Coefficient Estimation Model	41
6.2.2 Work Coefficient Estimation Model	42

PRECEDING PAGE BLANK NOT FILMED

## TABLE OF CONTENTS (Concluded)

<u>Section</u>	<u>Page</u>
6.3 Pressure Coefficient Estimation	44
6.4 Work Coefficient Estimation	52
7.0 COMPUTER MODEL SIMULATION	55
7.1 Model Description	55
7.2 Low Speed Test and Modelling Results	57
7.3 High Speed Modelling Results	65
8.0 CONCLUSIONS AND RECOMMENDATIONS	71
APPENDIX	
A. High Speed Post-Stall Transients	73
REFERENCES	87

## LIST OF FIGURES

<u>Figure</u>		<u>Page</u>
1	Plane 25 Transient Airflow Rake.	6
2	Plane 31 Transient Airflow Rake.	7
3	Dynamic Instrumentation Locations	8
4	Plane 31 Rake Position.	9
5	Airflow Rake Cross Sections.	10
6	Face Average Pressure Ratio, 98.5% $N_c$ Stall Inception.	20
7	Face Average Inlet Corrected Airflow Rate, 98.5% $N_c$ Stall Inception.	20
8	Operating Point Migration, 98.5% $N_c$ Stall Inception.	21
9	Test Facility Schematic	22
10	Compressor Inlet Total Temperature, 98.5% $N_c$ Stall Inception.	23
11	Compressor Corrected Speed, 98.5% $N_c$ Stall Inception.	23
12	Tip Operating Point Migration, 98.5% $N_c$ Stall Inception.	24
13	Hub Operating Point Migration, 98.5% $N_c$ Stall Inception.	24
14	Operating Point Migration, 98.5% $N_c$ Quasi-Steady Surge Cycles for $1.8 < \text{Time} < 3.6$ Seconds.	25
15	Inlet Corrected Airflow, 98.5% $N_c$ Quasi-Steady Surge Cycles.	26
16	Inlet Total Pressure, 98.5% $N_c$ Quasi-Steady Surge Cycles.	26

## LIST OF FIGURES (Continued)

<u>Figure</u>		<u>Page</u>
17	Exit Total Pressure, 98.5% $N_c$ Quasi-Steady Surge Cycles.	27
18	Inlet Total Temperature, 98.5% $N_c$ Quasi-Steady Surge Cycle.	27
19	Unfiltered Inlet Total Pressure Kulite Signal (PX25SW), 90% $N_c$ Instability.	29
20	Unfiltered Inlet Total Pressure Kulite (PX25SW), 90% $N_c$ Instability.	29
21	Power Spectrum of Unfiltered PX25SW with First Order Trend Removed, 90% $N_c$ Instability.	30
22	Inlet Corrected Airflow Calculated from Unfiltered PX25SW and PX2ASW, 90% $N_c$ Instability.	31
23	Power Spectra of Unfiltered and Filtered Inlet Total Pressure Kulite (PX25SW), 90% $N_c$ Instability.	33
24a	A Comparison of Inlet Airflow Calculated from Unfiltered and Filtered Pressure Measurements, 90% $N_c$ Instability.	34
24b	Power Spectra of Inlet Airflow Calculated from Unfiltered and Filtered Pressure Measurements, 90% $N_c$ Instability.	34
25a	A Comparison of Inlet Airflow Calculated from Filtered Pressure Measurements and Filtered Airflow, 90% $N_c$ Instability.	35
25b	Power Spectra of Inlet Airflow Calculated from Filtered Pressures and Filtered Airflow, 90% $N_c$ Instability.	35
26	Compressor Estimation Model	40
27	Input Signals for Work Coefficient Estimation.	43

## LIST OF FIGURES (Continued)

<u>Figure</u>		<u>Page</u>
28	A Comparison Between the 98.5% $N_c$ Estimated Pressure Coefficient and 75% $N_c$ Test Data.	45
29	Pressure Coefficient Estimation Models, 98.5% $N_c$ .	47
30	Histogram of In-Stall Flow Coefficient, 98.5% $N_c$ .	48
31	Measured Parameters Used in 90% $N_c$ Pressure Coefficient Estimation.	49
32	Histogram of In-Stall Flow Coefficient, 90% $N_c$ .	50
33	Pressure Coefficient Estimation Models, 90% $N_c$ .	51
34	A Comparison of Actual and Reconstructed Instantaneous Pressure Coefficient, 90% $N_c$ .	53
35	Work Coefficient Estimation Model, 90% $N_c$ .	54
36	Compressor Rig Model Geometry.	56
37a	Stall Inception Time Constants.	58
37b	Stall Recovery Time Constants.	58
38	Compressor Characteristics, 75% $N_c$ .	59
39	Stall Development, 75% $N_c$ Test Data.	61
40	Operating Point Migration, 75% $N_c$ Stall Inception, Model Data.	62
41	Inlet and Exit Pressure, 75% $N_c$ Stall Inception, Model Data.	64
42	Compressor Characteristics, 98.5% $N_c$ .	66
43	Operating Point Migration, 98.5% $N_c$ Stall Inception, Model Data.	67

## LIST OF FIGURES (Continued)

<u>Figure</u>		<u>Page</u>
44	Inlet and Exit Pressure, 98.5% $N_c$ Stall Inception, Model Data.	68
45	Compressor Inlet Pressure, 90% $N_c$ Instability.	74
46	Compressor Inlet Corrected Airflow, 90% $N_c$ Instability.	74
47	Compressor Inlet Temperature, 90% $N_c$ Instability.	75
48	Compressor Inlet Physical Airflow, 90% $N_c$ Instability.	75
49	Compressor Exit Pressure, 90% $N_c$ Instability.	76
50	Compressor Exit Corrected Airflow, 90% $N_c$ Instability.	76
51	Compressor Exit Temperature, 90% $N_c$ Instability.	77
52	Compressor Exit Physical Airflow, 90% $N_c$ Instability.	77
53	Compressor Inlet Pressure, 95% $N_c$ Instability.	78
54	Compressor Inlet Corrected Airflow, 95% $N_c$ Instability.	78
55	Compressor Inlet Temperature, 95% $N_c$ Instability.	79
56	Compressor Inlet Physical Airflow, 95% $N_c$ Instability.	79
57	Compressor Exit Pressure, 95% $N_c$ Instability.	80
58	Compressor Inlet Pressure, 95% $N_c$ Instability, Stators Open 5°.	81

LIST OF FIGURES (Concluded)

<u>Figure</u>		<u>Page</u>
59	Compressor Inlet Corrected Airflow 95% $N_c$ Instability, Stators Open 5°	81
60	Compressor Inlet Temperature, 95% $N_c$ Instability, Stators Open 5°.	82
61	Compressor Inlet Physical Airflow, 95% $N_c$ Instability, Stators Open 5°.	82
62	Compressor Exit Pressure, 95% $N_c$ Instability, Stators Open 5°.	83
63	Compressor Inlet Pressure, 98.5% $N_c$ Instability.	84
64	Compressor Inlet Corrected Airflow, 98.5% $N_c$ Instability.	84
65	Compressor Inlet Temperature, 98.5% $N_c$ Instability.	85
66	Compressor Inlet Physical Airflow, 98.5% $N_c$ Instability.	85
67	Compressor Exit Pressure, 98.5% $N_c$ Instability.	86



# LIST OF TABLES

<u>Table</u>		<u>Page</u>
1	Instability Events.	18
2	A Comparison of Model and Test Steady-State Data Points, 75% $N_c$ Stall.	63

PRECEDING PAGE BLANK NOT FILMED

xi

PAGE X INTENTIONALLY BLANK

## NOMENCLATURE

A	-	Area
$\underline{A}$	-	Linear Dynamic System Matrix
$\underline{B}$	-	Linear Dynamic System Input Matrix
$\underline{C}$	-	Linear Dynamic System Output Matrix
$C_p$	-	Specific Heat at Constant Pressure
$\underline{D}$	-	Linear Dynamic Input-Output Matrix
$F_z$	-	Axial Force
g	-	Gravitational Constant
J	-	Joule's Constant
L	-	Volume Length
M	-	Mach Number
$N_c$	-	Corrected Speed
P	-	Pressure
$q^{-1}$	-	Delay Operator
R	-	Gas Constant
S	-	Entropy
s	-	Estimation Model Input
T	-	Temperature
t	-	Time
U	-	Mean Rotor Velocity
$\underline{u}$	-	Input Vector
V	-	Volume
V	-	Loss Function
v	-	Measurement Error

## NOMENCLATURE (Continued)

$W$	-	Airflow
$\underline{w}$	-	Process Disturbance Vector
$\underline{x}$	-	Linear Dynamic System State Vector
$y$	-	Dynamic System Output
$\gamma$	-	Specific Heat Ratio
$\delta$	-	Standard Day Pressure Correction Factor
$\epsilon$	-	Output Error
$\theta$	-	Parameter Estimate Vector
$\theta$	-	Standard Day Temperature Correction Factor
$\rho$	-	Density
$\sigma$	-	Standard Deviation
$\tau$	-	Time Constant
$\phi$	-	Flow Function
$\psi'$	-	Pressure Coefficient
$\Psi$	-	Work Coefficient

### Subscripts

$k$	-	Discrete Time Step
QS	-	Quasi-Steady
s	-	Static
t	-	Total
o	-	Standard Condition
1	-	Volume Inlet
2	-	Volume Exit
25	-	Compressor Inlet
31	-	Compressor Diffuser Exit

## 1.0 SUMMARY

The overall effort described in this report was to obtain high-speed post-stall compressor characteristics from actual transient test data. To this end, the NASA Energy Efficient Engine (E<sup>3</sup>) compressor was tested to obtain both low and high speed in-stall data. This report describes the instrumentation, data reduction, and estimation procedures necessary to obtain the high-speed post-stall characteristics from transient (surge cycle) data.

In-stall characteristics were obtained from post-surge transients for two high-speed conditions, 90 and 98.5 percent corrected speed, using maximum likelihood parameter estimation techniques. The 90 percent speed transient contained sufficient data during which the compressor inlet airflow was reversed such that estimates of compressor characteristics in the reverse flow regime were also obtained.

The estimates of the in-stall characteristics were found to be insensitive to the presence of test facility-induced dynamics which influenced the nature of the post-stall transients. However, the estimates of the compressor dynamic response time constants were found to be sensitive to these parasitic dynamics.

In an effort parallel to the testing and data analysis, a computer model to simulate the E<sup>3</sup> compressor both in stalled and unstalled operation was developed. This model proved capable of simulating the different types of compressor instability, namely rotating stall and surge, which occur at low and high speed, respectively.

## 2.0 INTRODUCTION

As the performance of high-pressure-ratio, high-speed aircraft engine axial-flow compressors increases, the penalties paid in off-design performance often increase as well. One of these penalty areas is often found to be stall recoverability. Therefore, as compressor designs improve, it is necessary to examine the effects of increased performance on post-stall performance.

Analyzing and understanding compressor instability and recoverability requires the development of detailed analytical models. These computer models should be able to simulate the components and engine system during post-stall transient operation. General Electric has recognized the need for improving these computer models, extending their capabilities, and developing test and data acquisition techniques to validate them.

The success of such models depends upon proper representation of the compressor in-stall characteristics. Previously, compressor models have used in-stall characteristics determined from low-speed research compressor data which were adjusted to reflect higher speeds, pressure ratios, and airflows. However, advances in compressor design have resulted in high-speed, highly-loaded compressors, the unstable behavior of which is difficult to correlate to low-speed in-stall data.

For this reason, this present effort was undertaken to obtain low-speed and high-speed post-stall data from the NASA Energy Efficient Engine (E<sup>3</sup>) compressor, a high-speed, high-pressure ratio machine which not only represents the latest advances in compressor design, but also embodies trends in compressor design which are likely to continue. Therefore, computer models based on the in-stall characteristics of the E<sup>3</sup> compressor should provide a more accurate representation of post-stall behavior and recoverability of current and future compressor designs.

The E<sup>3</sup>-10C compressor was tested in General Electric's Full Scale Compression Test Facility located in Lynn, Massachusetts. The E<sup>3</sup>-10C compressor configuration and testing are documented in Reference 1. Also in Reference 1 are results of in-stall testing in which the low-speed (50 to 75 percent corrected speed) in-stall characteristics were obtained from steady-state, rotating-stall instabilities. In this study, that effort is extended to obtain the high-speed (90 to 98.5 percent corrected speed) in-stall characteristics from post-stall transient (surge) data.

It has been found that more traditional methods of obtaining and reducing data, while useful in determining low-speed rotating-stall characteristics, are inadequate in determining the high-speed in-surge characteristics. For this reason, the use of system identification has been pursued. In this report, a procedure for using maximum likelihood parameter estimation theory (MLPET) to obtain in-surge compressor characteristics from post-stall transient data is presented. The

procedure is documented herein, from data acquisition and reduction through incorporation of the estimated characteristics into a compressor model.

The specialized instrumentation required to obtain the necessary transient data is described in Section 3. This instrumentation consists of airflow rakes containing high-response pressure transducers and thermocouples. The calibration of these airflow rakes is described in Section 4, along with a brief explanation of the data digitization procedure and unit conversion methods.

The airflow rake pressures and temperatures are used to calculate airflow at the compressor inlet and exit during post-stall surge transients. The airflow calculation procedure is presented in Section 5, along with results of a high-speed surge transient. In addition, Section 5 contains a description of the filtering techniques used on some of the data.

In Section 6, the basic idea of MLPET is introduced. An estimation model structure is proposed, and the results of estimating the in-surge characteristics are then presented for two cases, 90 and 98.5 percent corrected speed.

Section 7 contains a brief description of a computer model which has been configured to represent the E<sup>3</sup>-10C compressor test rig system. Low-speed in-stall characteristics obtained from steady-state test data and high-speed in-stall characteristics estimated from the surge transient data are incorporated into the model. Steady-state and transient output from the model is then compared to actual test data.

### 3.0 TEST INSTRUMENTATION

In order to obtain data useful in quantifying surge cycle behavior, specialized instrumentation was developed. This instrumentation was designed to detect high frequency pressure and temperature variations, as well as rapid airflow fluctuations in both the forward and reverse directions.

The instrumentation was also designed to minimize sensor error due to drift or temperature variations and, should error occur, a system to aid in error detection and calibration was implemented.

#### 3.1 Airflow rakes

The Airflow Rakes used in this test were custom-designed for the E<sup>3</sup> compressor flowpath with the purpose of measuring rapidly changing forward or reverse flow at the compressor inlet and exit (Figures 1 and 2). Two rakes were located at plane 25 to measure the inlet flow and two rakes were located at plane 31 just aft of the diffuser to measure the exit flow (Figures 3 thru 5). At each plane, the rakes were mounted at circumferential locations labeled "S" and "Y", which were 90 degrees apart. On each rake, transducers were mounted at two immersions in order to measure both hub and tip airflow (Figure 5).

The airflow rakes contain five sensors each; four pressure transducers (two facing forward and two facing aft) and one aspirated thermocouple.

The pressure sensors are high-response differential transducers. The transducers in the plane 25 rakes were made by Endevco and have a range of  $\pm 20$  psid. The transducers in the plane 31 rakes were made by Kulite and have a range of  $\pm 60$  psid. The natural frequencies are 100 KHz for the Endevco transducers and 275 KHz for the Kulite transducers, well above the frequencies of interest in surge analysis.

The thermocouples were type E (chromel-constantan) for both plane 25 and plane 31. The thermocouple junctions were made 0.001 inches in thickness in order to give a time constant of 10 milliseconds. These thermocouples were mounted facing aft on the rakes and were normally aspirated. The temperature recovery for the probes was  $T_i/T_t = 0.994$ .

As can be seen in Figure 5, the pressure transducers are mounted in a tube inside the rake; the end of this tube projects into the gas flowpath. When the dynamics of this tube are considered, the natural frequency of the pressure measurement becomes 400 Hz. There is a leakage path around the transducer in the tube so that the tube pressure may be measured by another remotely mounted transducer. These remotely mounted transducers are used to measure the steady-state pressure in the tubes for use in calibration.

ORIGINAL PAGE IS  
OF POOR QUALITY

ORIGINAL  
OF POOR QUALITY

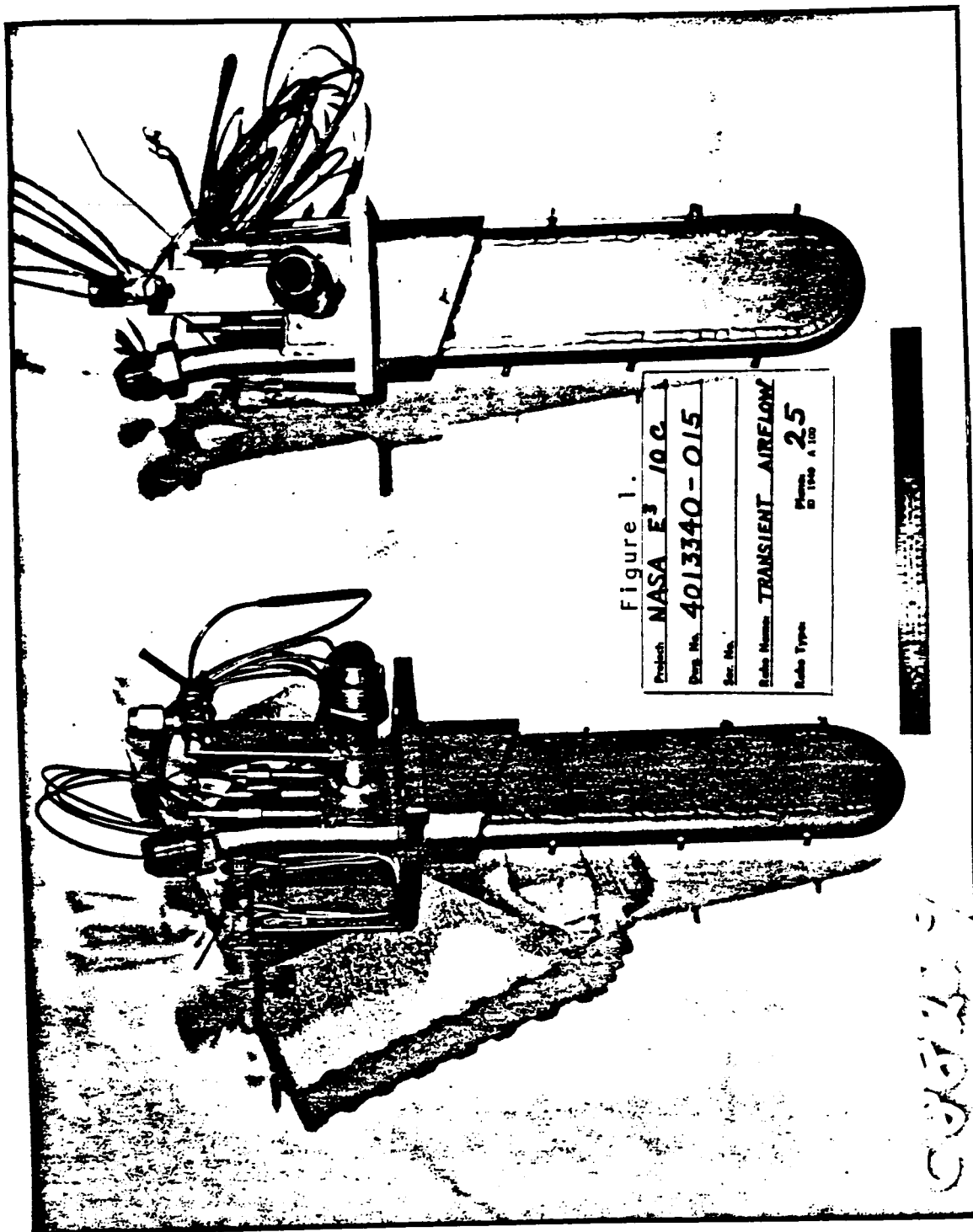
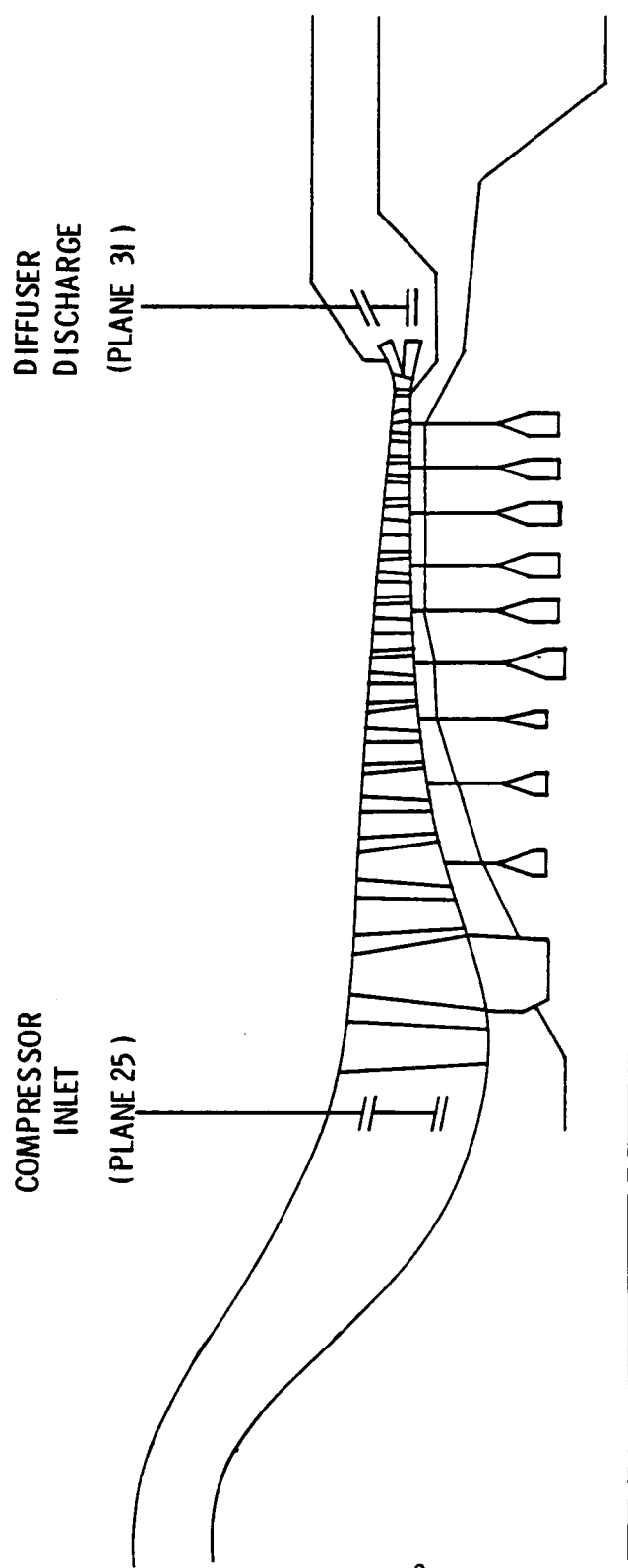


Figure 1. Plane 25 Transient Airflow Rake.

ORIGINAL PAGE IS  
OF POOR QUALITY



Figure 2. Plane 31 Transient Airflow Rake.



### 3. Dynamic Instrumentation Locations.

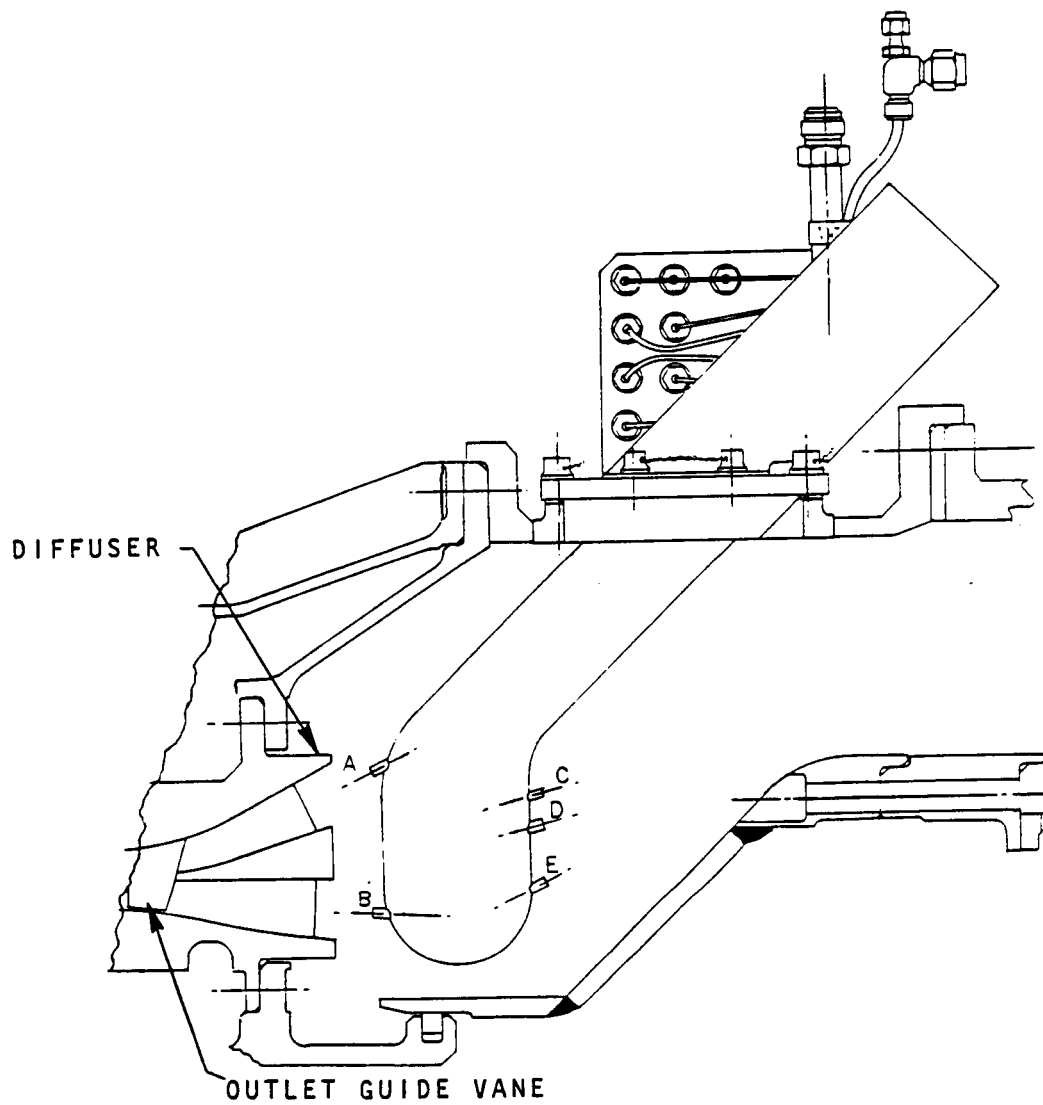


Figure 4. Plane 31 Rake Position.

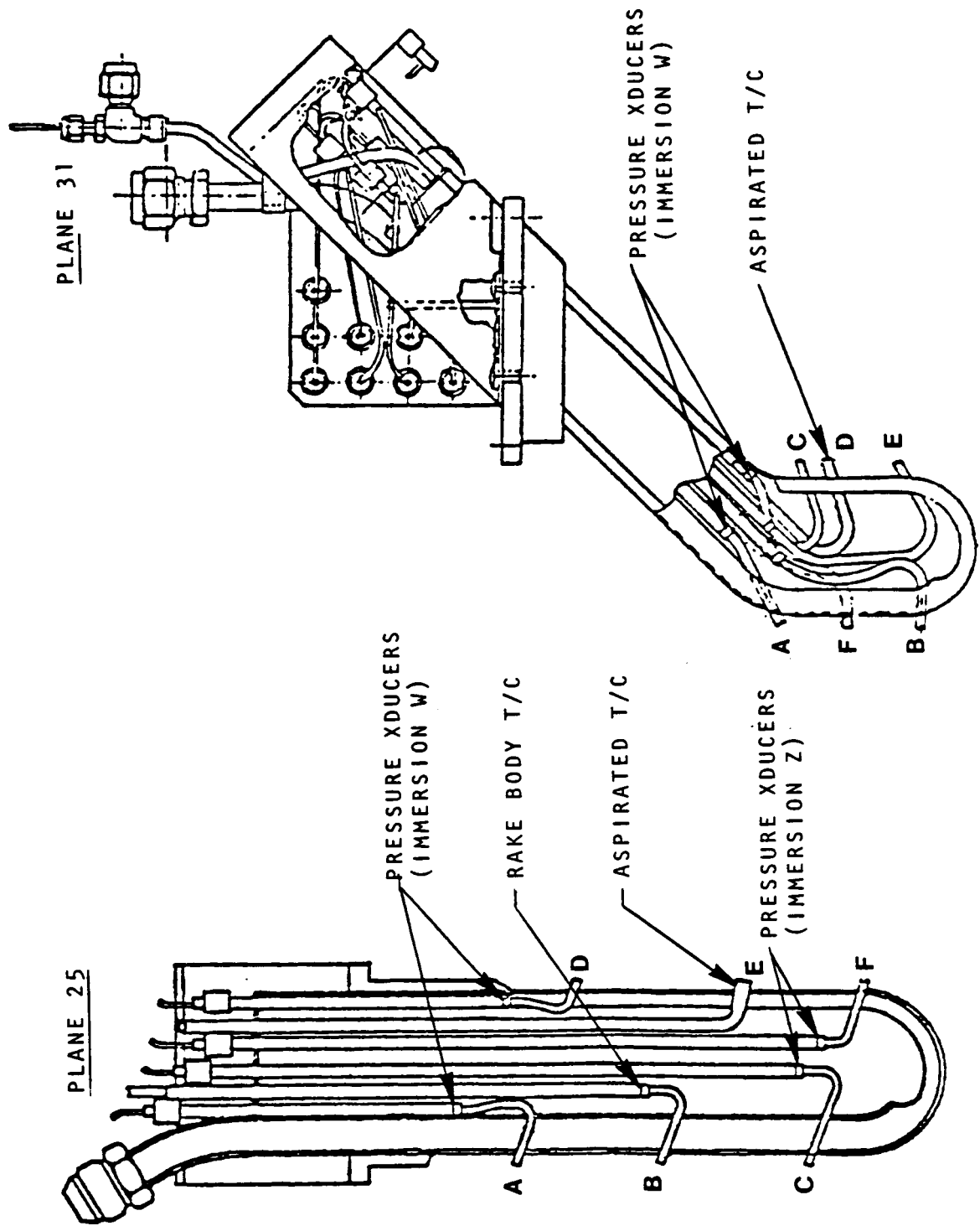


Figure 5. Airflow Rake Cross-Sections.

Since the sensitivity of the pressure transducer changes with temperature, the rakes themselves were kept at a constant temperature by means of fluid circulation. The plane 25 rakes were heated during the test by circulating sump oil at 100°F. The plane 31 rakes were water cooled to maintain a transducer temperature of less than 110°F.

### 3.2 ZOC System

To improve the accuracy of the pressure measurements, differential pressure transducers were chosen with ranges only large enough to measure expected pressure fluctuations about a reference pressure level. The ZOC (Zero, Operate, and Calibrate) system was used to introduce a constant, accurately measured pressure to the reference side of the transducers so that the range of the transducers would be extended to the magnitude of pressure to be measured.

The ZOC system has three modes of operation; the "zero", "operate", and "calibrate" modes. The operate mode is as previously described; it is the mode in which data are normally taken. The zero mode is used to pneumatically couple the sensing side of the transducers to the reference side such that the transducer output should be zero. In this mode, zero shift or electrical bias may be determined.

In the calibrate mode, a known pressure difference is applied to the reference side of the transducers. This mode is used to determine any changes in transducer sensitivity during the test due to changes in operating conditions such as temperature.

The reference pressure generated by the ZOC system was measured by high-accuracy Genesco absolute pressure transducers. The voltage output from these transducers was recorded on magnetic tape along with the voltage output of the airflow rake transducers. The ZOC pressure was also measured by the steady-state facility measurement system so that the airflow rake/ZOC system calibration procedure could be documented by steady-state readings.

#### 4.0 AIRFLOW RAKE DATA REDUCTION

Once the dynamic, in-surge data had been obtained, a few steps were necessary before the airflow calculations could be performed. First, the analog data, which was in the form of electrical signals, had to be digitized. Then, the actual pressures and temperatures had to be reconstructed from these digitized electrical signals.

##### 4.1 Digitization Hardware and Software Description

During the test, the dynamic temperatures and pressures measured by the airflow rakes were recorded on analog tape. The Lynn facility data measurement system amplified the DC voltage output of the pressure and temperature transducers. The tape recorder converted these voltages into FM signals.

During tape playback and digitization, the FM signals were reconverted to DC voltages, which in turn were amplified before being sent into the digitization system.

The digitization system consisted of an IBM PC XT configured with an A to D board and software from RC Electronics, Inc. This hardware and software, called the ISC-16 system, enables an IBM PC to operate as a digital storage oscilloscope. The system uses as input 16 channels of DC voltages in the range of  $\pm 10$  volts. This data is then digitized on a 12-bit A-D convertor at a sampling rate which was set to 1000 samples/sec. The digital data is then sorted in a buffer which can then be displayed on the CRT and stored permanently. The digitization process was triggered from a time code recorded on the analog tape during the test. The time code has a resolution of one millisecond.

The analog tape has 28 tracks, and data can be stored on six FM channels on each track. During the test, 46 of these channels were used to record dynamic pressure and temperature measurements. Out of these, 28 channels were chosen for digitization. For this reason, each surge/stall event required two digitization passes to obtain the necessary digital data. Each pass was then stored as a unique file, two of which are needed to reconstruct a particular event. With the chosen sampling rate and time code accuracy, it was possible to synchronize these two passes within one millisecond.

The calibration and airflow calculations were done on the IBM PC, with the final pressures, temperatures, and airflow then transmitted to a VAX mainframe computer for filtering and characteristic estimation. The data reduction was done in this manner to minimize data transmission from the PC to the VAX.

##### 4.2 Data Reduction and Calibration Procedure

There were two phases in the reduction and calibration procedure for the digitized signals. The first phase involved obtaining the

original voltage signal from the stored binary digital data. The second phase involved obtaining the actual temperatures and pressures represented by the voltages originally recorded on the analog tape.

#### 4.2.1 Electrical Calibration

As mentioned previously, the data were digitized by sending the voltage output from the analog system through a 12 bit binary expression with a value between 0 and 4095 directly proportional to a -10 to +10 DC voltage level. This 12 bit binary number was then stored in a 2 byte (16 bit) word. The first phase in calibration, then, was to determine gain and bias levels to reproduce from these binary numbers the voltages representing the dynamic instrumentation output.

During the test, voltage calibration signals were sent over the instrumentation channels and were recorded on tape. Prior to data digitization, these signals were played back and used to correlate the voltage levels to their corresponding binary values.

#### 4.2.2 Engineering Unit Calibration

Once these voltages had been obtained, the pressures and temperatures were recreated. In order to do this, two calibration quantities had to be known. The first quantity was the sensitivity of the particular sensor. The transducers and thermocouples used typically produced an electrical signal of a few millivolts in proportion to the pressure or temperature measured. This sensitivity was determined for each transducer and thermocouple prior to the test. The second quantity was the test facility gain used to amplify the millivolt signal up to  $\pm 2.5$  or  $\pm 1.0$  volts, depending on the sensor. This gain was also determined and recorded prior to the test.

There were three types of sensors used in conjunction with the dynamic data acquisition; high response differential transducers (Kulite and Endevco), absolute pressure transducers (Genesco), and high response E-type thermocouples. The sensitivities for the Genesco transducers and thermocouples were known prior to the test, and those values were used in the calibration. The sensitivities of the Kulite and Endevco transducers, however, were determined based on calibration measurements performed periodically during the testing.

The procedure for calibrating the airflow rake transducers involved recording two special steady-state data points; a "zero" point and a "calibrate" point. While the compressor was in a steady-state operating condition, three consecutive steady-state readings would be taken; "zero", "calibrate", and "operate" points. This calibration procedure was sufficient to determine the sensitivity and bias for each transducer. However, before each surge playback, a near-stall steady-state data point was run to determine DC bias setting so that the digital playback of the rake instrumentation matched the data

recorded during the steady-state reading using the test facility instrumentation. For example, the forward-facing pressure-probes were adjusted to read the plane average total pressures. Likewise, the individual thermocouples were adjusted to read the plane average temperature as recorded by the facility instrumentation.

## 5.0 AIRFLOW CALCULATIONS

Once the dynamic airflow rake pressure and temperature data had been obtained in digital form, the calculation of the airflows completed the data reduction procedure.

In this section, the airflow calculation procedure is explained and the digitized data from a high-speed (98.5 percent corrected speed) surge is presented and examined in some detail.

Because of inherently high noise levels resulting from the airflow calculation procedure, the data were filtered prior to use in the estimation process. The process by which the filter was designed is also included in this section.

### 5.1 Airflow-Calculation Procedure

On each airflow rake are two pairs of forward and aft-facing pressure probes. During normal operation, the pressure measured on the forward facing probe is the total pressure of the air at that point, while the aft-facing probe will measure a lower pressure (the base pressure) which is slightly above the local static pressure. Because of the close proximity of these two probes, these forward and aft pressures can be used to calculate the Mach number at a given radial and circumferential location by the use of the following formula:

$$M_{\text{CALC}} = \left[ \frac{2}{\gamma-1} \left( \frac{P_t}{P_s} \right)^{\frac{\gamma-1}{\gamma}} - 1 \right]^{0.5} \quad (1)$$

Since the aft pressure measured is a "wake" pressure and not a true static pressure, an empirical formula is used to obtain the true Mach number from the calculated Mach number. This formula was derived from rake calibration in a special wind tunnel and is given by:

$$M_{\text{TRUE}} = a M_{\text{CALC}} + b \quad (2)$$

where a and b are experimentally determined for each pair of pressure probes. The corrected flow is then calculated as follows:

$$\frac{W \sqrt{\theta}}{\delta} = \frac{A \sqrt{T_o}}{P_o} \sqrt{\frac{\gamma_g}{R}} \left( \frac{M_{\text{TRUE}}}{1 + \frac{\gamma-1}{2} M_{\text{TRUE}}^2} \right) \frac{\gamma+1}{2(\gamma-1)} \quad (3)$$

From this corrected flow, the physical flow can be calculated in the following manner:

$$W = \frac{W\sqrt{\theta}}{\delta} \frac{P}{P_o} \sqrt{\frac{T_o}{T}} \quad (4)$$

where P and T are the total pressure and total temperature at the plane of airflow measurement. During a surge, reverse flow can also be measured, the total pressure being measured on the aft-facing probe and the wake pressure being measured on the forward facing probe. The wake pressure is always lower than the total pressure, thus the direction of the local airflow can be determined by calculating the direction of pressure drop across a probe pair.

On-site airflow rake calibration was also conducted prior to each induced instability. The calibration utilized the facility airflow, pressure, and temperature measurements at the steady-state points prior to surge.

The pressure indicated by the forward facing probes was biased to match the facility instrumentation plane average. However, the bias of the aft-facing pressure probes was adjusted using the facility steady-state airflow measurements and the airflow calculation algorithm defined by Equations 1 and 2. The wake pressure was adjusted such that the airflows from the facility measurement system and the airflow rakes were the same. This calibration procedure was accomplished such that each probe pair at a measurement plane yielded the average steady-state airflow as recorded by the facility measurement system for that plane.

## 5.2 Compressor Dynamic Response

The transient airflow rake measurements for four instabilities at three different compressor speeds were digitized and reduced according to the procedure described in Subsection 5.1. Table 1 gives the conditions at which each instability event was conducted.

Table 1. Instability Events

<u>Case</u>	<u>Corrected</u>	<u>Stator</u>	<u>Duration</u>	<u>Airflow Planes</u>
	<u>Speed</u>	<u>Setting</u>		<u>Measured</u>
1	90%	Nominal	3 sec	Inlet, Exit
2	95%	Nominal	5 sec	Inlet
3	95%	Open 5°	3 sec	Inlet
4	98.5%	Nominal	5 sec	Inlet

The results of the 98.5 percent surge case are presented in this section; the results of the other three cases are presented in Appendix A. Figures 6 and 7 show the response of compressor pressure ratio and airflow in response to a surge at 98.5 percent corrected speed. Note that the pressures and airflows in these two figures represent the arithmetic average of the four probes at each of the measurement planes.

The pressure ratio and airflow response show that it took about 1.2 seconds until quasi-steady surge cycles were established. Figure 8 is a plot of compressor pressure ratio versus inlet airflow and clearly shows the initial instability transient and subsequent surge cycles. The initial transient was affected by the significant initial flow reversal through the compressor interacting with the facility inlet refrigeration system and the inlet and exit ducts, which are shown in Figure 9. A description of these effects are given in Reference 1. It should be mentioned that as a result of this flow reversal which included not only the compressor discharge plenum, but also the facility exhaust volume, and the continuous pumping airflow from the inlet refrigeration units, a significant increase in inlet pressure and temperature resulted. It is also clear from Figure 8 that the recovery segments of the surge cycles do not recover to the pressure ratio and airflow of the initial stall point. It appears that the compressor is recovering, but at a much lower pressure ratio and airflow. Figures 10 and 11 point to a probable explanation. The compressor is run at a constant physical speed, and when the compressor inlet temperature increased during the initial transient, the corrected speed was driven down to between 70 percent and 80 percent. Analysis shows that when the compressor is run at low speeds with the stators in the high-speed position, the speed line and stall point is very close to that indicated by the in-surge recovery trajectories in Figure 8.

The pressure ratio and airflow were also calculated using the tip probe pairs (Figure 12) and the hub probe pairs (Figure 13). Comparing these two figures one can see that the flow reversals during surge are not entirely axisymmetric. Rather, the flow at the tips of the blades breaks down and reverses to a much greater extent than the hub flow. This leads to a radial recirculation pattern which has been observed in other compressors, such as that of the J93 engine.

Following the initial instability, blowdown, and surge cycle development, the compressor entered a period of relatively stable surge cycles. These cycles are shown in Figure 14. The uniform character of these cycles makes them ideal for use in estimating the in-stall compressor characteristics, which will be explained in Section 6.

Figures 15, 16, 17 and 18 show the inlet corrected airflow, inlet and exit total pressure, and inlet total temperature, respectively, during these cycles as a function of time. From these plots, the characteristics of a surge cycle may be examined. A surge cycle starts at stall, at which time the exit pressure and flow rate drop

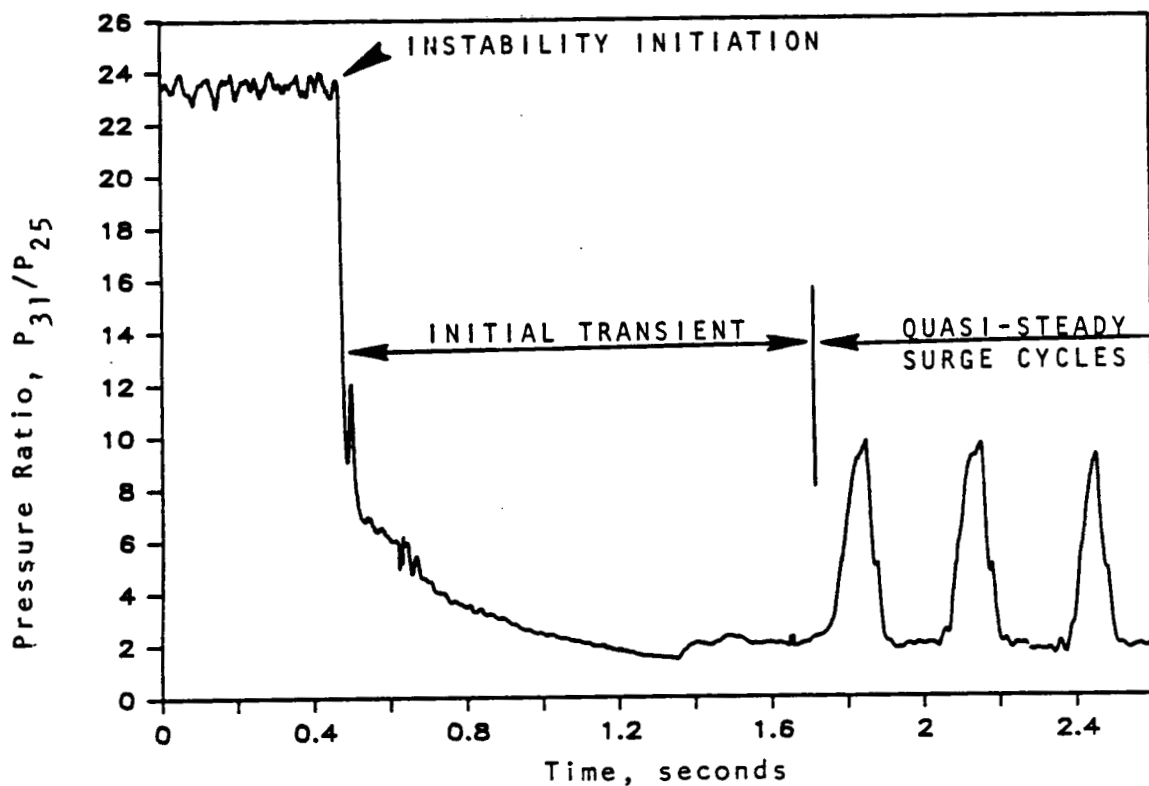


Figure 6. Face Average Pressure Ratio, 98.5%  $N_c$  Stall Inception.

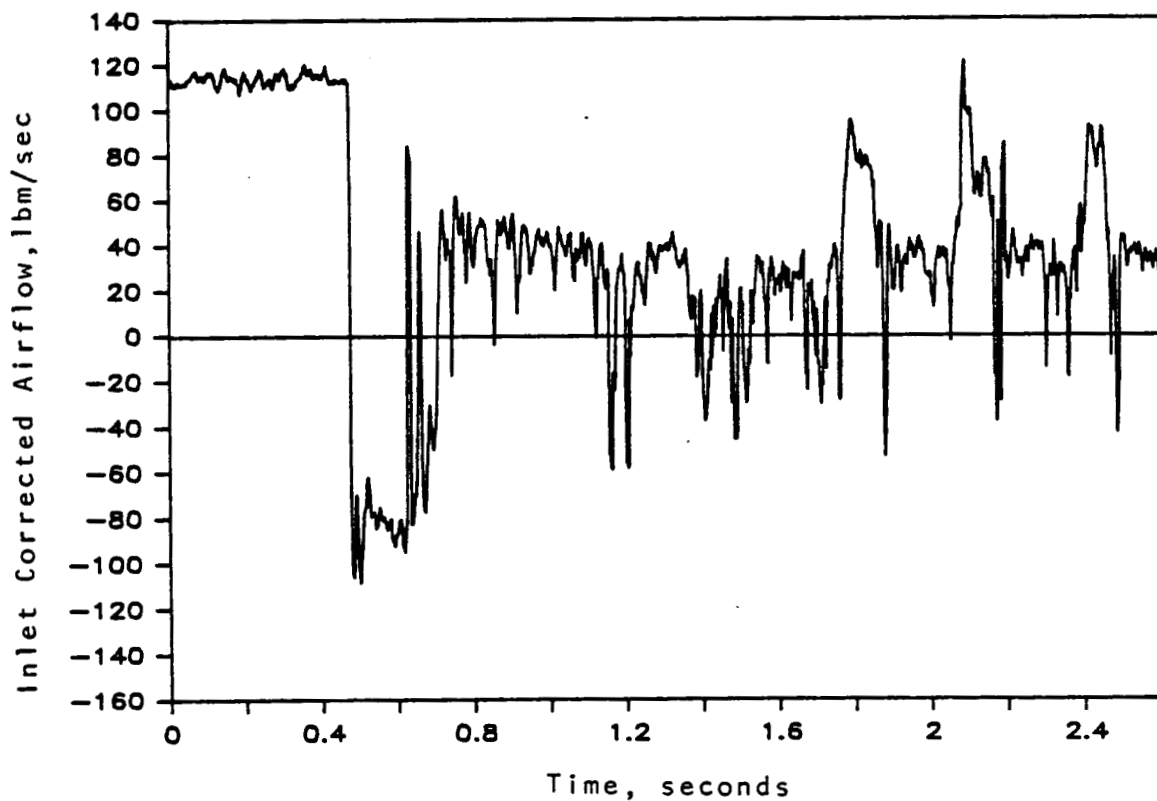


Figure 7. Face Average Inlet Corrected Airflow Rate, 98.5%  $N_c$  Stall Inception.

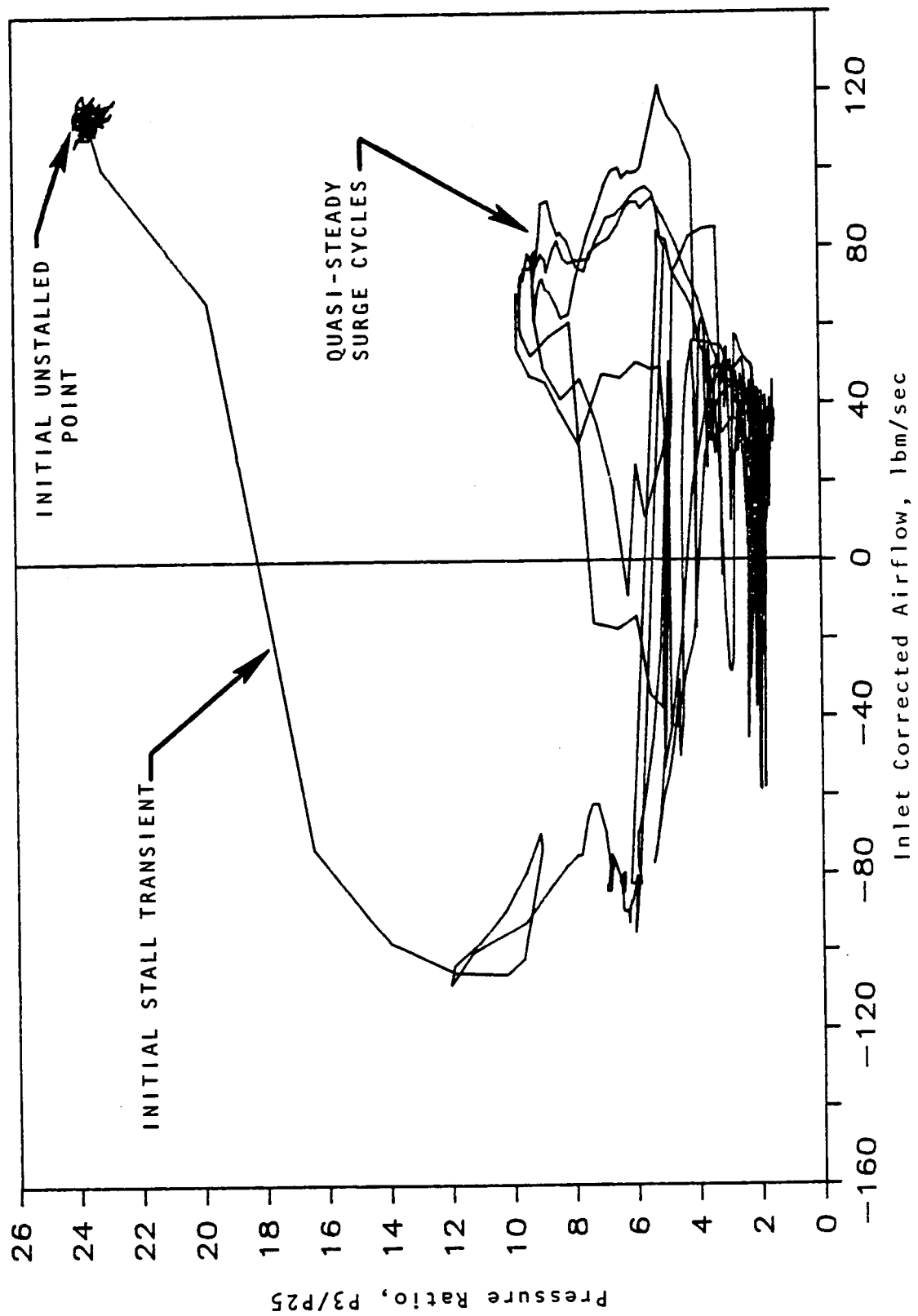
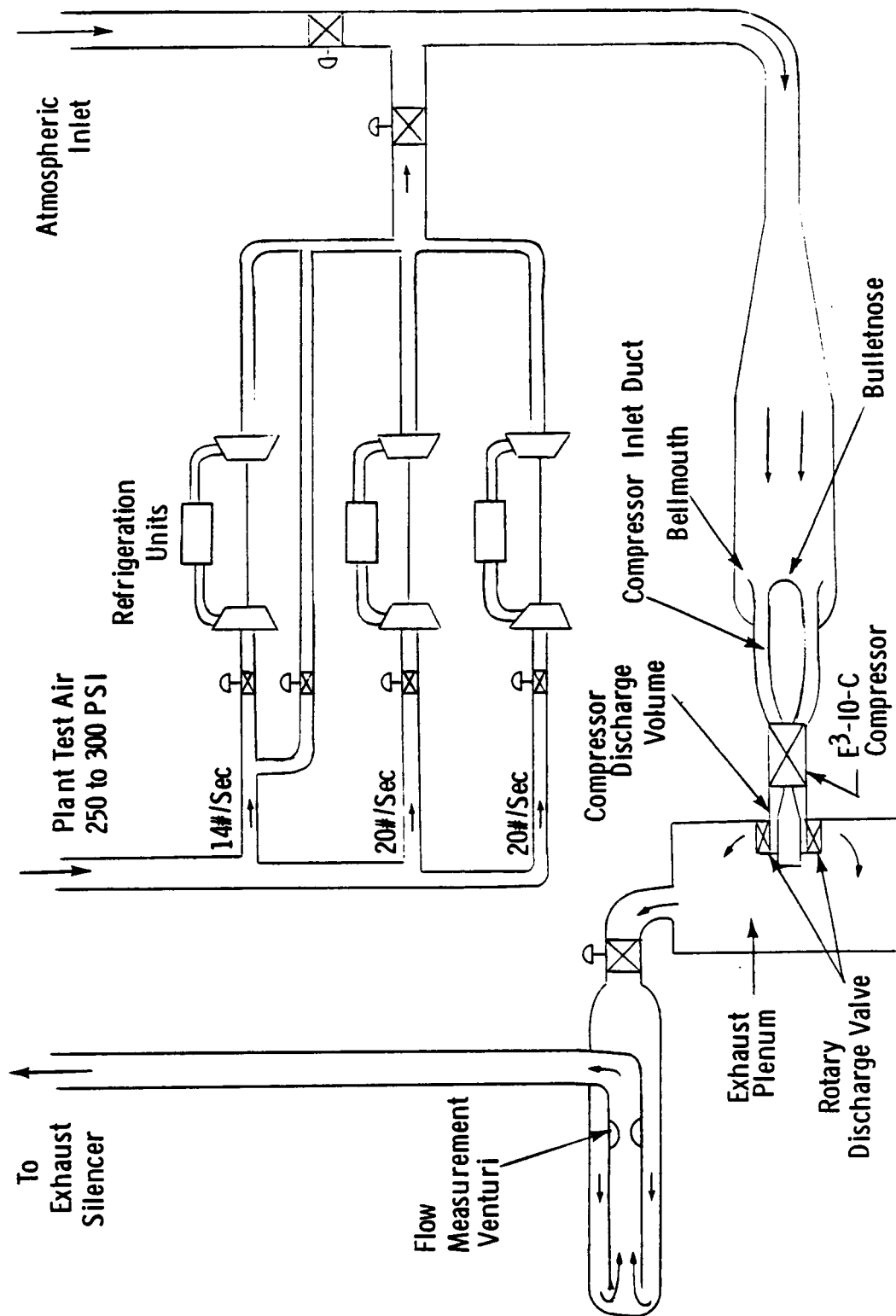


Figure 8. Operating Point Migration, 98.  $N_c$  Stall Inception.



9. Test Facility Schematic.

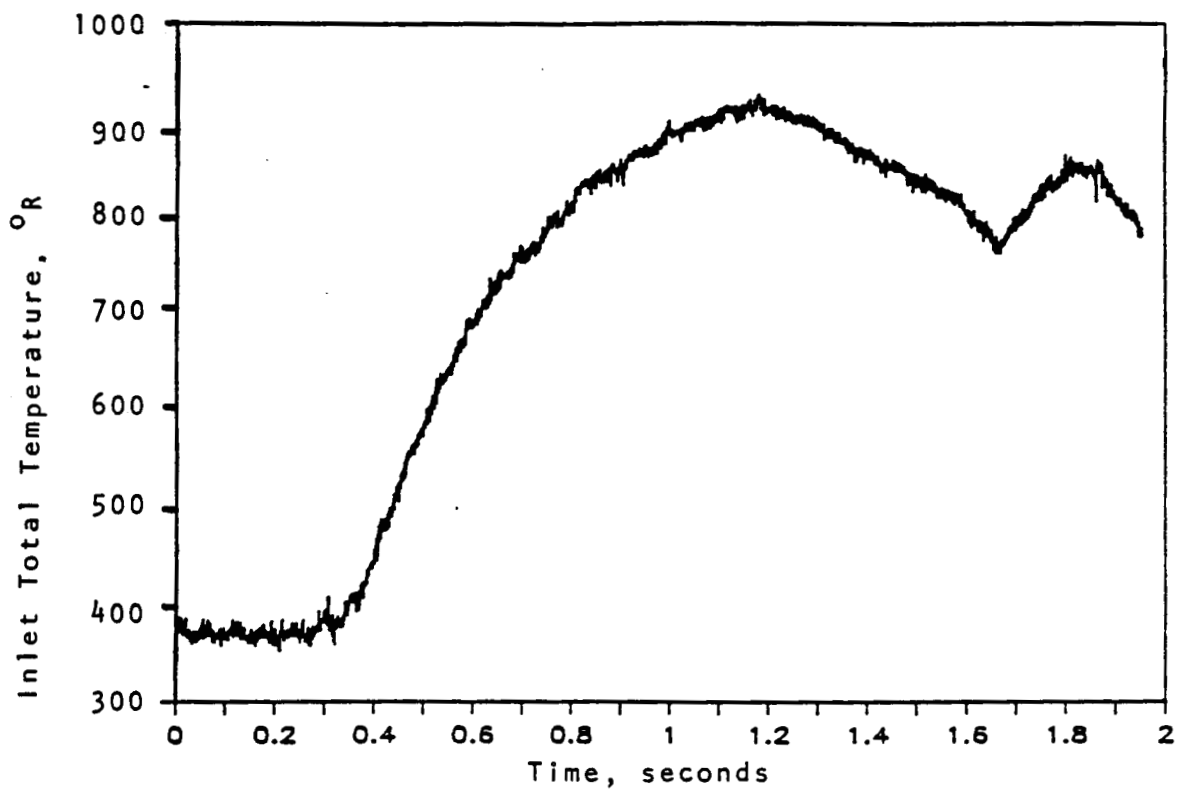


Figure 10. Compressor Inlet Total Temperature, 98.5%  $N_c$  Stall Inception.

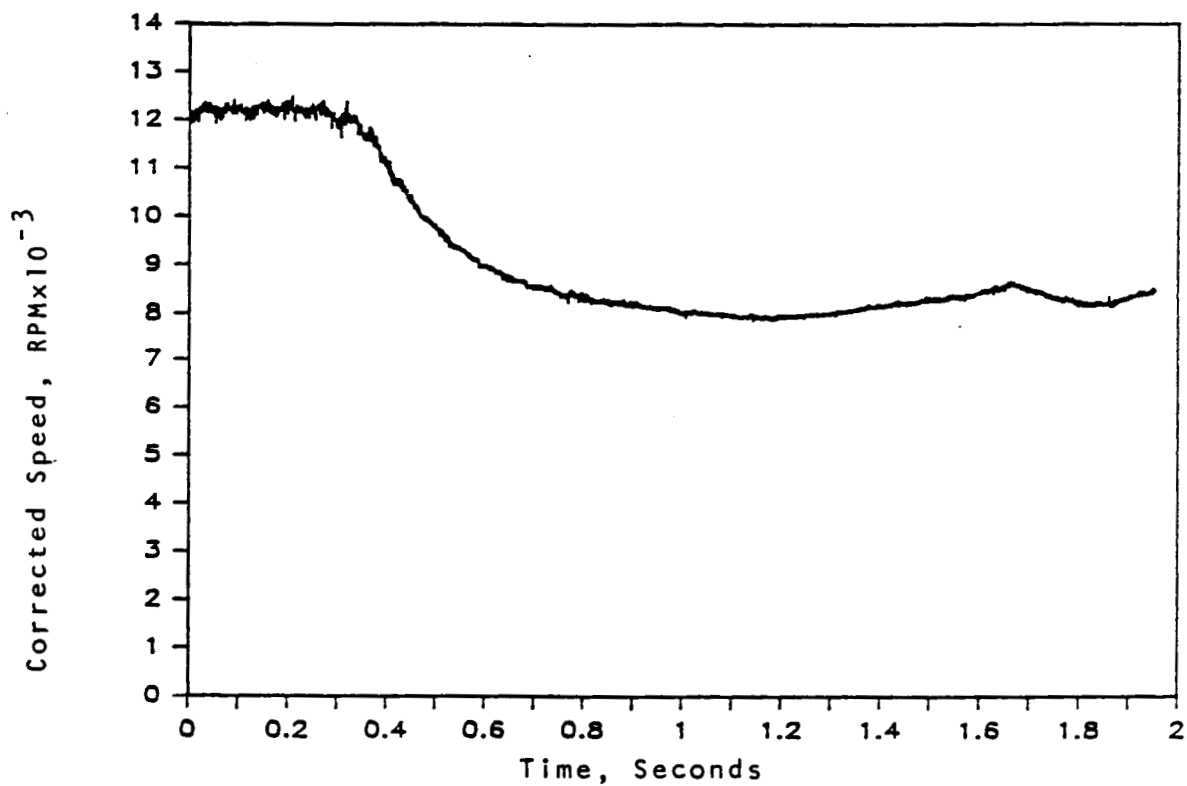


Figure 11. Compressor Corrected Speed, 98.5%  $N_c$  Stall Inception.

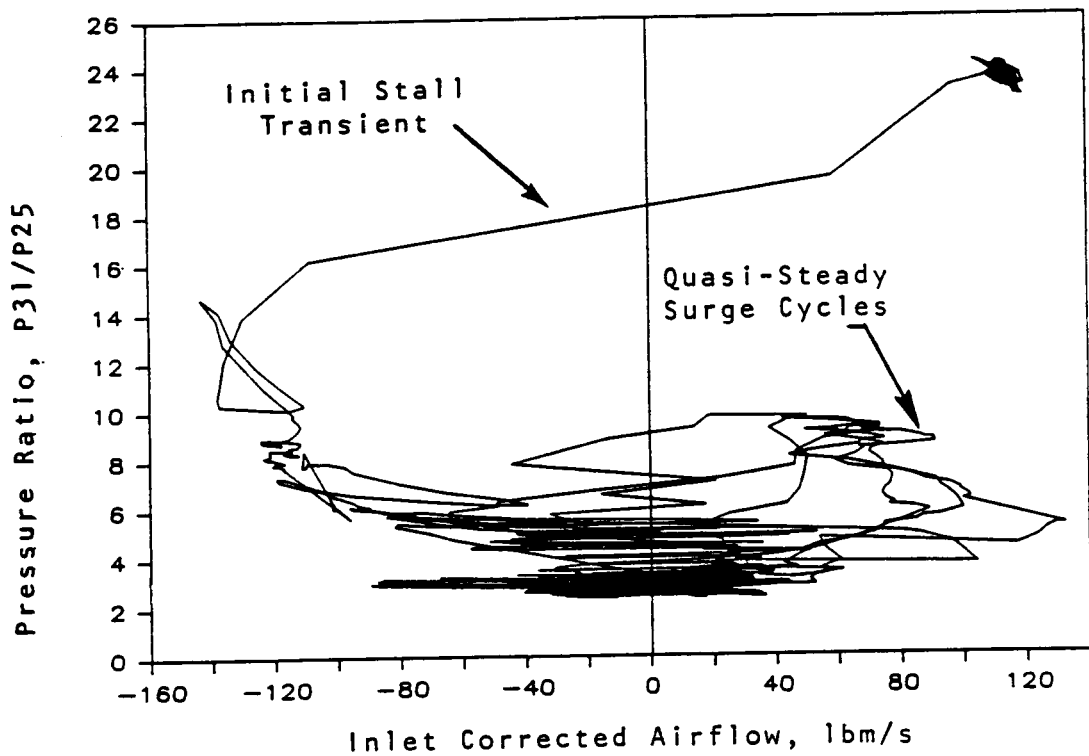


Figure 12. Tip Operating Point Migration, 98.5%  $N_c$  Stall Inception.

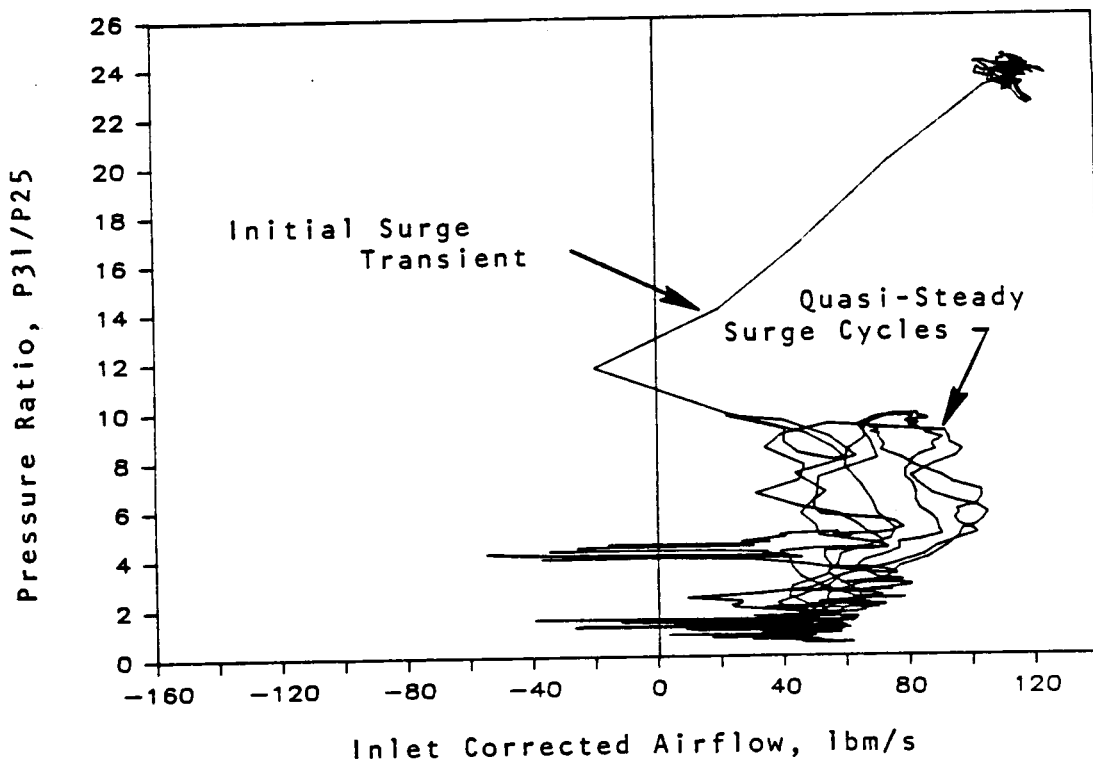


Figure 13. Hub Operating Point Migration, 98.5%  $N_c$  Stall Inception.

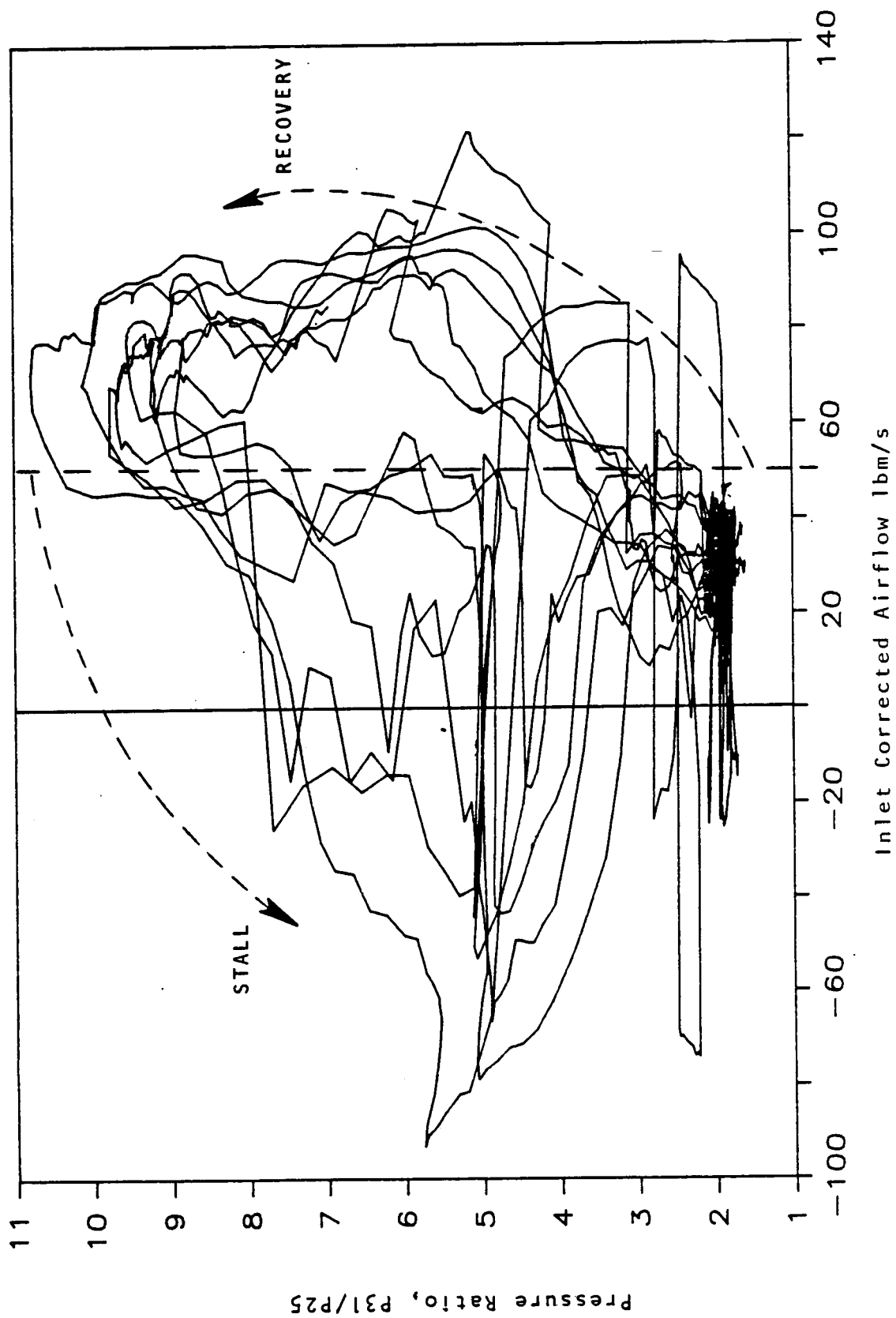


Figure 14. Operating Point Migration, 98.5%  $N_c$  Quasi-Steady Surge Cycles for  $1.8 < \text{Time} < 3.6$  Seconds.

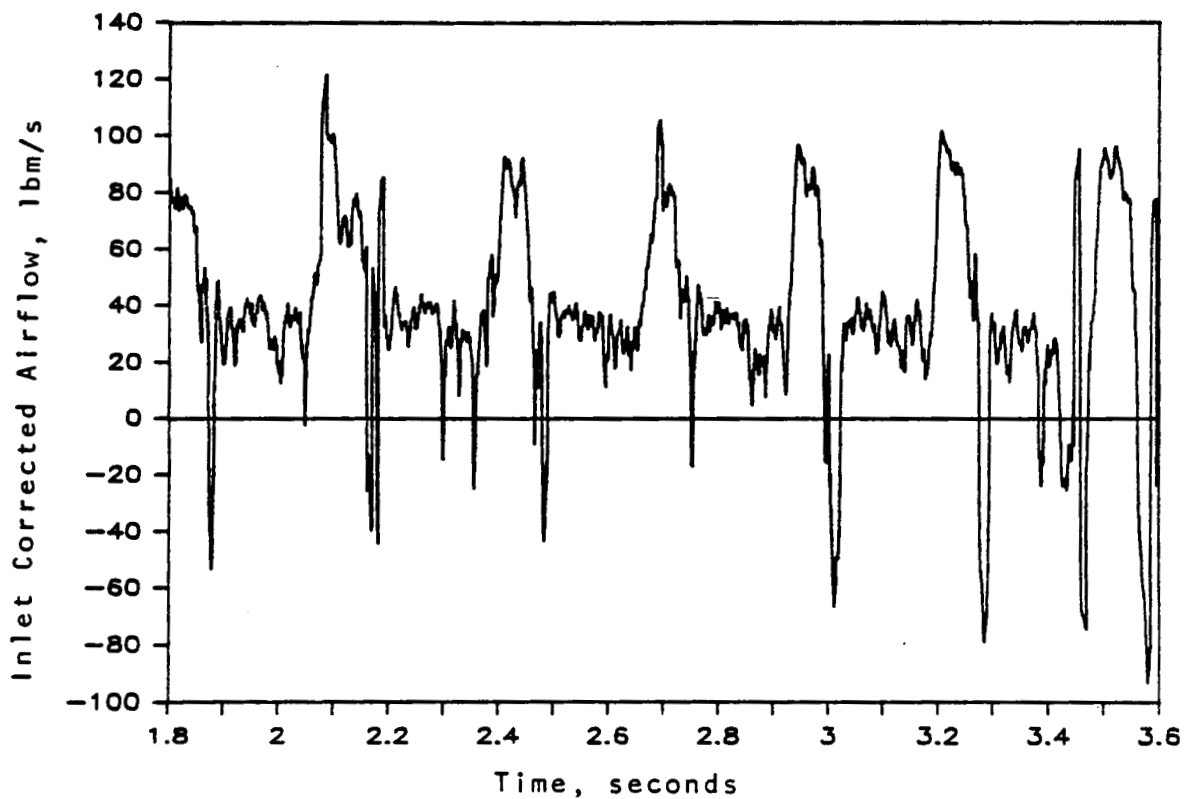


Figure 15. Inlet Corrected Airflow, 98.5%  $N_c$  Quasi-Steady Surge Cycles.

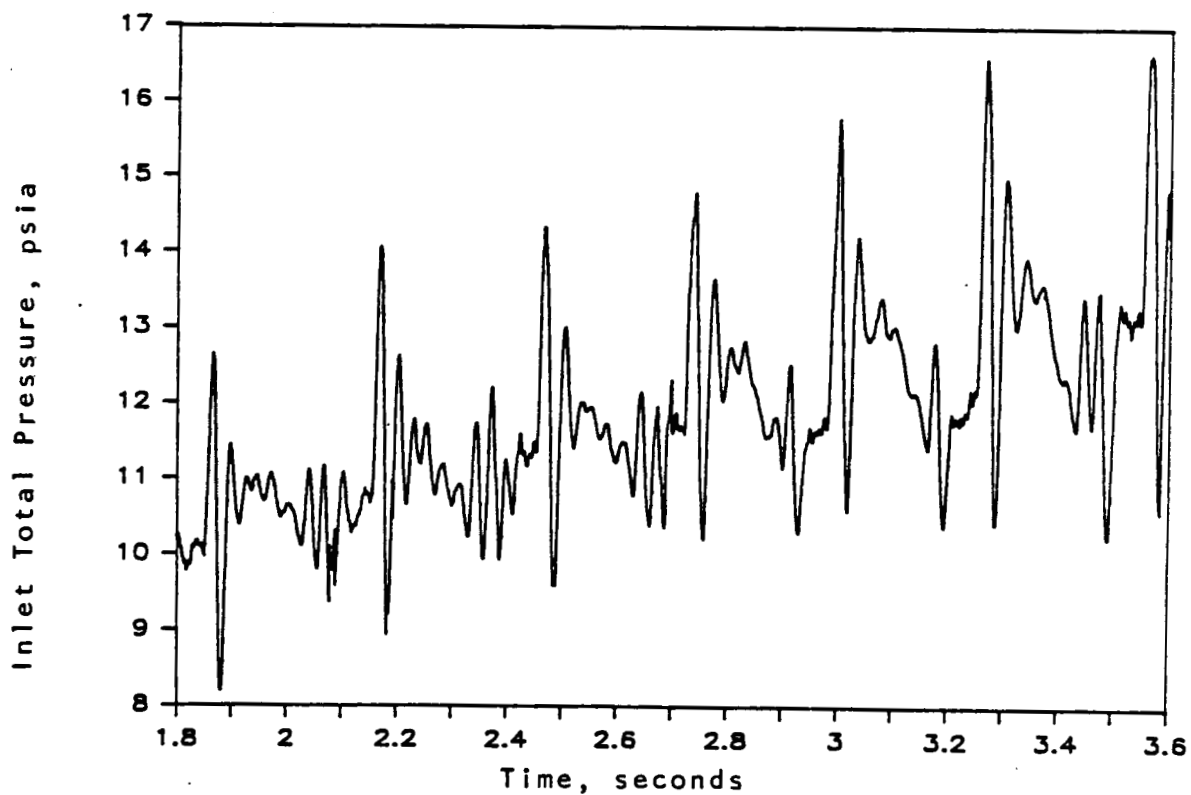


Figure 16. Inlet Total Pressure, 98.5%  $N_c$  Quasi-Steady Surge Cycles. 26

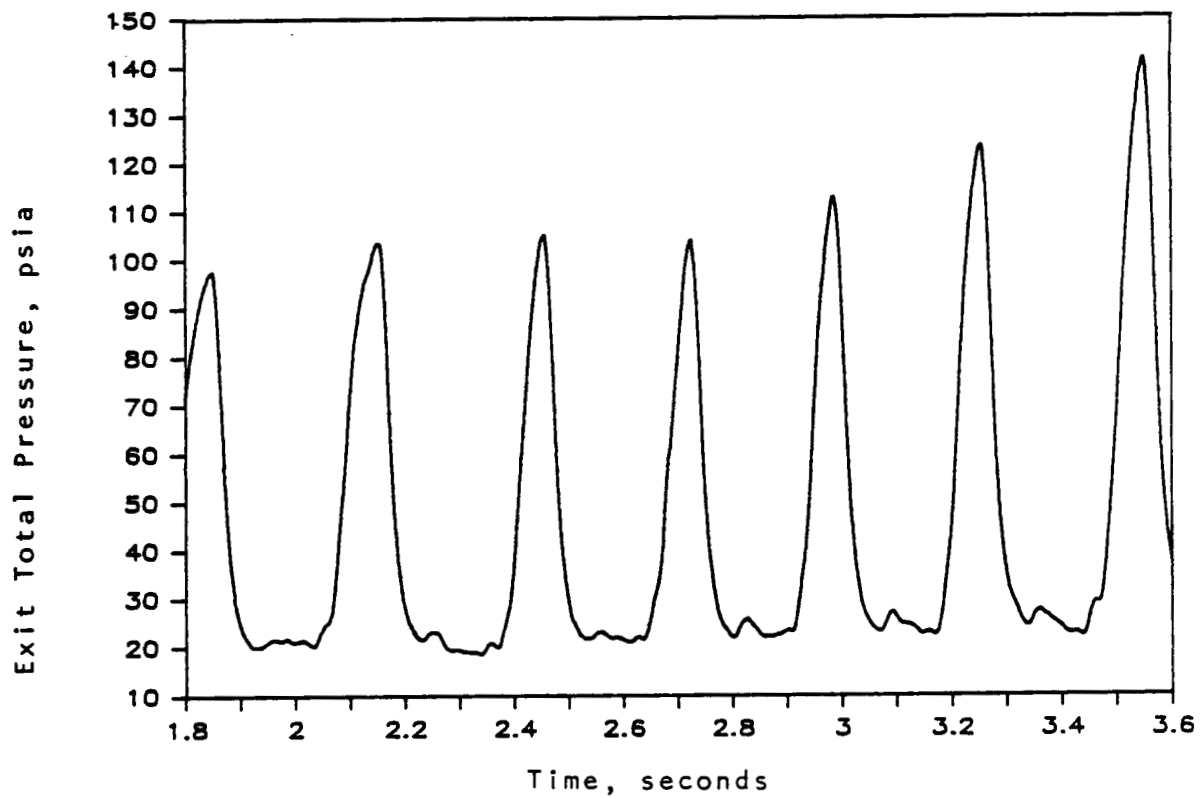


Figure 17. Exit Total Pressure 98.5%  $N_c$  Quasi-Steady Surge Cycles.

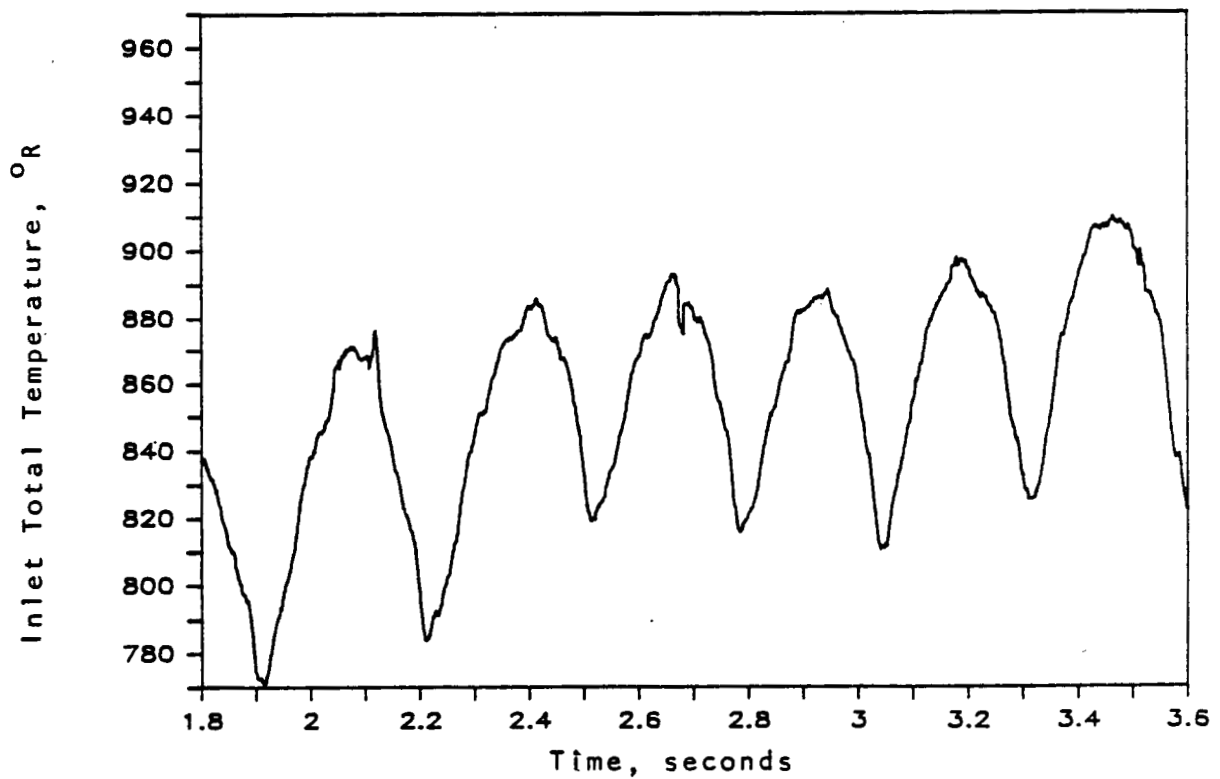


Figure 18. Inlet Total Temperature, 98.5%  $N_c$  Quasi-Steady Surge Cycles.

significantly and the airflow actually reverses. The resulting flow blockage causes an initial sudden increase in the inlet pressure, followed by an equally sharp drop-off. Once in stall, the exit pressure and airflow remain at stable, in-stall levels. Interstage static pressure measurements indicate the presence of rotating stall cells during this phase (see also Reference 1). Also to be noted is the increase in inlet temperature during this in-stall phase, indicating some kind of flow reversal, probably at the tip. As the compressor recovers, this inlet temperature drops off, while exit pressure and airflow both increase before stalling again and beginning another surge cycle.

### 5.3 Digital Filtering Techniques

The flow measurement method used to obtain the unsteady, transient airflow rate during surges is particularly sensitive to flow and pressure fluctuations which are not necessarily indicative of axisymmetric flow fluctuations. One of the major non-axisymmetric disturbances were rotating stall cells which were present in one form or another during all of the surges examined in this report.

It was decided to use the 90 percent corrected speed surge data for the filtering investigation because the sinusoidal nature of the in-stall oscillations would simplify a frequency domain analysis. The measurements plotted as a function of time are shown in Appendix A, Figures 43 through 50. The data interval for the following analysis corresponds to the segment of the instability from 2.0 to 3.5 seconds, and contains 1500 samples as shown on the following figures.

The presence of high frequency pressure fluctuations can readily be seen in Figure 19. In order to correctly analyze this signal in the frequency domain, the first order trend was removed from the signal (Figure 20). The power spectral density of this signal is shown in Figure 21. Note the dominant high frequency peak at 510 radians/sec. This corresponds to a frequency of 81.2 Hz. From interstage wall static pressure instrumentation, the rotating stall frequency was measured to be 82.5 Hz (see Reference 1). The peak just to the right of the 510 rad/sec is at approximately 1000 rad/sec which would be the first harmonic of the fundamental rotating stall frequency. The low frequency peaks occur at 44 and 100 rad/sec, which correspond to 7 Hz and 16 Hz respectively, and are more representative of the axisymmetric flow fluctuations in the compressor. In the planes of flow measurement upstream and down stream of the compressor, the flow patterns of interest are fluctuations resulting from axisymmetrical flow oscillations. The circumferential pressure disturbance caused by rotating stall cells distorts the planar flow measurements to the point of questionable physical significance, as can be seen in the large-amplitude high-frequency airflow fluctuations observed in Figure 22. This type of disturbance must be eliminated or at least attenuated in order to be consistent with the level of sophistication inherent in a one-dimensional estimation model.

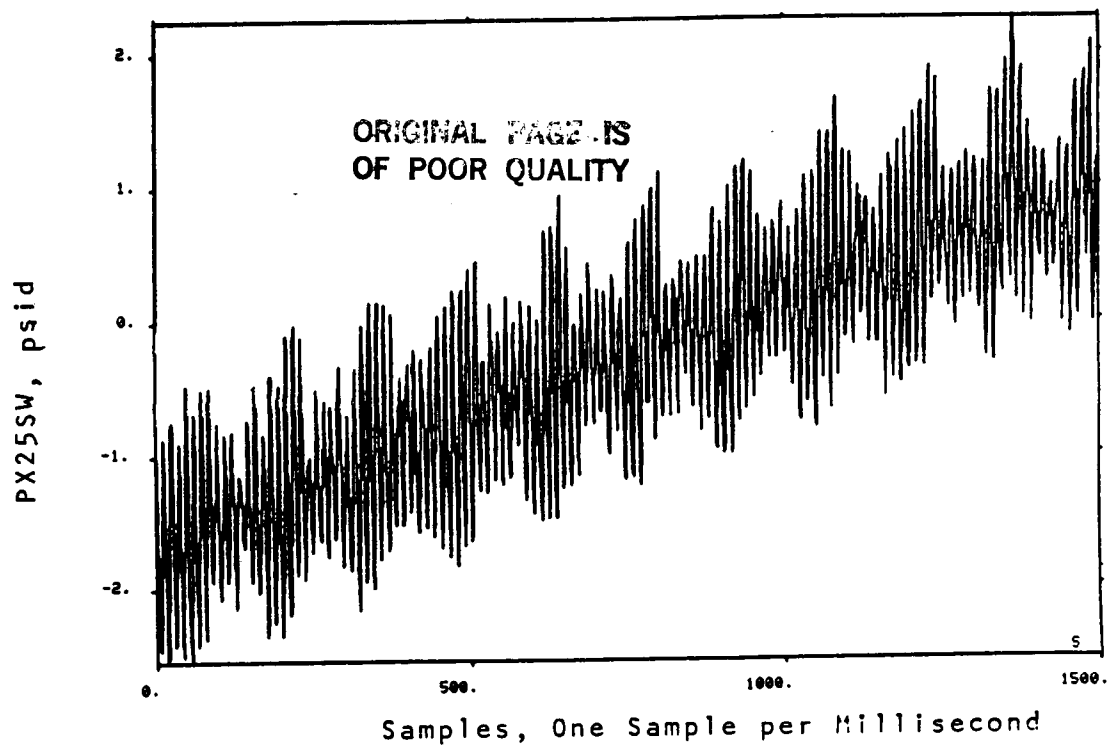


Figure 19. Unfiltered Inlet Total Pressure Kulite Signal (PX25SW), 90%  $N_c$  Instability.

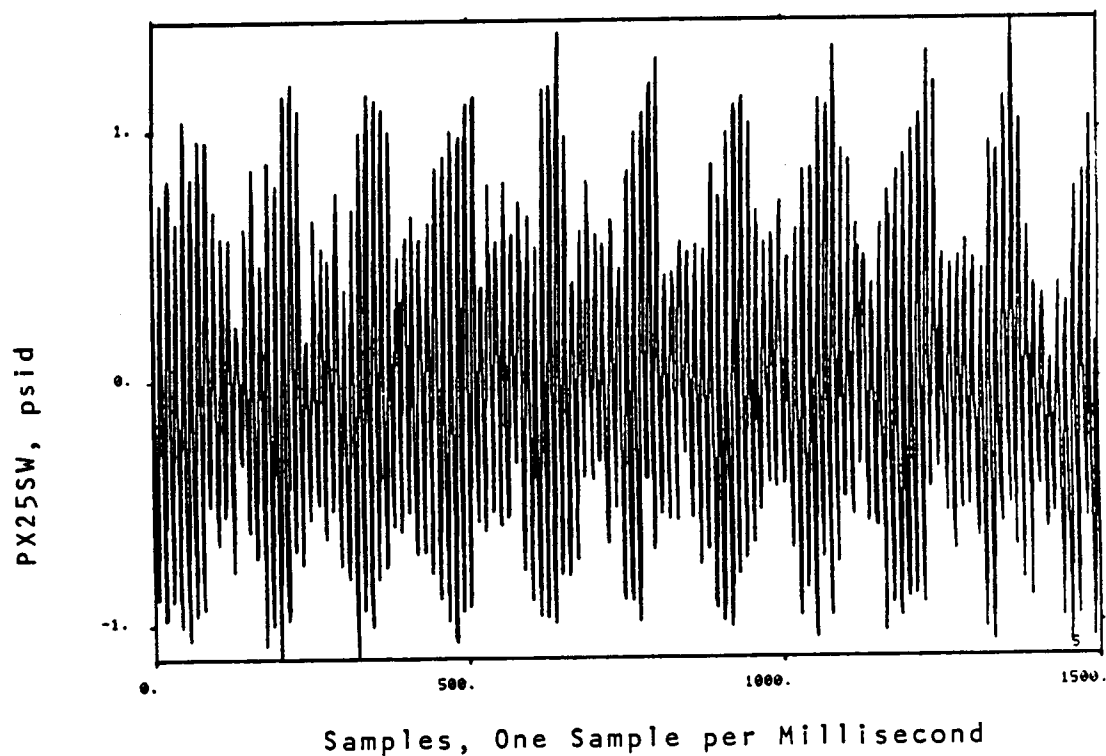


Figure 20. Unfiltered Inlet Total Pressure Kulite (PX35SW), 90%  $N_c$  Instability.

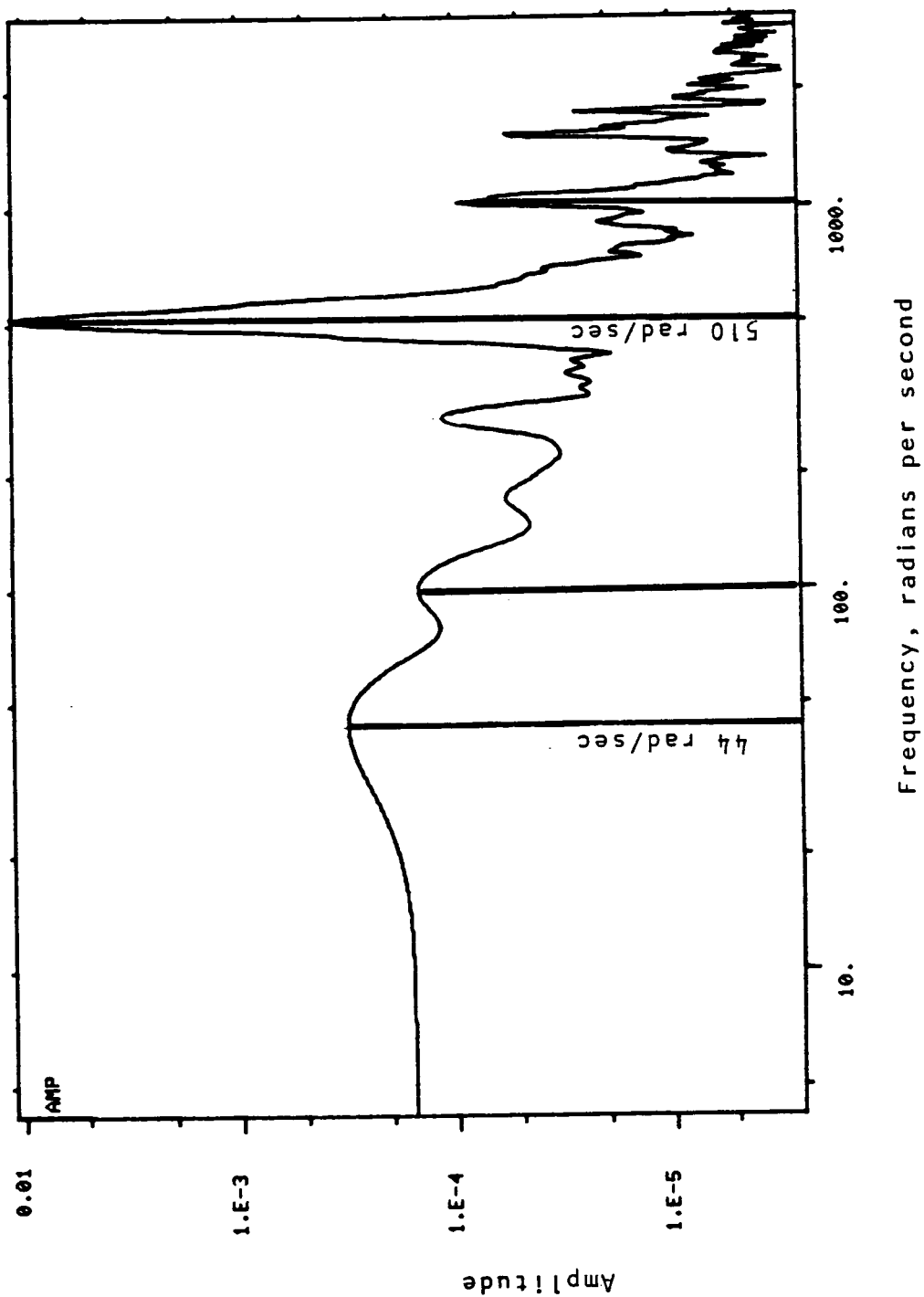
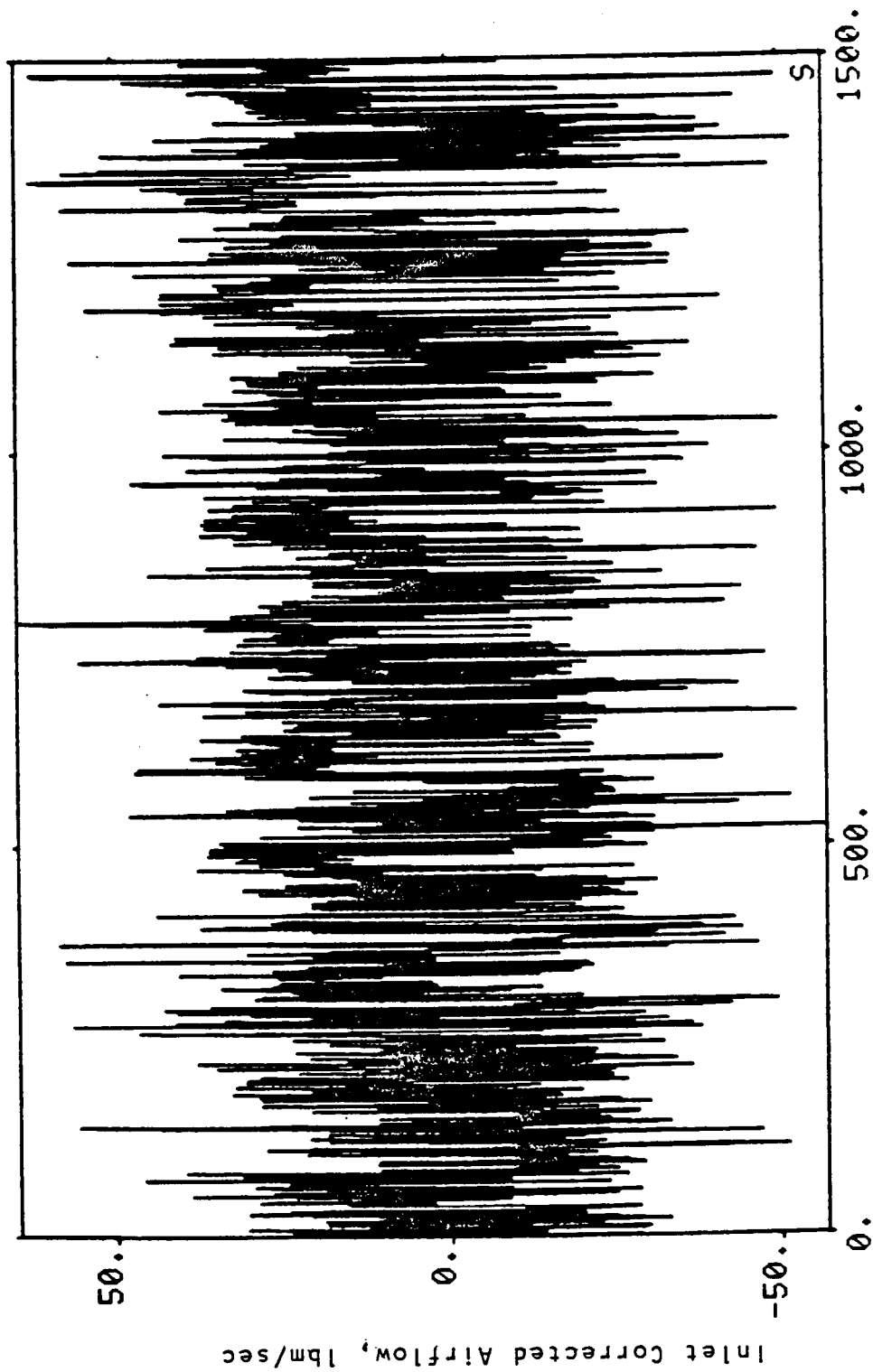


Figure 21. Power Spectrum of Unfiltered PX25SW with First Order Trend Removed, 90%  $N_c$  Instability.



Samples, one sample per millisecond

Figure 22. Inlet Corrected Airflow Calculated from Unfiltered PX25SW and PX2ASW, 90%  $N_c$  Instability.

It was therefore decided to filter the mass flow rate prior to its use in the estimation process. Two different schemes were tried. The first scheme was to filter the pressure signals from the forward and aft-facing pressure probes from which the airflow was then calculated. The second scheme was to filter the airflow itself. From the beginning it was felt that, due to the non-linearity of the mass flow rate calculation, the measured pressures should be filtered instead of the flow rate, so this scheme was used for the filter design. It was decided to use the IDPAC Butterworth filter design option because of its speed and compatibility with the parameter estimation routines. The filter cutoff frequency was chosen at 300 rad/sec (47.7 Hz), and third order and fifth order Butterworth filters were designed. Figure 23 shows the spectral densities of the pressure signals (1), filtered with a third order filter (3), and filtered with a fifth order filter (5).

These filtered pressures are then used to calculate local airflows, which are then arithmetically averaged to obtain the airflow at a given plane. Figure 24a shows a local compressor inlet airflow before and after filtering by this method, with the corresponding frequency domain plots shown in Figure 24b.

It was also verified that filtering prior to or after the airflow calculation affected the final waveform. Figures 25a compares the two schemes. Figure 25b shows the corresponding frequency domain plots. Inspection of these plots shows that some of the low frequency amplitude is lost when the second scheme (filtering the flow rate) is used; therefore, it was decided that filtering the pressure signals prior to mass flow rate calculation would yield more accurate results.

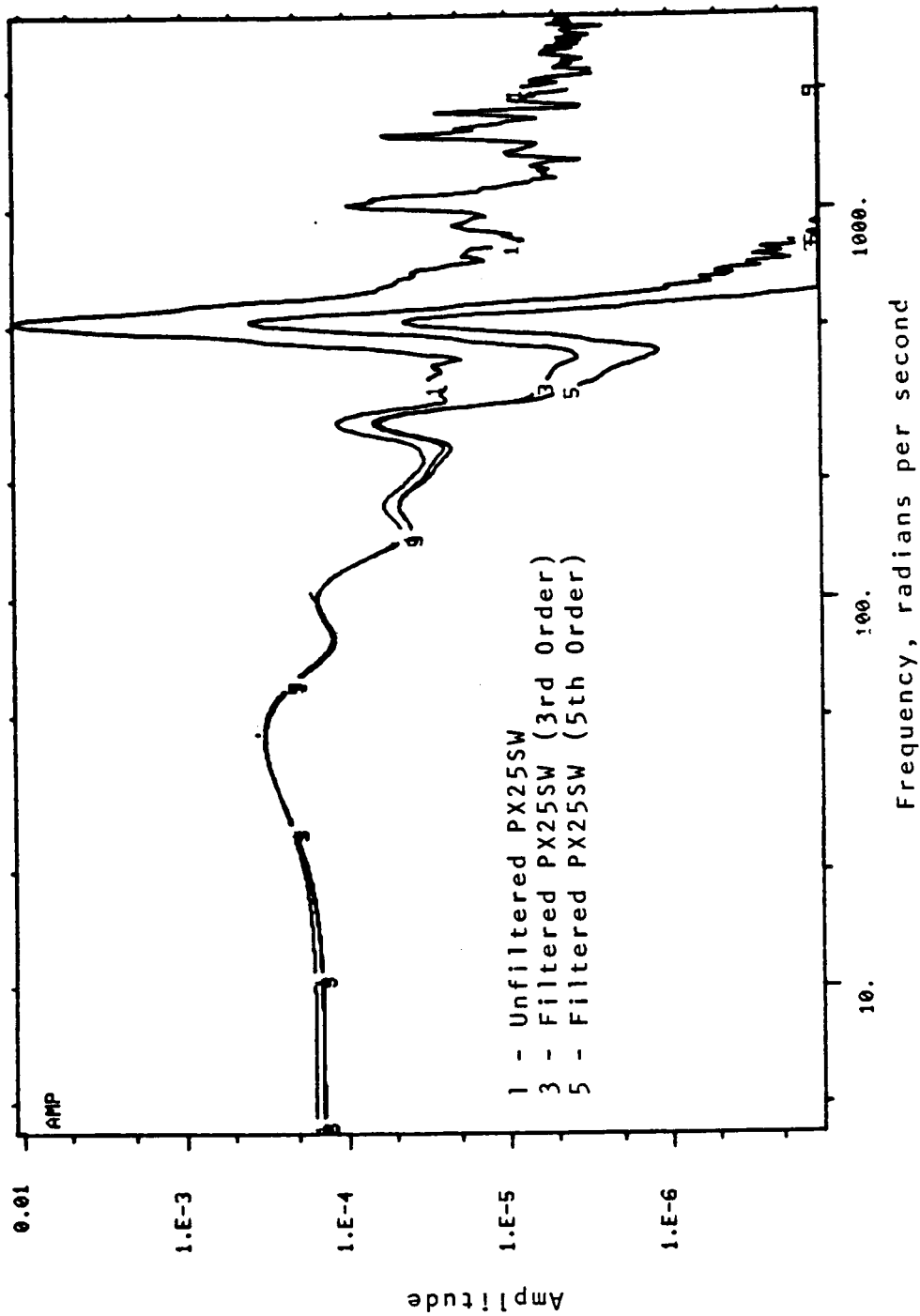


Figure 23. Power Spectra of Unfiltered and Filtered Inlet Total Pressure Kulite (PX25SW), 90%  $N_c$  Instability.

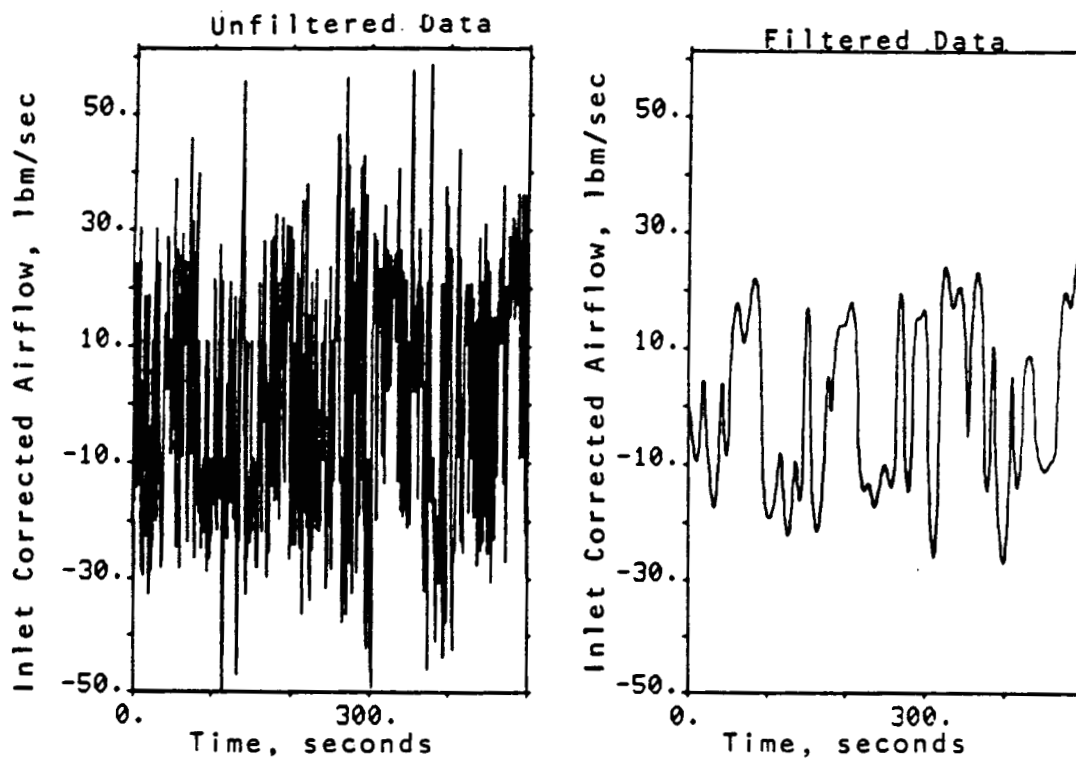


Figure 24a. A Comparison of Inlet Airflow Calculated from Unfiltered and Filtered Pressure Measurements, 90%  $N_c$  Instability.

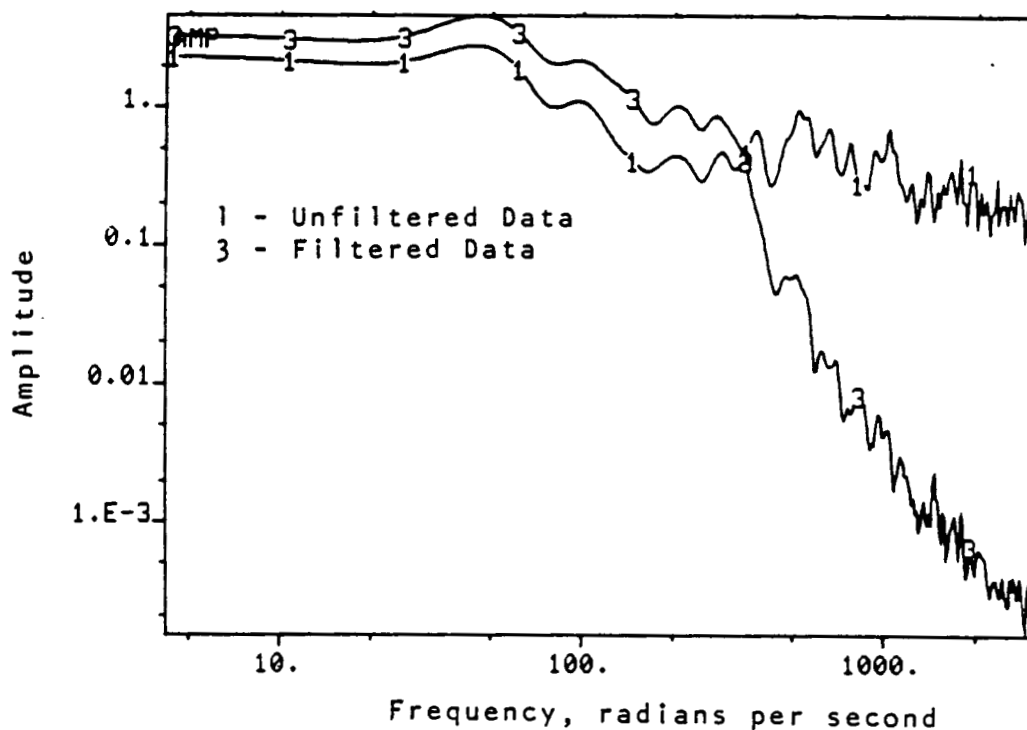


Figure 24b. Power Spectra of Inlet Airflow Calculated from Unfiltered and Filtered Pressure Measurements, 90%  $N_c$  Instability.

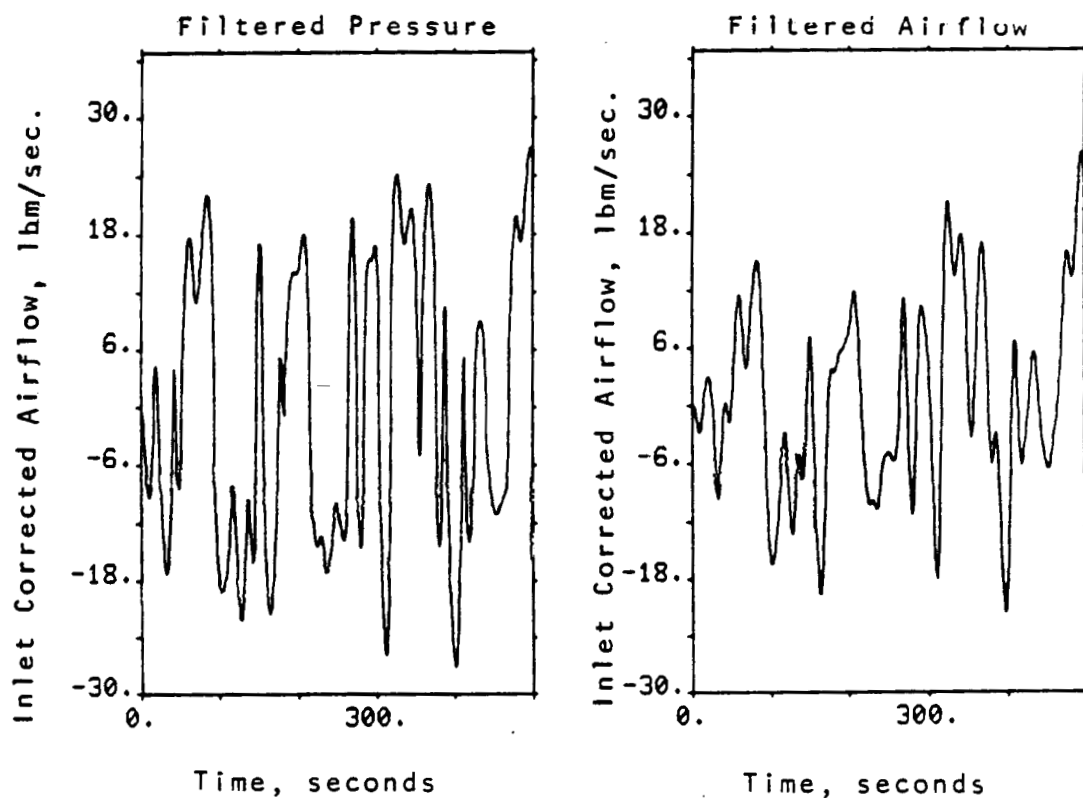


Figure 25a. A Comparison of Inlet Airflow Calculated From Filtered Pressure Measurements and Filtered Airflow, 90%  $N_c$  Instability.

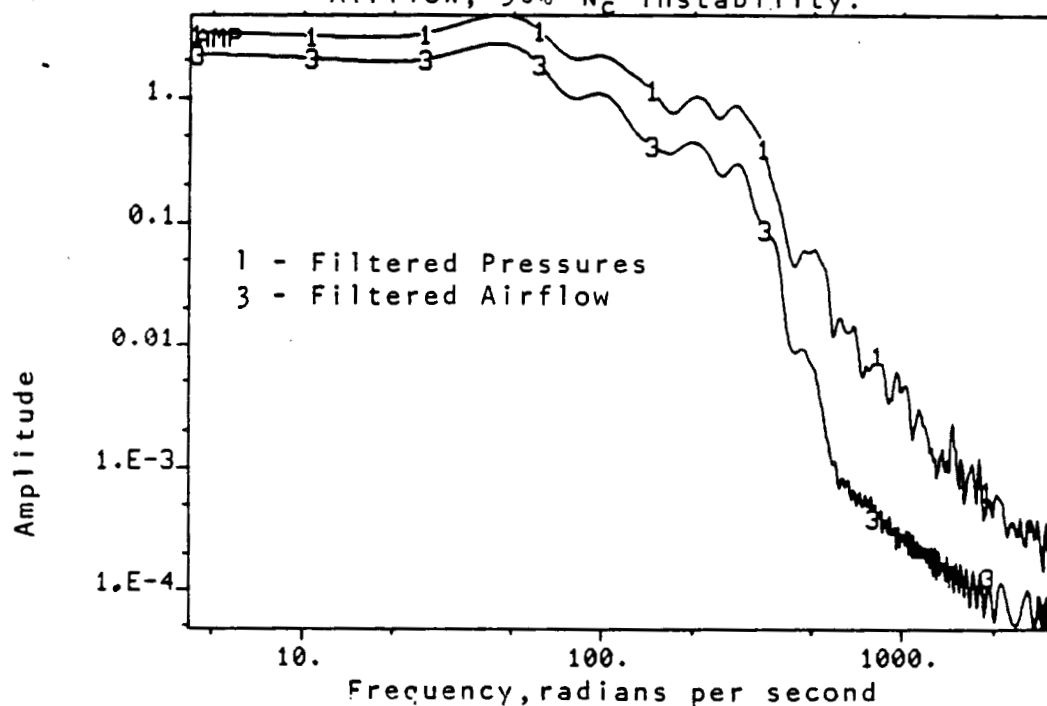


Figure 25b. Power Spectra of Inlet Airflow Calculated From Filtered Pressures and Filtered Airflow, 90%  $N_c$  Instability.

## 6.0 COMPRESSOR CHARACTERISTICS IDENTIFICATION

The oscillating, large amplitude nature of the surge cycle is based on a coupled set of highly nonlinear governing equations. Due to the complexity of the dynamics, obtaining an analytical solution to the compressor instability problem based on first principles is not feasible.

Many researchers, most notably Greitzer (Reference 2), have formulated an in-stall model which assumes that the various instability transients have as their forcing function a set of quasi-steady characteristics. The compressor can then be modelled such that the system non-linearities can be accounted for in the formulation of these quasi-steady characteristics, enabling the relationship between the quasi-steady and instantaneous characteristics to be modelled as a simple linear dynamic system.

When the compressor problem is thus decoupled into a quasi-steady non-linear part and a linear dynamic part, powerful statistical techniques based on estimation theory may be applied to the linear dynamic model to obtain both linear model parameter estimates and "fits" to the non-linear characteristics.

For this effort, Maximum Likelihood Parameter Estimation theory (MLPET), applied in the form of the software package IDPAC, was used to obtain estimates of the high-speed in-stall quasi-steady characteristics.

### 6.1 Background

Consider a multiple input, single output linear time invariant system of the form

$$\dot{\underline{x}} = \underline{A}\underline{x} + \underline{B}\underline{u} + \underline{w} \quad (5)$$

where  $\underline{x}$  is defined as the state vector of the system,  $\underline{u}$  is the input vector, and  $\underline{w}$  represents modelling errors and stochastic disturbances. The output  $y$  of this system is described by the following equation

$$y = \underline{C}\underline{x} + \underline{D}\underline{u} + v \quad (6)$$

where  $v$  represents measurement noise. The elements of  $\underline{w}$  and  $v$  are assumed to be Gaussian white noise processes.

The idea of MLPET is to obtain a reconstruction of the output  $y$ , designated  $\hat{y}$ , based on an estimated model, so that the difference between the output and its reconstructed value is minimized.

This is done by defining a loss function

$$V(\underline{\theta}) = \frac{1}{2} \sum_{i=1}^N \epsilon_i^2 \quad (7)$$

where  $\underline{\theta}$  is a vector of parameters to be estimated and

$$\epsilon_i = y_i - \hat{y}_i \quad (8)$$

Minimizing this loss function with respect to  $\underline{\theta}$  will yield the maximum agreement between a parameter and its estimate. This subject is presented in more detail in Reference 3.

For this particular effort, an interactive identification package named IDPAC was used. IDPAC was developed at Lund University in Sweden and has many useful capabilities, including maximum likelihood estimation and dynamic system modelling, as well as the frequency domain analysis and filter design techniques mentioned in Subsection 5.3. The capabilities and use of IDPAC are explained in Reference 4.

Equations 5 and 6 are continuous-time system equations which can be written in a discrete-time input-output canonical form defined by the following equation:

$$A(q^{-1})y(t) = B_1 u_1(t) + \dots + B_m u_m(t) + C(q^{-1})e(t),$$

for  $t = 0, 1, 2, \dots$  (9)

where  $q^{-1}$  is a delay operator such that

$$q^{-1}u(t) = u(t-h) \quad (10)$$

and where  $h$  is the delay time,  $y(t)$  is a single output,  $u(t)$  is a vector comprised of  $m$  inputs, and  $e(t)$  is the measurement error.

The functions  $A$ ,  $B$ , and  $C$  are polynomials of  $q^{-1}$  as follows:

$$\begin{aligned} A(q^{-1}) &= 1 + a_1 q^{-1} + a_2 q^{-2} + \dots + a_n q^{-n} \\ B(q^{-1}) &= b_0 + b_1 q^{-1} + \dots + b_n q^{-n} \\ C(q^{-1}) &= 1 + c_1 q^{-1} + \dots + c_n q^{-n} \end{aligned} \quad (11)$$

The parameters to be estimated are the coefficients of these polynomials. The best estimate of these parameters is obtained by minimizing the loss function described by Equation 7. A measure of the random error input to the system is then defined by

$$\lambda = \frac{2}{N} \min_{\theta} [v(\theta)] \quad (12)$$

where N is the number of input-output samples used in the estimation.

The accuracy of the estimate of a given parameter  $\theta_i$  is found by calculating the uncertainty,  $\sigma$ , of that parameter, which is defined by

$$\sigma_{\theta_i}^2 = \lambda^2 [v_{\theta\theta}(\theta)]_{ii}^{-1} \quad (13)$$

where  $v_{\theta\theta}(\theta)$  is the second partial derivative of the minimized loss function (equation 7).

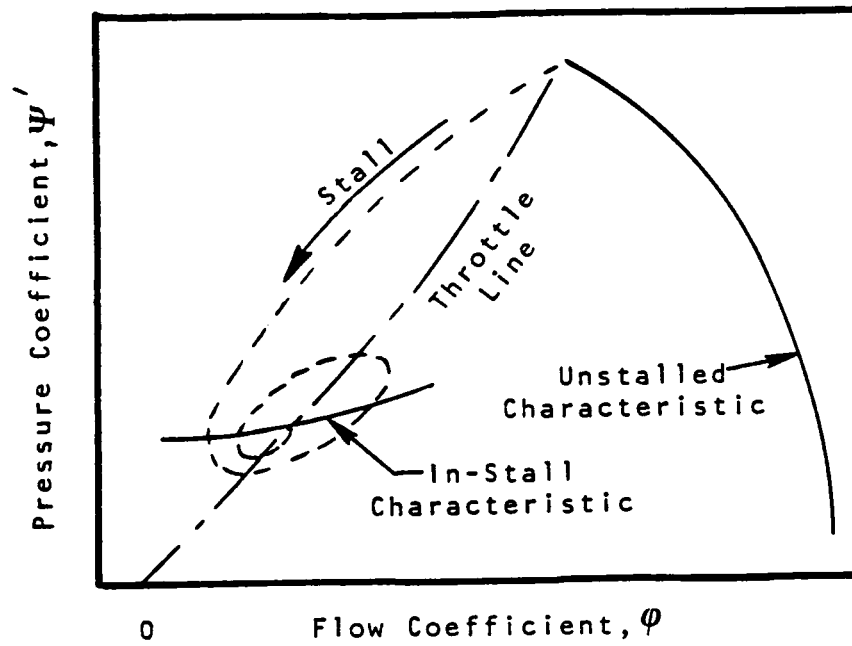
## 6.2 Estimation Model

The dynamic model assumed for the compressor has as its foundation quasi-steady characteristics to which the compressor has two fundamental modes of response. This model is illustrated in Figure 26. One response is associated with low-speed behavior and involves at the point of stall the transition from an unstalled steady-state point to a rotating stall quasi-steady operating point along a trajectory assumed to be a first order decay.

The high-speed post-stall transient is also assumed to be a first order response, but in this case the operating point migrates with time and the resulting surge cycle is therefore based at times on the in-stall characteristic, the unstalled characteristic, and also the in-stall reverse-flow characteristic. The high-speed operating point migration shown in Figure 26 may be compared with actual test data previously shown in Figures 8 and 14.

The techniques developed for identifying the in-stall characteristics inherent to surge transient data are based on the fact that compressor flow exit properties can be related to the inlet conditions, and this relation is basically a function of the quasi-steady, in-stall characteristics and the compressor time-response constants. Evaluation of this relationship is done using only inlet and exit measurements. Thus, independent from the system where the data are to be acquired, engine or test rig system, the identification process does not have to be system dependent. This approach simplified the identification methodology and alleviates many of the difficulties that would be encountered if the component parameter identification were based on a system representation. In Reference 5, a methodology

### Low Speed Compressor Response



### High-Speed Compressor Response

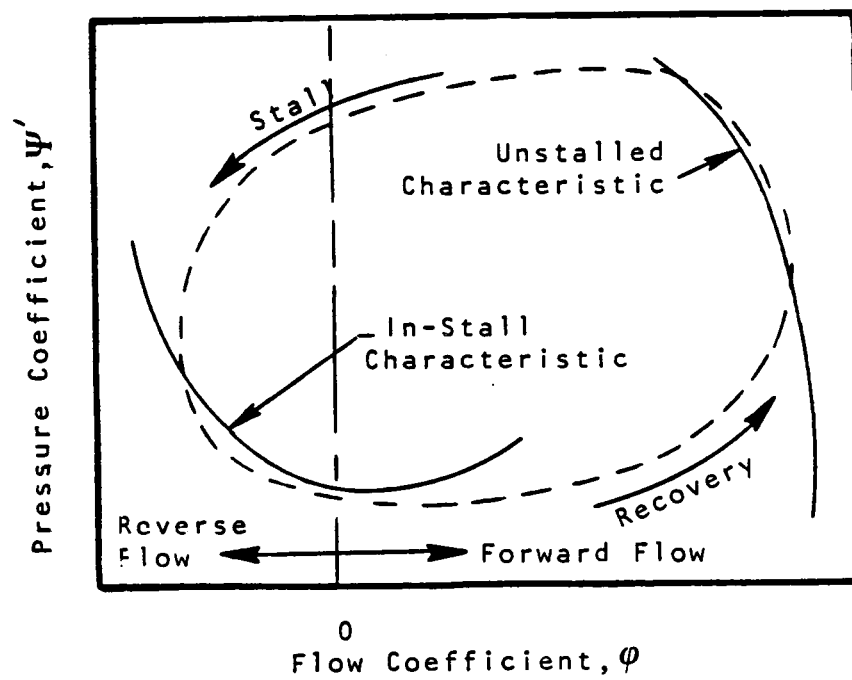


Figure 26. Compressor Estimation Model

based on a system identification model has shown that precise surge initiation synchronization between the model and the measurements was necessary for successful parameter identification. Such synchronization is expected to become more difficult when the surge is not initiated as a planar wave, as is the case with real compression systems. In addition, for a system modelling technique, the compressor parameter estimation will be biased due to any errors introduced through incorrect modelling or misrepresentation of the other system components.

In the following sections, the identification model based on these compressor inlet and exit relationships is presented.

#### 6.2.1 Pressure Coefficient Estimation Model

The pressure coefficient model structure is based on a simplified version of the momentum equation together with a first order time delay equation. A one-dimensional model was assumed, and the convective momentum terms and mass accumulation within the compressor control volume were neglected. With these assumptions, the momentum equation becomes decoupled from the mass and energy equations. Thus, the pressure coefficient can be explicitly obtained. The simplified momentum equation appears as follows:

$$\frac{L}{Ag} \frac{dW_{25}}{dt} = \left[ \Psi' \frac{U^2}{2g J C_p T_{25}} + 1 \right]^{\frac{\gamma}{\gamma-1}} P_{25} - P_{31} \quad (14)$$

The first order time delay function is

$$\tau \frac{d\Psi'}{dt} + \Psi' = \Psi'_{QS} \quad (15)$$

where  $\Psi'_{QS}$  is the quasi-steady pressure coefficient and is a function of the flow coefficient  $\phi$ , where the flow coefficient is defined by

$$\phi = \frac{M_{25}}{U} \left[ \frac{\gamma g R T_{25}}{1 + \frac{\gamma-1}{2} M_{25}^2} \right]^{0.5} \quad (16)$$

For this model, the measured parameters are compressor inlet total pressure  $P_{25}$ , exit total pressure  $P_{31}$ , inlet total temperature

$T_{25}$ , and inlet physical airflow  $W_{25}$ . The estimation involves obtaining the time constant  $\tau$  and the functional relationship between  $\Psi_{QS}$  and  $\phi$  :

$$\Psi'_{QS}(\phi) = \sum_{i=1}^m \beta_i s_i(\phi) \quad (17)$$

where  $s_i$  are known input functions of  $\phi$  and  $\beta_i$  are the unknown parameters to be estimated. The relation described by Equation 17 is constrained to be a linear function of the input signals  $s_i$ . The assumed functional form of  $\Psi'$  (a polynomial in  $\phi$ ) dictates the set of signals  $s_i$  to be used.  $QS$

The model given by Equations 14 and 15 must be put into a discrete multi-input single-output (MISO) form for IDPAC to use:

$$\Psi'_{k+1} - a \Psi'_k = \sum_{i=1}^m b_i s_{i,k} \quad (18)$$

The coefficients for this model are

$$a = e^{-h/\tau} \quad (19)$$

and

$$b_i = (1-a) \beta_i \quad (20)$$

where  $h$  is the digital sample period. With the system in this form, the parameters to be estimated are  $a$  and  $b_i$ .

From previous estimation work on model data and low-speed in-stall test data, the in-stall pressure coefficient is assumed to be in the form of a parabola. Thus Equation 16 becomes

$$\Psi'_{QS} = b_1 s_1 + b_2 s_2 + b_3 s_3 \quad (21)$$

where

$$s_1 = 1.0, \quad s_2 = \phi, \quad \text{and} \quad s_3 = \phi^2.$$

#### 6.2.2. Work Coefficient Estimation Model

The work coefficient model structure is based on the compressor control volume energy equation together with a first order time delay

equation. The energy equation is expressed in terms of entropy and is given by:

$$\frac{d}{dt} (\rho_{25} s_{31}) = s_{25} w_{25} - s_{31} w_{31} + s_F \quad (22)$$

$$s_F = w_{25} \frac{R}{J} \ln \left[ \left( \psi \frac{u^2}{2gJC_p T_{25}} + 1 \right)^{\frac{\gamma}{\gamma-1}} \left( \psi' \frac{u^2}{2gJC_p T_{25}} + 1 \right)^{\frac{-\gamma}{\gamma-1}} \right] \quad (23)$$

The time delay equation is

$$\tau \frac{d\psi}{dt} + \psi = \psi_{QS} \quad (24)$$

which is similar in form to Equation 15. Note that in addition to the measured variables required to estimate the pressure coefficient, the work coefficient model requires the compressor exit physical airflow rate  $w_{31}$ . It must also be mentioned that when these equations are rearranged to provide  $\psi$  as a function of the measured variables, the model becomes singular at zero inlet airflow rate. The IDPAC estimation model formulation for the work coefficient follows the formulation for the pressure coefficient model (see Equations 15 through 20), except that the shape of the quasi-steady work coefficient cannot be fitted well with a polynomial. For this reason, the work coefficient was modelled as a series of linear segments as follows:

$$\psi_{QS} = b_1 s_1 + b_2 s_2 + b_3 s_3 + b_4 s_4 \quad (25)$$

where the input functions  $s_i$  are defined as shown in Figure 27.

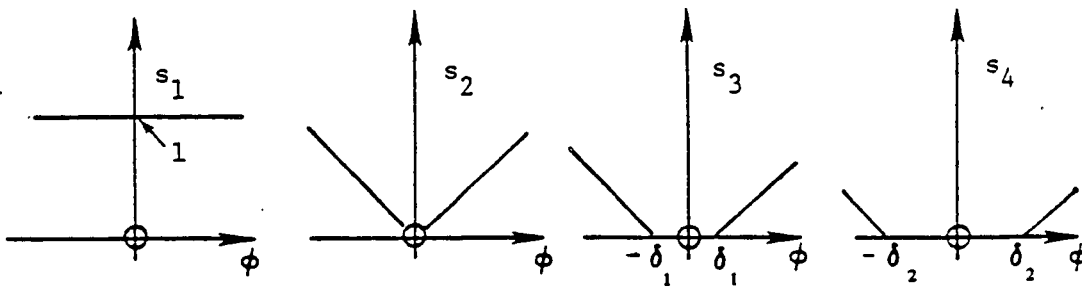


Figure 27. Input Signals For Work Coefficient Estimation.

### 6.3 Pressure Coefficient Estimation

The first case to be estimated was the 98.5 percent corrected speed case. However, before the estimation could be accomplished, two preliminary steps had to be taken to prepare the data. The first step was to obtain a segment of data during which the surge cycles were well developed and uniform. The second step was to segment the data into in-stall and unstalled regions.

The data used in the estimation process was the time segment between 1.6 and 3.7 seconds of the transient, part of which is shown in Figures 14, 15, 16, 17, and 18. Figure 14 shows that the cycles can be separated into unstalled and in-stall regimes by choosing as a criterion the passing of the corrected inlet airflow rate through a threshold of about 50 lbm per second. The data was then separated into intervals during which the airflow rate was below this value, which became the in-stall data, and intervals during which the airflow rate is above this value, which became the unstalled data. A study on data segmentation was performed in which it was found that the quality of estimation was not highly sensitive to using the exact value of 50 lbm per second. In fact, deviations of 8 lbm per second from this value did not cause significant variations in the estimated parameters. Also, the introduction of hysteresis (recovery from stall at a higher airflow rate than the threshold value for going into stall) did not produce much difference in the estimation process. These intervals were then linked to form an in-stall time series and an unstalled time series. The estimation process was then performed on the in-stall time series.

Figure 28 shows the estimated 98.5 percent corrected speed quasi-steady in-stall pressure coefficient. In order to compare the estimated in-stall pressure coefficient to the available steady-state in-stall data, some steady-state data points obtained during 75 percent corrected speed rotating-stall are included in the figure. This comparison has some validity due to the fact, as observed in Subsection 5.2, that an increase in inlet temperature during the 98.5 percent speed instability actually drove the corrected speed down into the 75 percent range. Note that the estimated characteristic is lower than the steady-state data. In comparing the test data and the estimate, it should be noted that they correspond to different in-stall behavior modes. The steady-state data was obtained during low-speed rotating stall. The estimate, however, was obtained from high-speed surge data using a one-dimensional, axisymmetric compressor estimation model. Recently, Greitzer and Moore (Reference 6) have proposed an approximate theory which predicts a difference between the rotating stall and the axisymmetric surge characteristic, the surge characteristic being steeper and lower near the zero flow region. The data presented in Figure 28 seems to support this theory. Also shown on this figure are uncertainty curves which were obtained by varying the estimated parameters plus or minus one standard deviation from their mean value. This standard deviation is obtained from Equation 13.

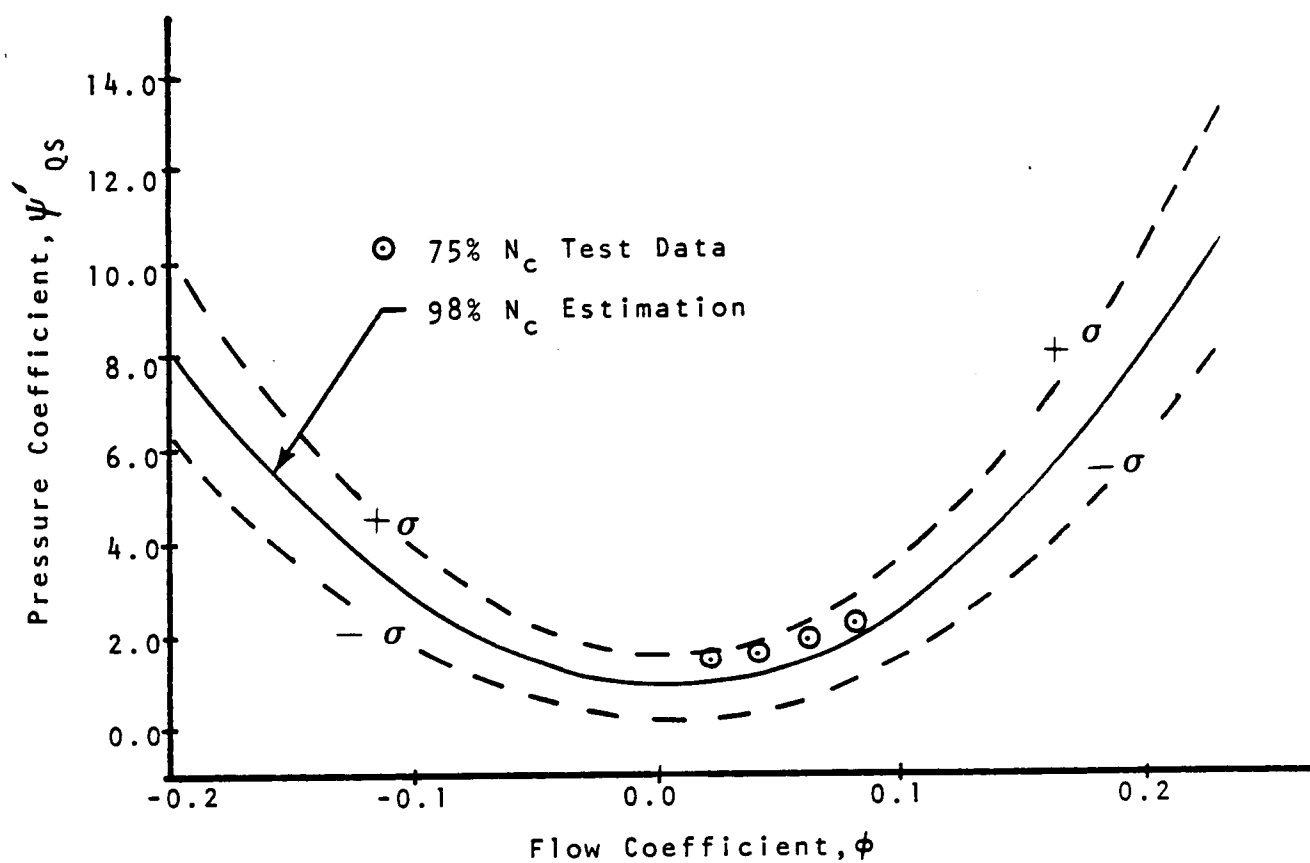


Figure 28. A Comparison Between the 98.5%  $N_c$  Estimated Pressure Coefficient and 75%  $N_c$  Test Data.

The pressure coefficient estimation was attempted using two different input models. Both models use second order polynomials; a "three input" model, given by Equation 20, and a "two-input model", which lacks the linear input term  $s_2$ . Figure 28 is an estimation based on the two-input model.

Figure 29 compares the estimations based on two-input and three-input models. By comparing the loss functions of these two models, it was determined that estimation quality was not degraded by leaving out the first order input  $s_2$ . The justification for this omission is that  $\Psi'$  has generally been found to be an even function of  $\phi$ , or nearly so. QS

Note that these curves can only be considered reliable estimates of the actual in-stall quasi-steady pressure coefficient over the range of high probability density of the flow coefficient as shown by the histogram of Figure 30. This range extends approximately from -0.025 to 0.175.

One of the objectives of this estimation effort was to obtain information on the compressor characteristics during reverse flow conditions. Recall from Subsection 5.2 that at the beginning of the 98.5 percent speed surge transient, there was a significant amount of reverse flow. However, once the surge cycles become established little reverse flow was evident. This can be seen in Figure 15. This is also obvious from the histogram shown in Figure 30. Unfortunately, the low probability density in the reverse flow region also indicates that the characteristic estimation in that region lacks credibility. For this reason, in-stall data from a 90 percent speed instability was also used in the pressure coefficient estimation process.

The data segment chosen for the 90 percent corrected speed estimation is the data between 2.0 and 3.7 seconds of the transient. The filtered data used for the pressure coefficient estimation is shown in Figure 31. Note that there is a significant amount of reverse flow at the inlet, and the histogram of the flow coefficient derived from the data shown in Figure 32 indicates a high probability density of the data centered around zero flow, and extending well into the reverse flow region. This histogram shows that the estimations based on this data would be valid for flow coefficient values from approximately -0.1 to 0.1. Figure 33 shows the two input and three input estimations of the in-stall pressure coefficient from this data. As in the 98.5 percent speed case, the elimination of the first order input  $s_2$  (i.e., assuming  $\Psi'_{QS}$  is an even function of  $\phi$ ) does not degrade the quality of estimation as measured by the loss function given by Equation 7.

The final test for validation of these estimates was to obtain, as stated in Subsection 6.1, a reconstruction of the output based on the estimated model. IDPAC was used to simulate the deterministic part (no process or measurement noise) of the estimated 90 percent corrected speed two-input model. It should be noted at this point that the

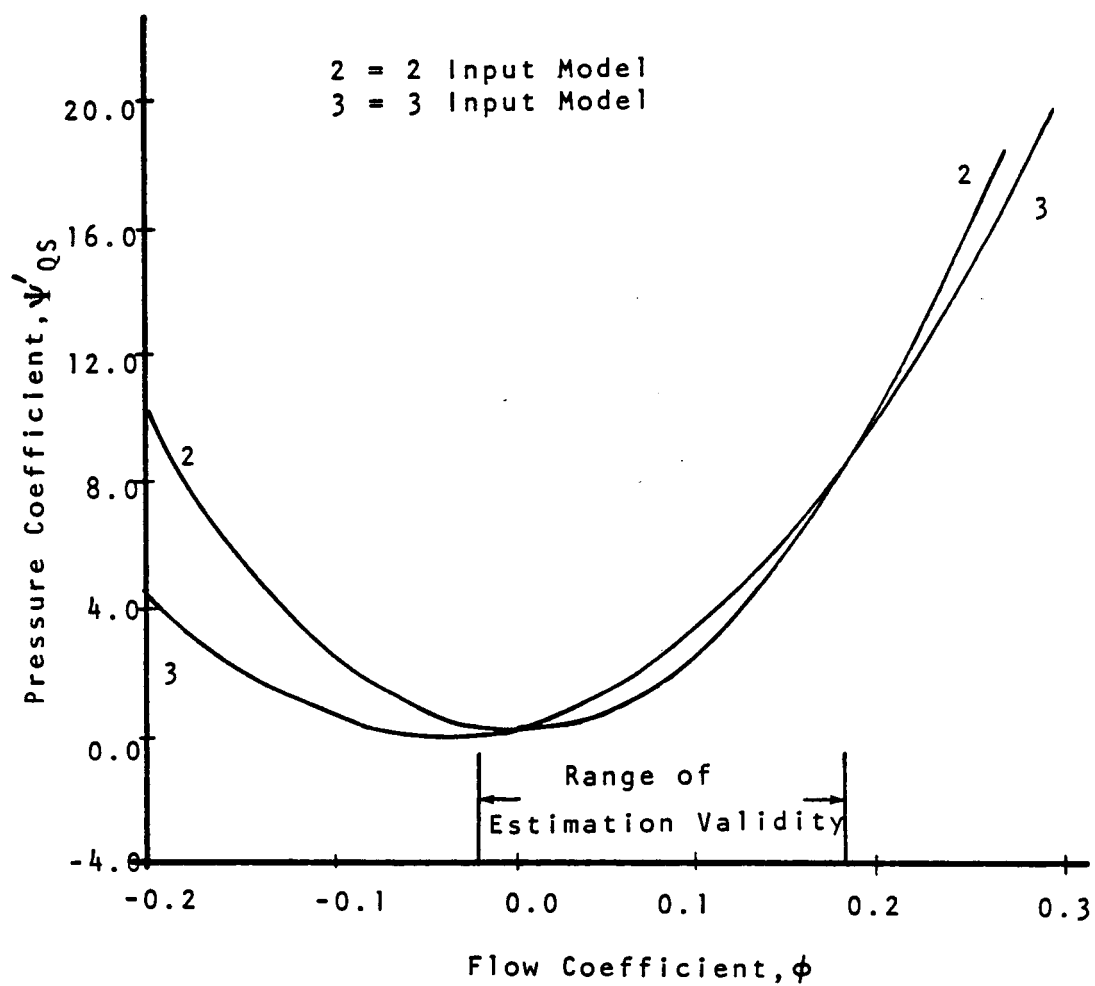


Figure 29. Pressure Coefficient Estimation Models, 98.5%  $N_c$ .

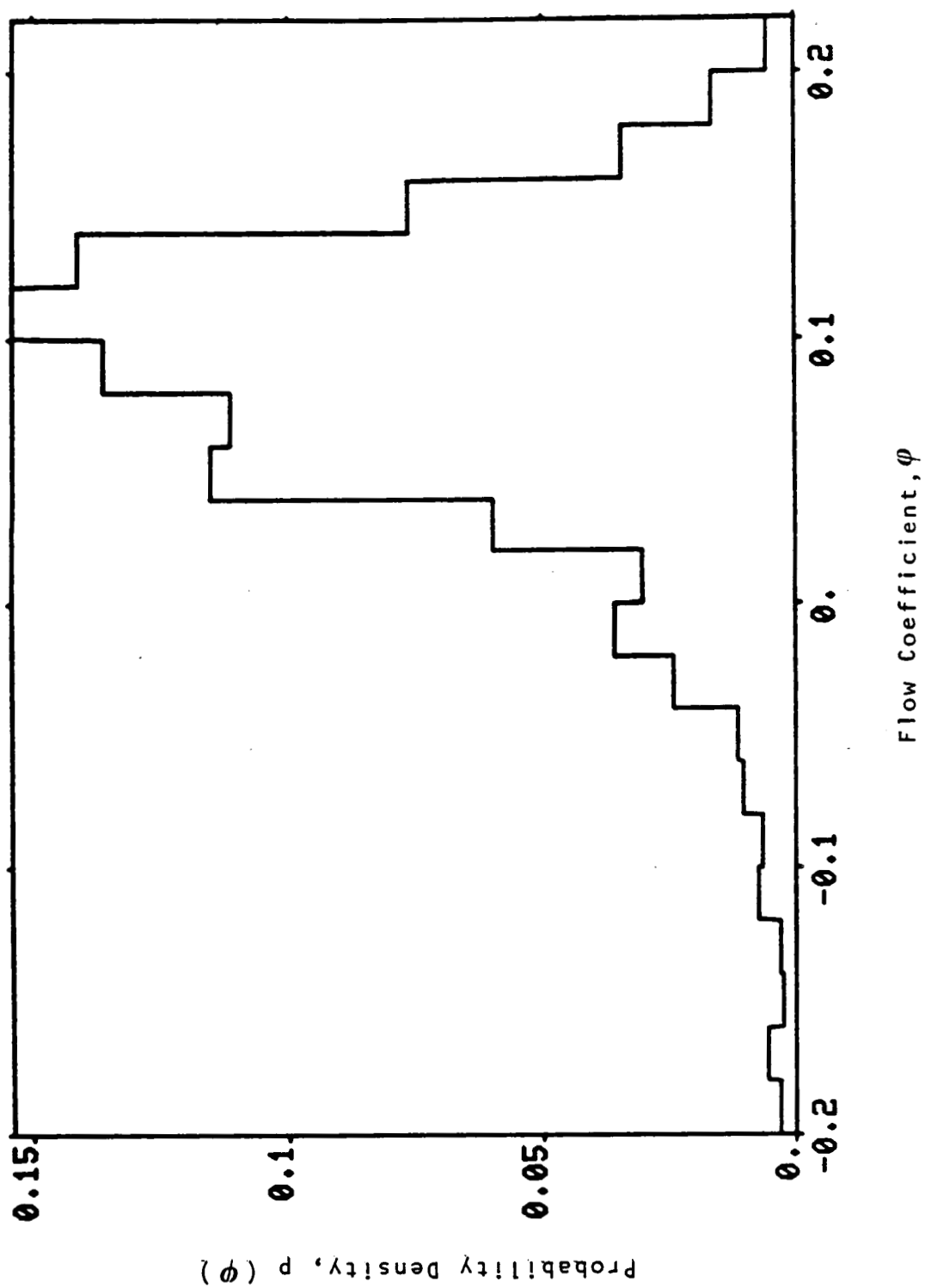


Figure 30. Histogram of In-Install Flow Coefficient, 98.5%  $N_c$ .

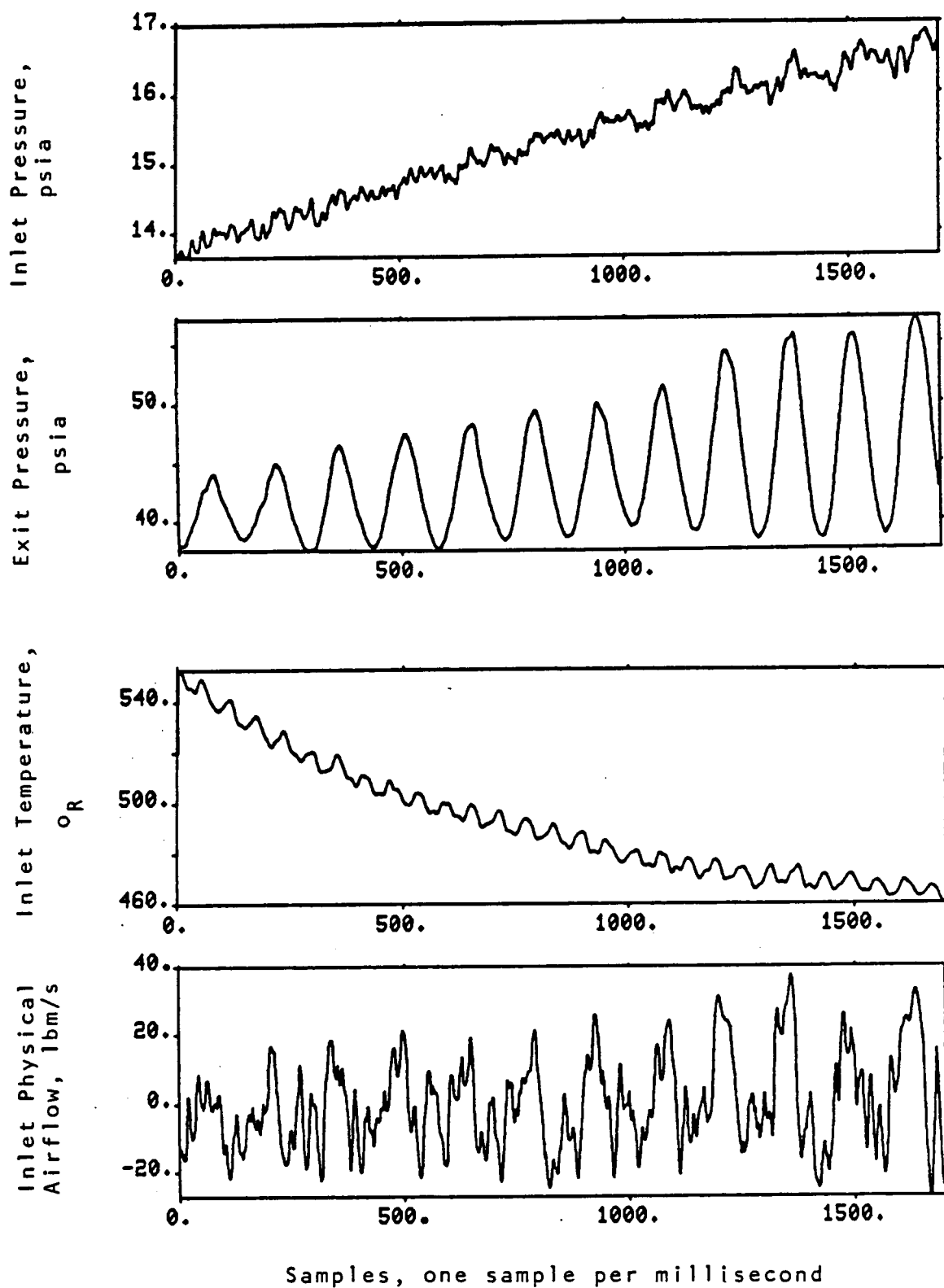


Figure 31. Measured Parameters Used in 90%  $N_c$  Pressure Coefficient Estimation.

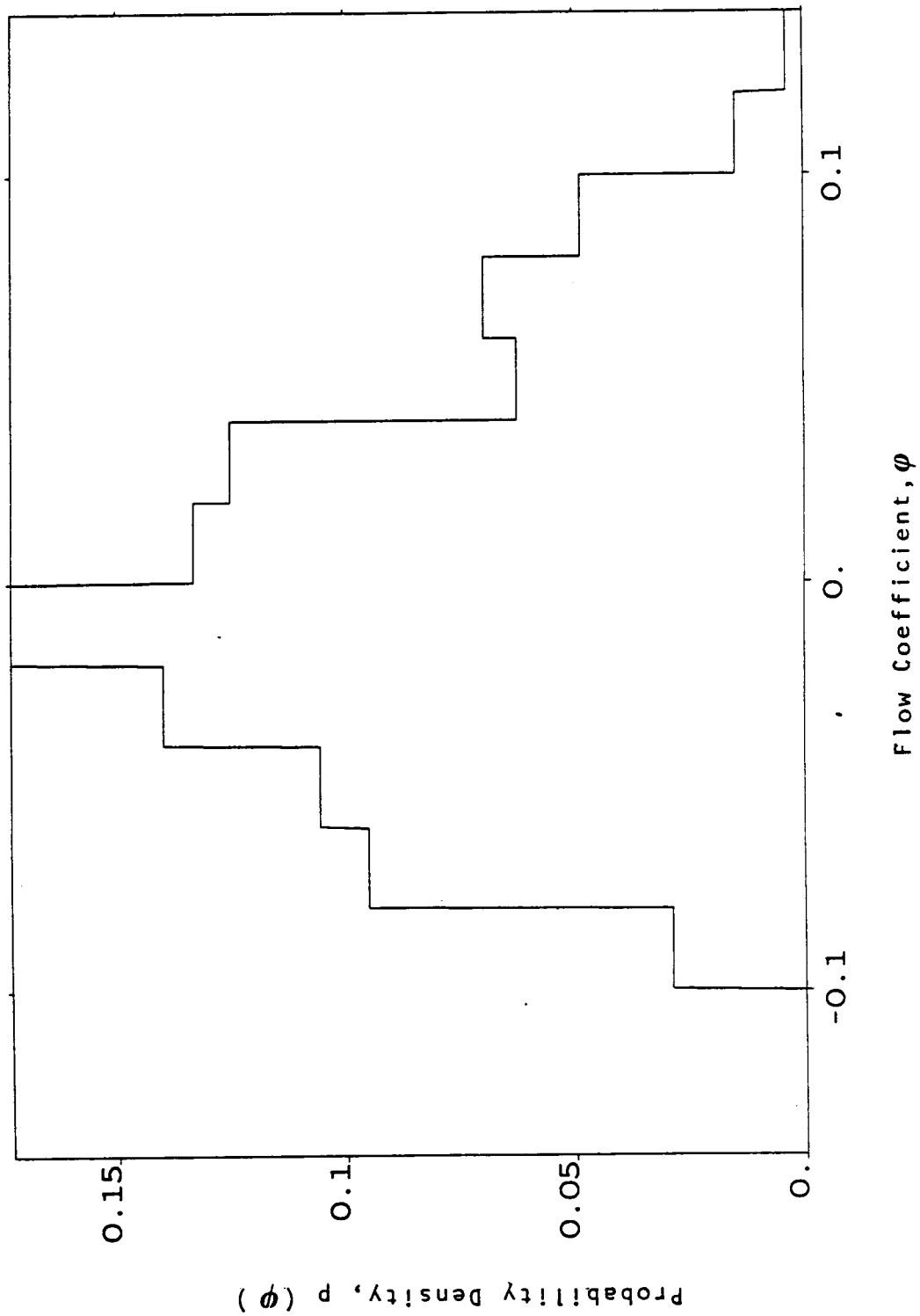


Figure 32. Histogram of the In-Still Flow Coefficient, 90%  $N_c$ .

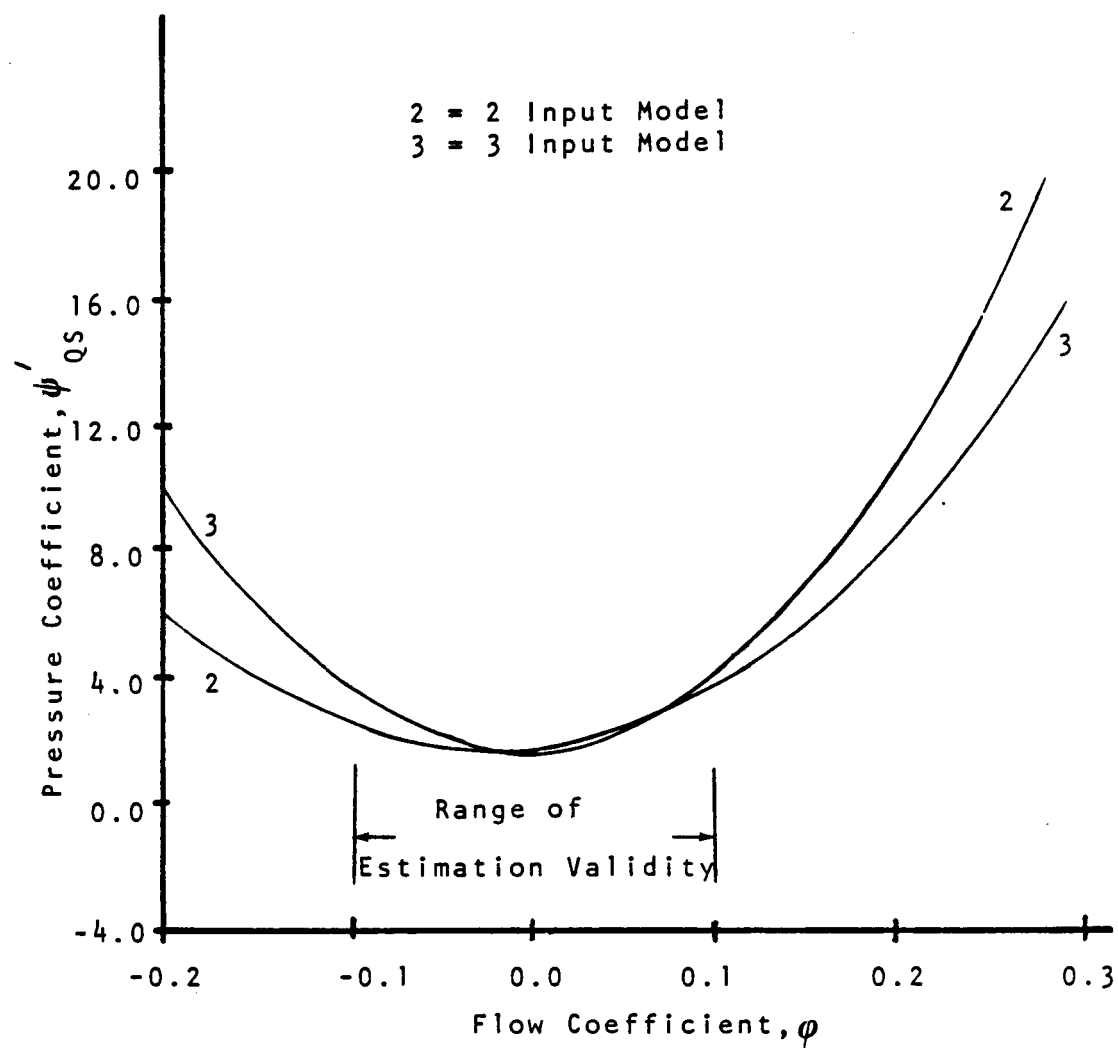


Figure 33. Pressure Coefficient Estimation Models, 90%  $N_c$ .

estimated time constant had to be adjusted to produce this pressure coefficient reconstruction. Applying Equation 19 to the estimated parameter 'a' yields a time constant of 243 milliseconds for the two-input model. From the period of oscillation seen in Figure 31 it can be clearly seen that this is not the time constant for which we are looking. Rather, the estimation process seems to have estimated a time constant in order to fit the system-dependent slow trends observed in the increasing inlet pressure and decreasing inlet temperature observed in Figure 31. A new time constant was then chosen for the estimation model used in the pressure coefficient reconstruction using trial and error. It was found that a time constant of 18 milliseconds yielded an acceptable reconstruction. Figure 34 is a comparison of the actual instantaneous pressure coefficient and its reconstruction based on the estimated model and the measured flow coefficient.

#### 6.4 Work Coefficient Estimation

The work coefficient estimation is a more difficult problem than the pressure coefficient estimation. One reason for this is the shape of the curve; it does not lend itself well to polynomial representation, so a piecewise linear fit must be attempted. The estimation model is more complex, requiring more terms and the exit physical airflow rate as an additional variable; see Equation 22. Also, this model is singular at zero inlet airflow. The problem of singularity at zero flow was solved by limiting the amplitude of the work coefficient at that point. The problem of constructing a piecewise linear fit was simplified by assuming an estimation model similar to the low speed rotating-stall work coefficient, just as was done for the case of the pressure coefficient.

The model requirement of having measurements of exit physical flow rate limited the available data to the 90 percent speed case. This is because at higher speeds the exit temperature went beyond the measurement limits set in the data acquisition system, and temperature is necessary in calculating physical airflow rate. Figure 35 shows the estimated work coefficients of the input model given by Equations 24 and 25. Also on this figure are points representing the 75 percent speed steady-state work coefficient derived from actual test data.

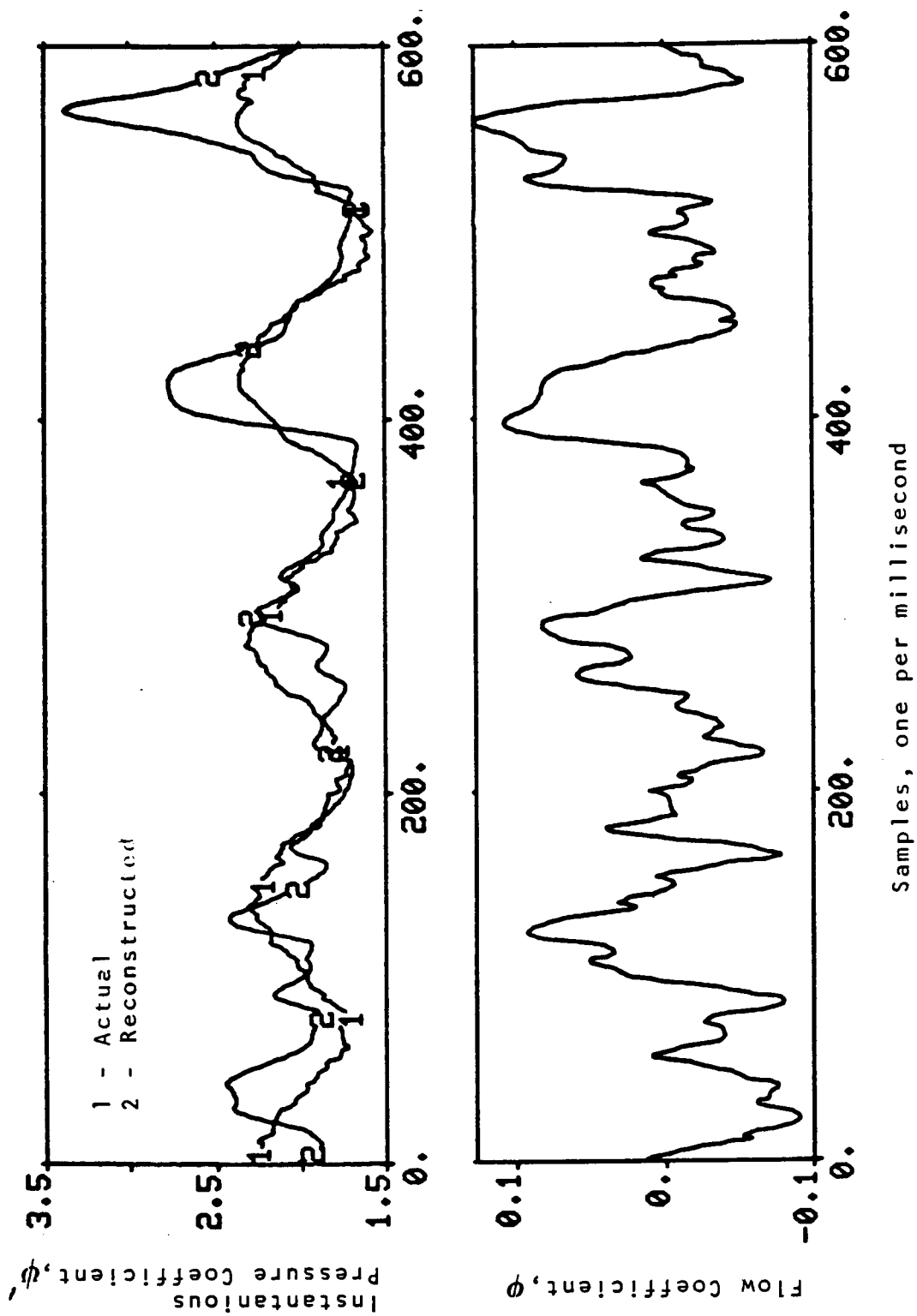


Figure 34. A Comparison of the Actual and Reconstructed Instantaneous Pressure Coefficient, 90%  $N_c$ .

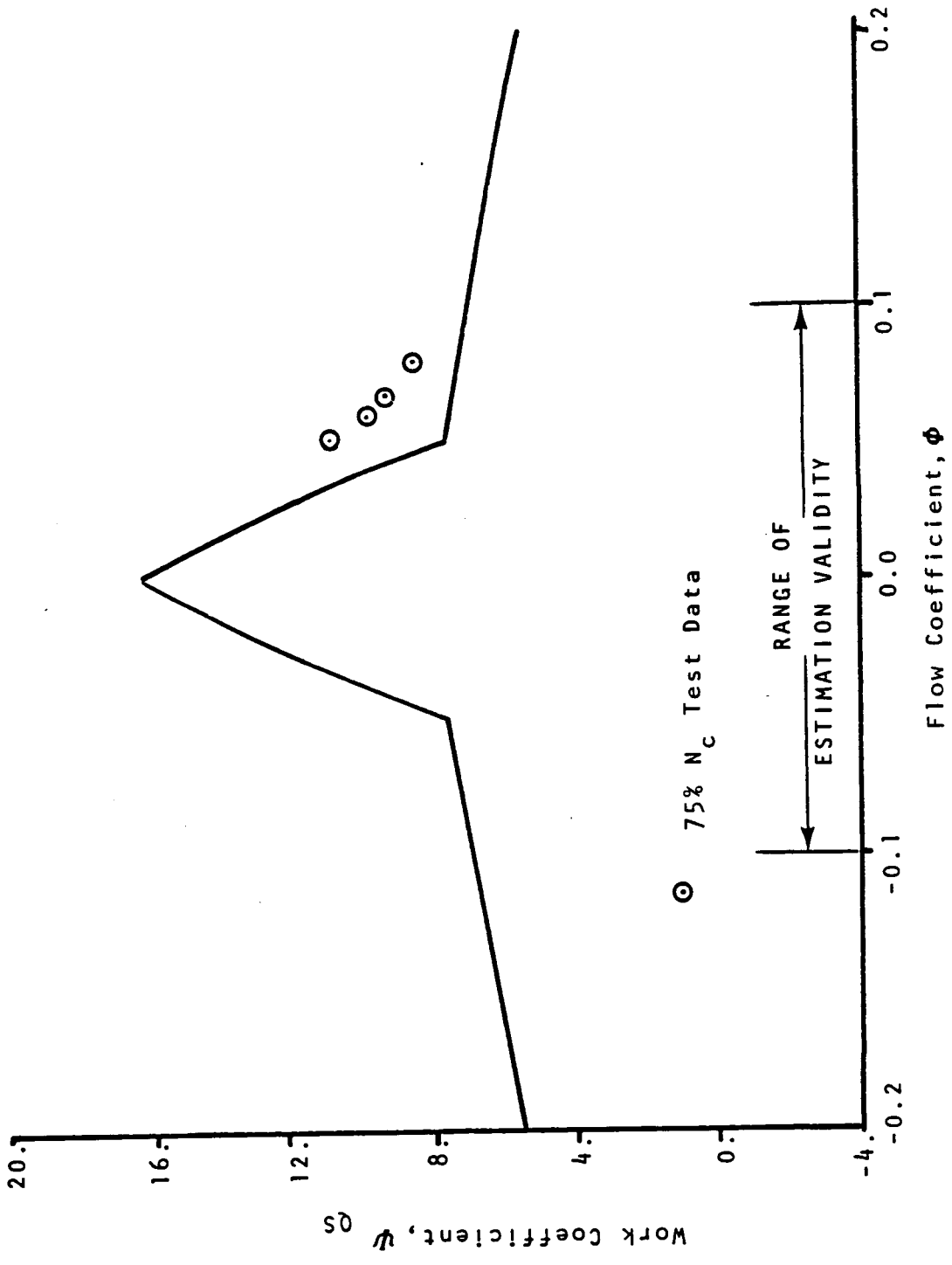


Figure. 35. Work Coefficient Estimation Model, 90%  $N_c$ .

## 7.0 COMPUTER MODEL SIMULATION

In addition to the experimental work and subsequent data reduction, a parallel effort involved the development and verification of a computer model capable of simulating, to a given extent, the nature of the instabilities encountered during the compressor test. This model was tested and verified at both low speed, where instability took the form of rotating stall, and at high speed, where the primary instability was surge.

### 7.1 Model Description

The model is a one-dimensional single-block compressor representation using the overall pressure and work characteristics to specify a given operating speed. The atmospheric inlet duct, compressor, discharge volume, and discharge valve, shown schematically in Figure 9, have been modelled as a set of volumes as shown in Figure 36.

The computer program is a modification of an existing program which has been used for simulating compressor post-stall dynamics. The program was modified and upgraded for the E<sup>3</sup> compressor post-stall simulations. The program numerically solves the three governing equations of mass, momentum, and energy for each volume in an explicit time-marching manner. The equations to be solved are as follows:

$$\frac{d\bar{\rho}}{dt} = \frac{1}{V} (W_2 - W_1) \quad (26)$$

$$\frac{d\bar{W}}{dt} = \frac{g}{L} \left( P_1 A_1 + \frac{W_1^2}{g \rho_1 A_1} + P_2 A_2 - \frac{W_2^2}{g \rho_2 A_2} + F_z \right) \quad (27)$$

$$\frac{d\bar{\rho} \bar{s}}{dt} = \frac{1}{V} (S_1 W_1 - S_2 W_2 + S_F) \quad (28)$$

These time-dependent equations are evaluated based on the actual characteristics of the E<sup>3</sup> compressor. The force and the generated entropy terms  $F_z$  and  $S_F$  are evaluated based on the compressor characteristics in a quasi-steady-state manner:

$$F_z = P_2' A_2 + \frac{(W_2')^2}{g \rho_2' A_2} - P_1 A_1 - \frac{W_1^2}{g \rho_1 A_1} \quad (29)$$

## MODEL REPRESENTATION

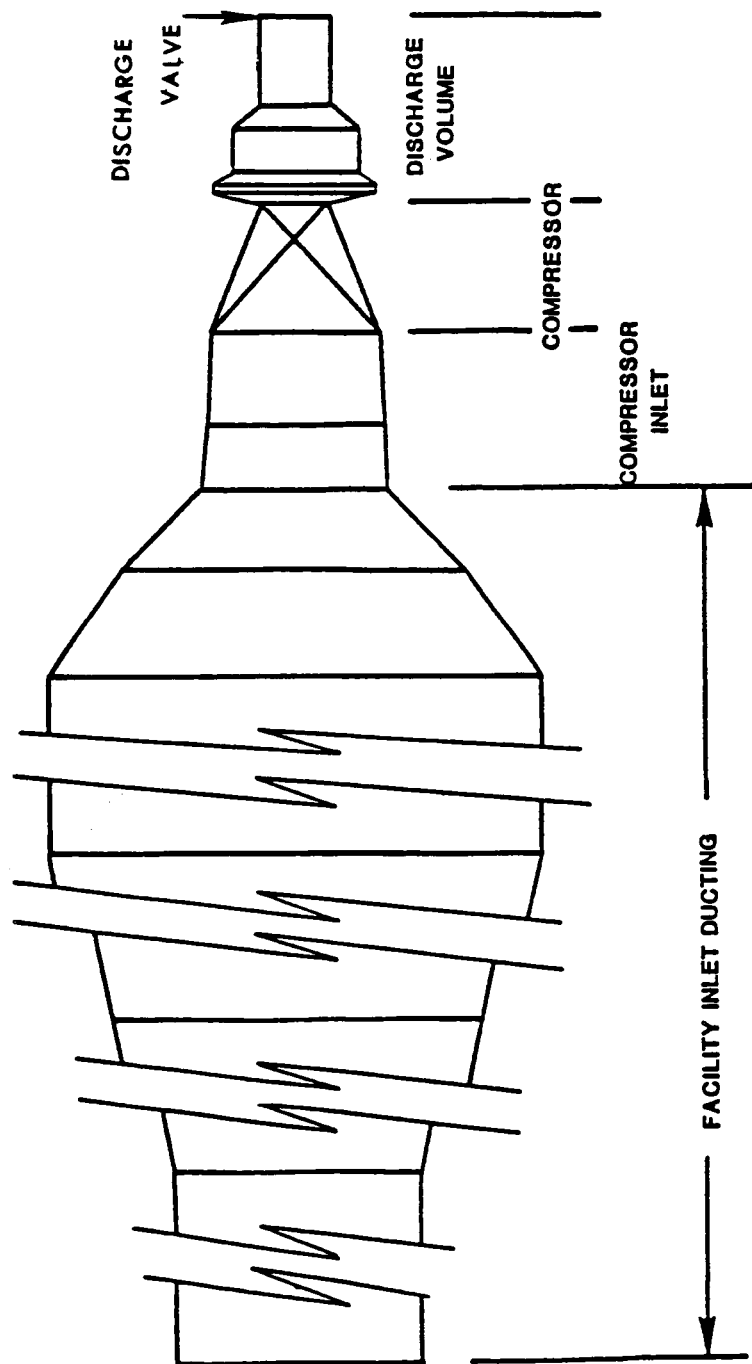


Figure 36. A Schematic of Compressor Rig Model Volumes.

$$S_F = S_2' W_2' - S_1 W_1 \quad (30)$$

where the prime variables ( $P', W', \dots$ ) are evaluated from the instantaneous pressure and work coefficients,  $\Psi$  and  $\Psi$ , using the following relations:

$$T_2' = \Psi \frac{U^2}{2gJC_p} + T_1 \quad (31)$$

$$P_2' = P_1 \left( \Psi' \frac{U^2}{2gJC_p T_1} + 1 \right)^{\frac{\gamma}{\gamma-1}} \quad (32)$$

$$W_2' = W_1 \quad (33)$$

The instantaneous characteristics are related to the quasi-steady-state characteristics by a first order time delay:

$$\tau \frac{d\Psi'}{dt} + \Psi' = \Psi'_{QS} \quad (34)$$

$$\Psi_{QS} = b_1 s_1 + b_2 s_2 + b_3 s_3 + b_4 s_4 \quad (35)$$

The time delay  $\tau$  was experimentally determined by examining stall inception and recovery transients at different speeds. The time constants were found to be a function of speed as shown in Figure 37.

## 7.2 Low Speed Test and Modelling Results

At low speeds, the compressor response to an induced instability was a rapid transient to an equilibrium rotating stall state. The compressor remained in this steady-state condition until the stall was cleared by deliberate action. Steady-state performance readings were obtained while the compressor was in-stall in addition to the normal unstalled performance readings. Figure 38 shows unstalled and in-stall compressor characteristics for 75 percent corrected speed based on these steady state readings. Note that while reading numbers 328 and 332 define part of the unstalled characteristic, reading numbers 329, 330 and 331 lie on the steady-state in-stall characteristic.

A significant amount of stall-recovery hysteresis may be observed in both the pressure and work coefficients. From a steady-state

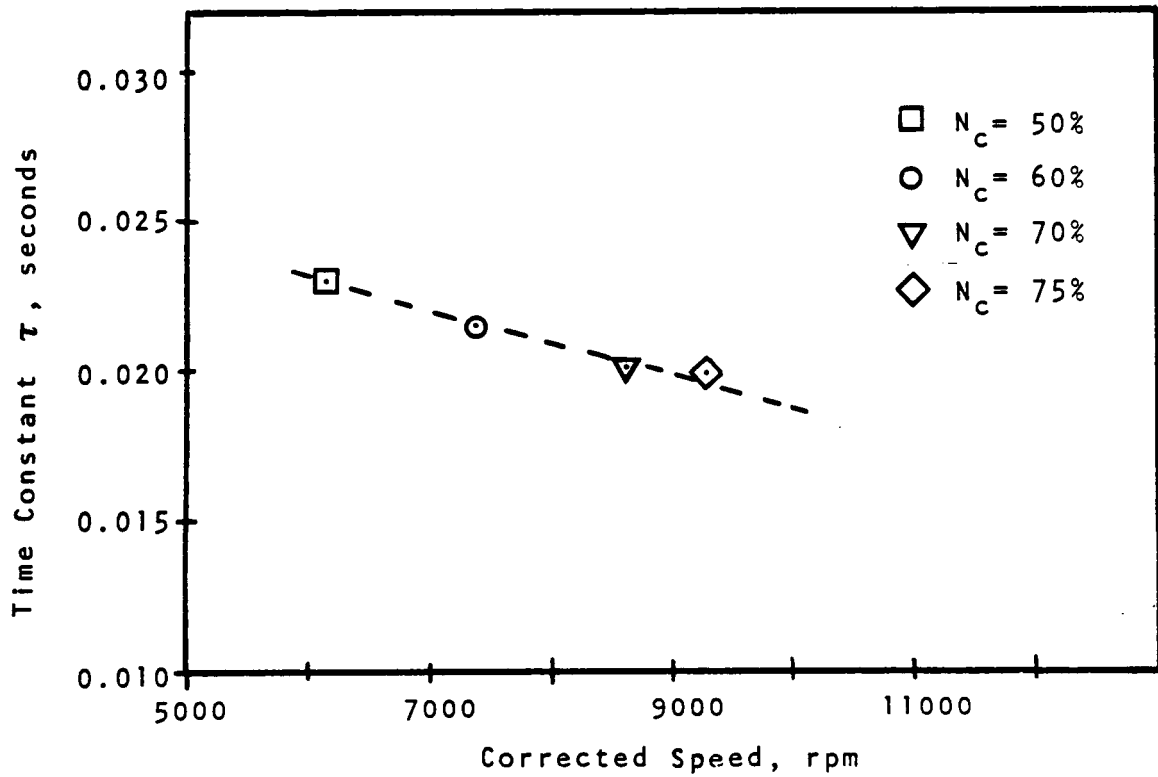


Figure 37a. Stall Inception Time Constants.

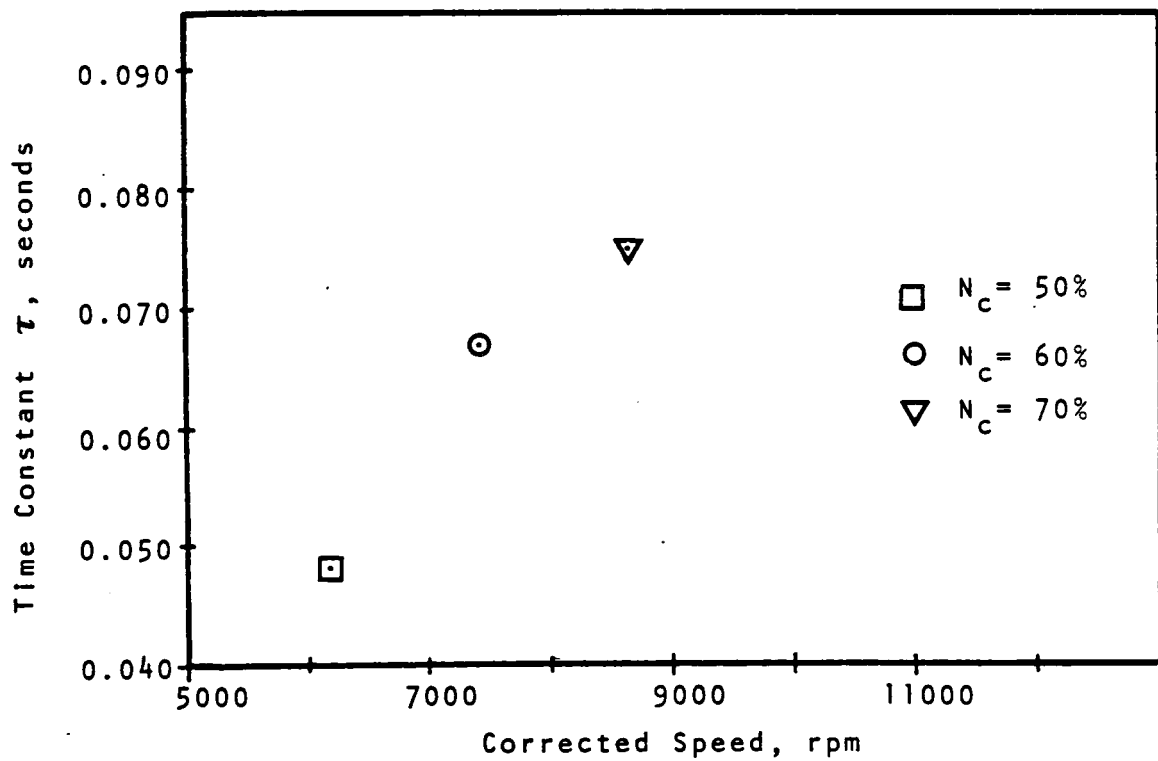


Figure 37b. Stall Recovery Time Constants.

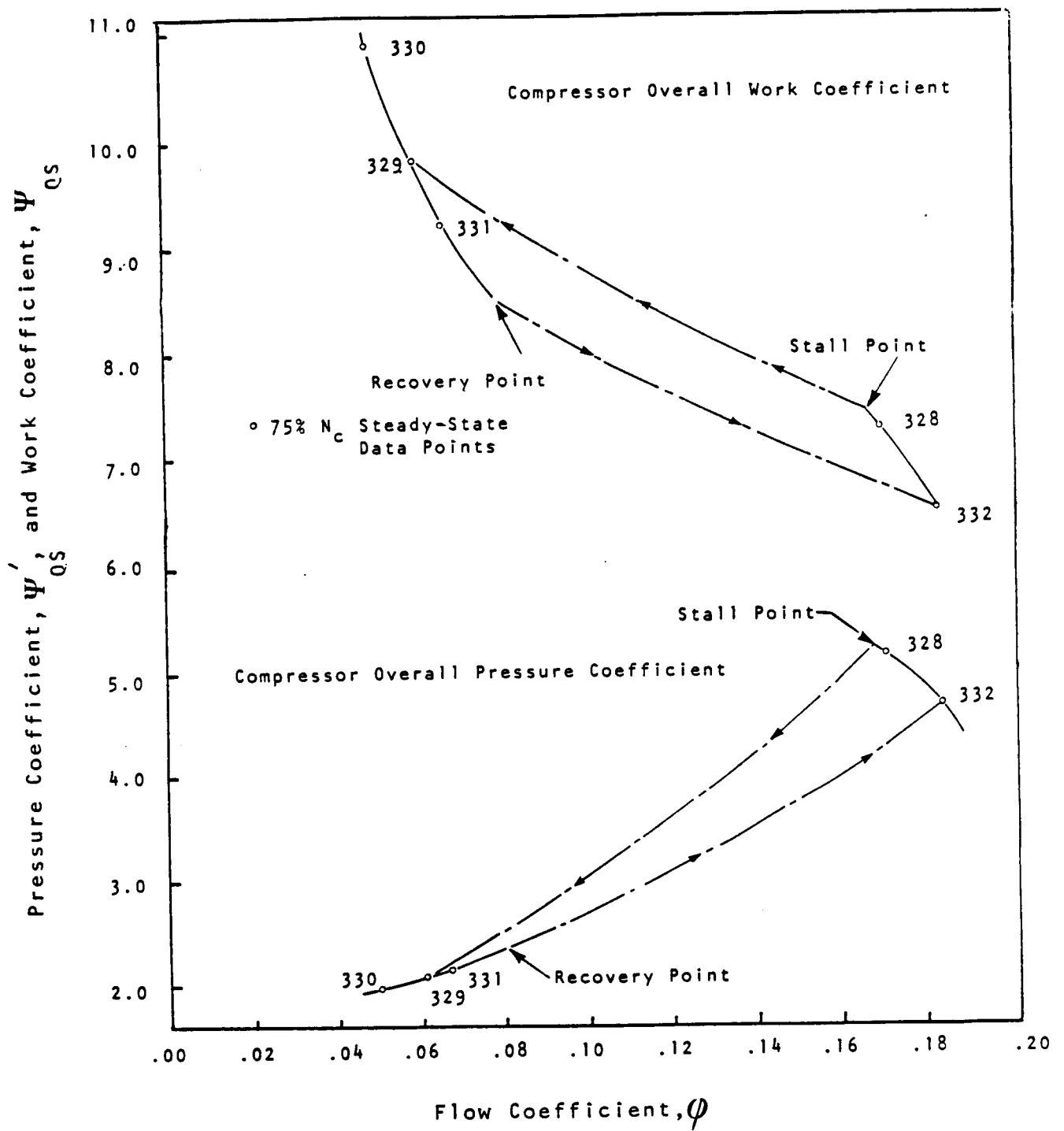


Figure 38. Compressor Characteristics, 75%  $N_c$ .

operating point at reading 328, the compressor discharge valve was closed until stall occurred. The discharge valve then had to be opened well past the stall initiation setting before recovery would occur. The difference between the discharge valve settings at the stall point and reading 332 is a measure of this hysteresis. Adjustments to the model's stall-recovery transition logic were made to account for this hysteresis.

The transition from the unstalled to the in-stall characteristic is transient in nature and cannot be defined in a steady-state manner. Figure 39 is a time history of two airflow rake pressures, one inlet and one exit, responding to this stall transition. The transient oscillations soon damp out, and the compressor settles into steady state in-stall operation at which time reading number 329 was recorded (see Figure 38). The time constant  $\tau$  plotted as a function of speed in Figure 37 and used in Equations 36 and 37 was obtained from the (assumed) first order decay of the exit pressure shown in Figure 39.

In order to simulate the 75 percent corrected speed condition, the curves of the steady-state characteristics shown in Figure 38 were input to the model as the quasi-steady-state characteristics of Equations 36 and 37; the time constant used in these equations was input from Figure 37. The speed and initial conditions for the simulation were determined from reading number 328. The model was then used to simulate 75 percent corrected speed stall development. A plot of compressor pressure ratio versus corrected inlet airflow is shown in Figure 40. From this figure it is easy to see the unsteady transition from an unstalled equilibrium point into a series of oscillations which eventually converge on an in-stall steady-state point. Table 2 shows a comparison of these two steady-state points as recorded at the test and as simulated by the model. Figure 41 shows time histories of inlet and exit pressures for this transient.

A comparison of Figures 39 and 41 shows that the model transient is slightly faster and with significantly more oscillation about the in-stall point. Nevertheless, the dynamic response of the inlet pressures are similar: the model yields a 28.5 Hz oscillation which compares well to the 32 Hz oscillations observed in the measured inlet total pressure  $P_{25}$  (this frequency is close to the organ pipe resonance frequency of the duct between the compressor face and the inlet bellmouth). Note also that the inlet pressure responds to the stall inception by first increasing, due to an increase in flow blockage within the compressor and then decreasing to a minimum as the exit pressure nears the end of its decay. The model produces a similar time history.

The model also reproduces a modulation of the inlet pressure oscillations, and both model and test data show that the oscillations increase again in amplitude approximately 0.2 seconds after the stall initiation and decrease again about 0.1 seconds later. This modulation is thought to be caused by interactions between the compressor and the inlet duct.

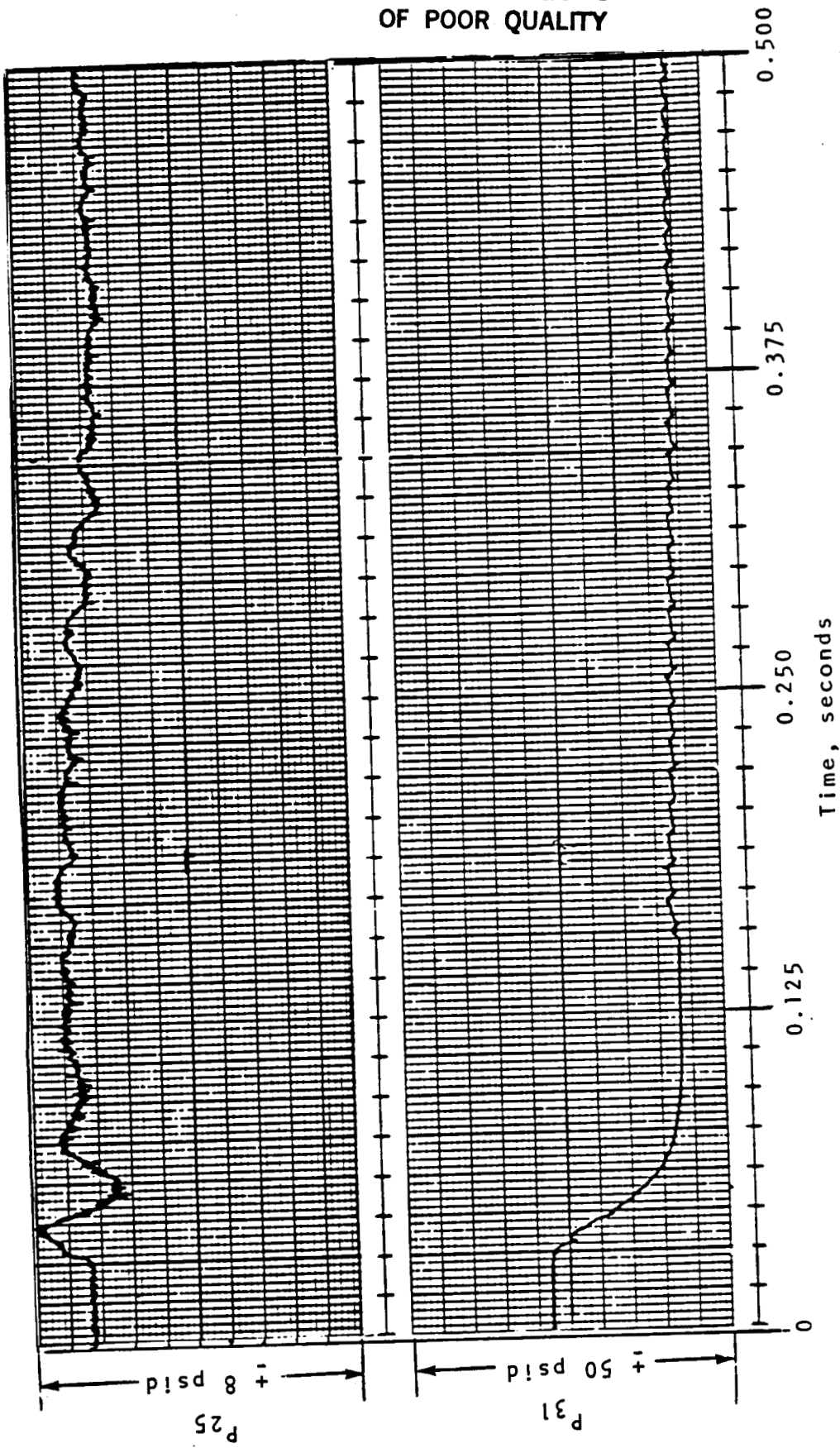


Figure 39. Stall Development, 75%  $N_c$  Test Data.

ORIGINAL PAGE IS  
OF POOR QUALITY

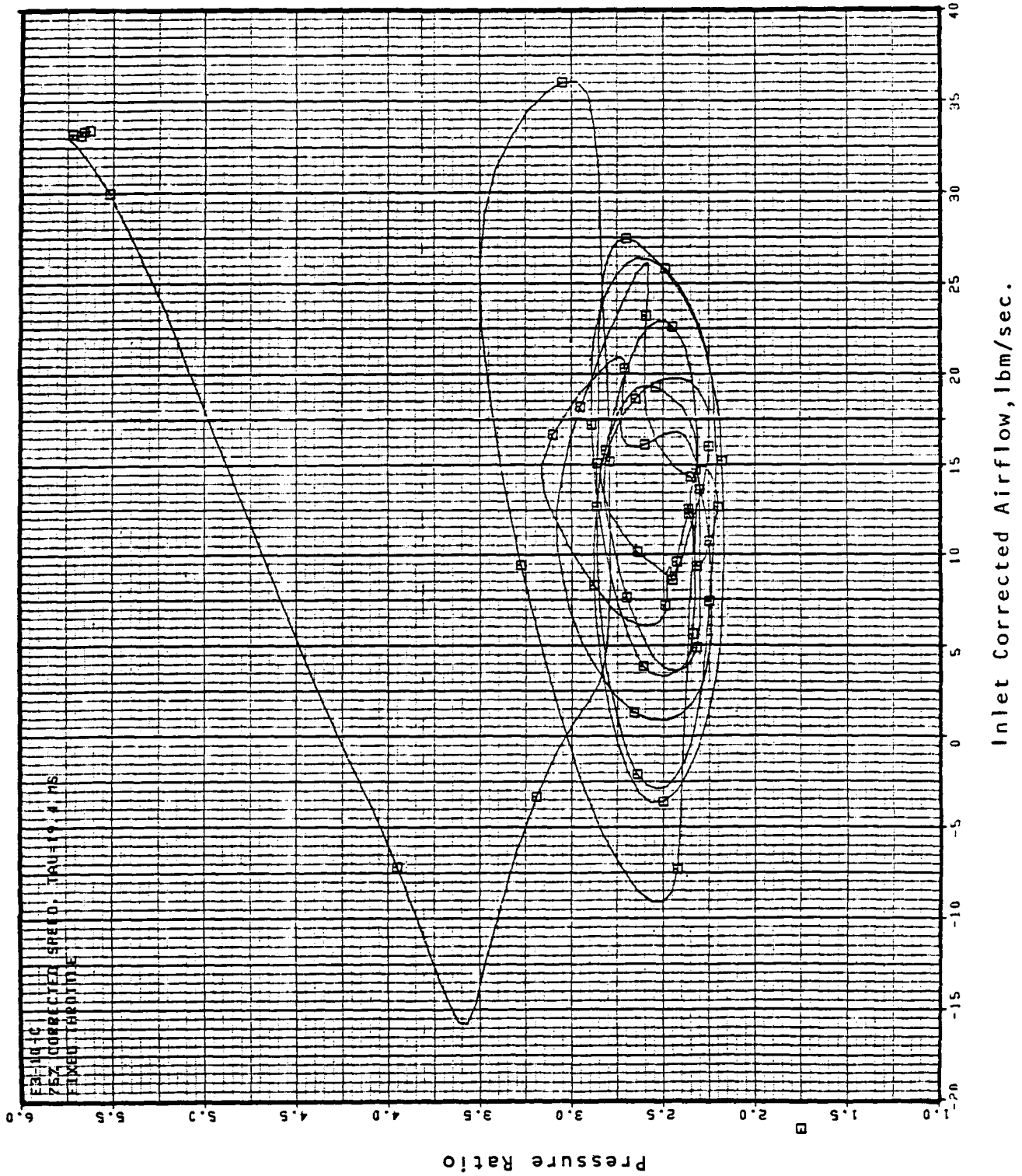


Figure 40. Operating Point Migration, 75%  $N_c$  Stall, Inception, Model Data.

Table 2. A Comparison of Model and Test  
Steady-State Data Points, 75%  $N_c$  Stall.

<u>Measured Parameter</u>	<u>Before Stall</u>		<u>After Stall</u>	
	<u>Model</u>	<u>Test</u>	<u>Model</u>	<u>Test</u>
$P_{25}$ , psia	14.75	14.74	14.75	14.83
$T_{25}$ , °R	492.0	491.6	495.0	491.8
$W_{C25}$ , lbm/sec	34.00	33.58	12.50	12.65
$P_{31}$ , psia	83.00	84.82	35.00	32.56
$T_{31}$ , °R	940.0	935.6	1150	1071

ORIGINAL PAGE IS  
OF POOR QUALITY

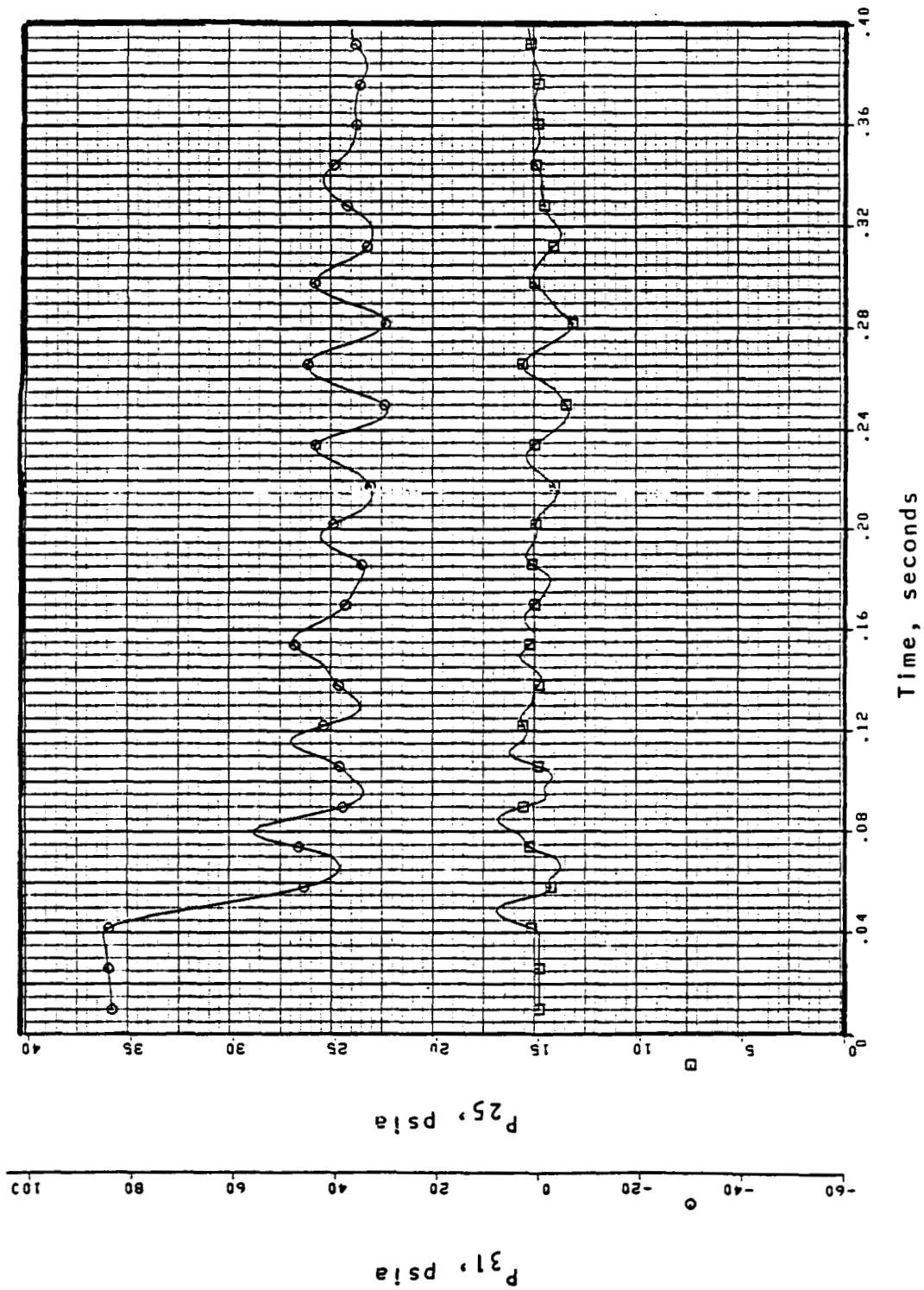


Figure 41. Inlet and Exit Pressure, 75%  $N_c$  Stall Inception, Model Data.

The most significant discrepancies between the model and the transient test data exist in the exit pressure waveforms and are caused either directly or indirectly by the presence of rotating stall cells which could not be simulated in the one-dimensional flow model. The rotating stall cells cause circumferential disturbances in the flow which are readily observable as the 80 Hz oscillations in the test data exit pressure. Not as obvious, however, is the fact that these rotating stall cells, in addition to causing blockage which reduces the overall axial flow, attenuate the compressor inlet pressure fluctuations. The model, which represents the compressor as one block, does not account for this attenuation, and transfers the inlet pressure fluctuations to the compressor exit.

### 7.3 High Speed Modelling Results

The 98.5 percent corrected speed surge case was chosen for simulation because of the fully-developed surge cycles with discernible periods of in-stall and unstalled operation (see Figure 14).

As in the 75 percent corrected speed case, the unstalled characteristics were determined from steady-state test data. However, no steady-state, in-stall data was available at high speed. For this reason, the estimated in-stall characteristics were incorporated in the model. The in-stall work coefficient curve, which was estimated at 90 percent corrected speed, had to be adjusted upward to be consistent with the higher unstalled work coefficient at 98.5 percent corrected speed. The pressure coefficient also had to be adjusted upward slightly to reduce the severity of transition from the unstalled to the in-stall regime which had been causing numerical stability problems. The resultant pressure coefficient curve used in the model is very close to the upper standard deviation curve shown in Figure 28. The unstalled and in-stall compressor characteristics used for the 98.5 percent speed simulation are shown in Figure 42.

As in the test data, fully developed surge cycles were observed in the model output. Figure 43 is a plot of compressor pressure ratio vs. inlet corrected airflow. Examination of this figure shows periods of stall including reverse flow, separated by periods of recovery, which are characterized by a building of pressure at a high airflow rate until stall occurs and the cycle starts again. Figure 44 shows the time histories of the inlet and exit pressures. Note that on this figure also, the data can be visually segmented into stalled and unstalled regimes as is the case with the test data.

It may be observed that the present simulation does not produce the initial transient observed during the 98.5 percent corrected speed surge as shown in Figure 8. The main reason for this difference is that the compressor interaction with the facility exhaust system was not allowed for in the model. Also, two-dimensional effects, such as rotating stall cells which do affect axial flow and pressure fluctuations to a degree, are not reproduced in the one-dimensional model.

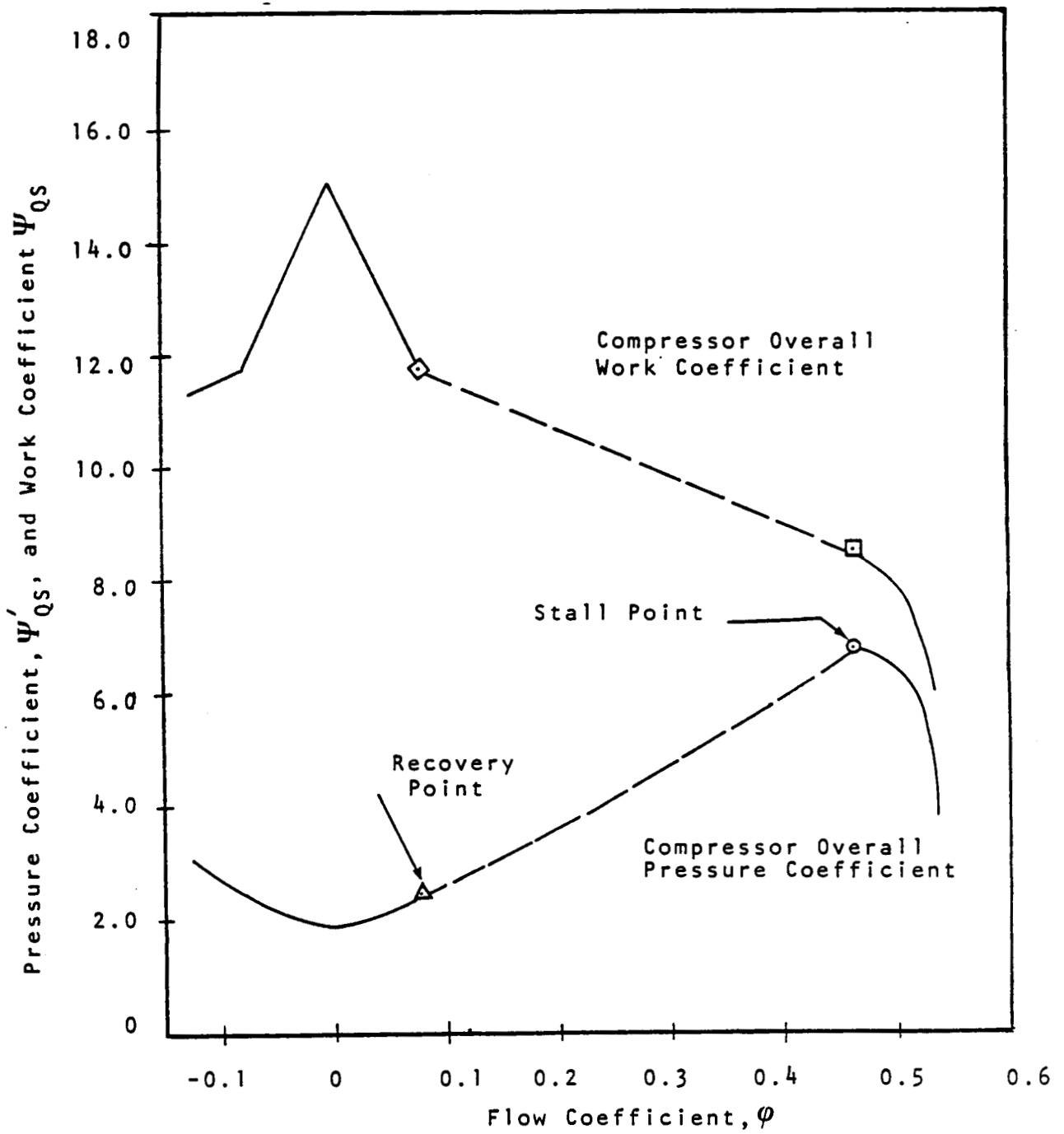


Figure 42. Compressor Characteristics, 98.5%  $N_c$ .

ORIGINAL PAGE-IS  
OF POOR QUALITY

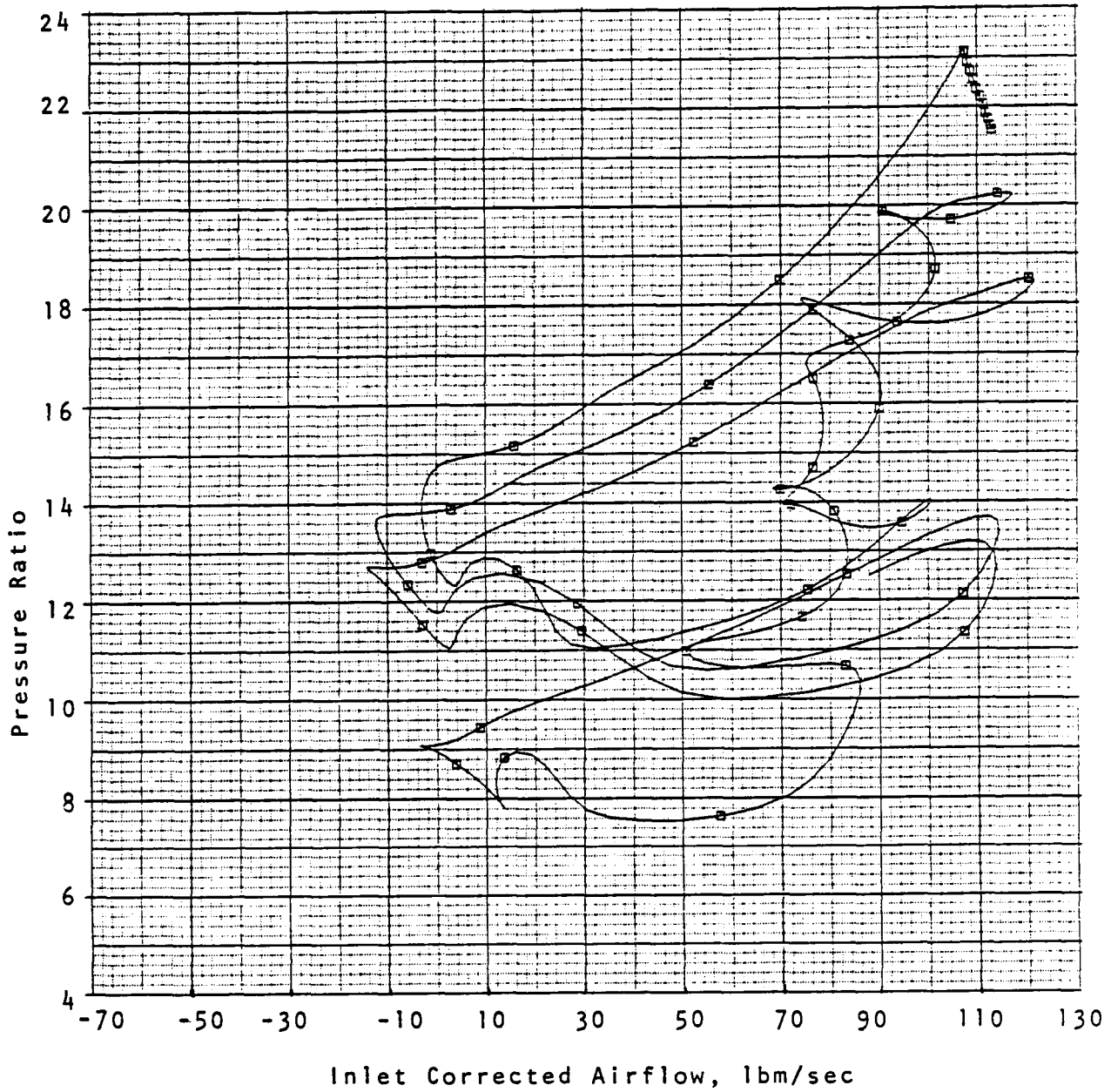


Figure 43. Operating Point Migration, 98.5%  $N_c$  Stall Inception, Model Data.

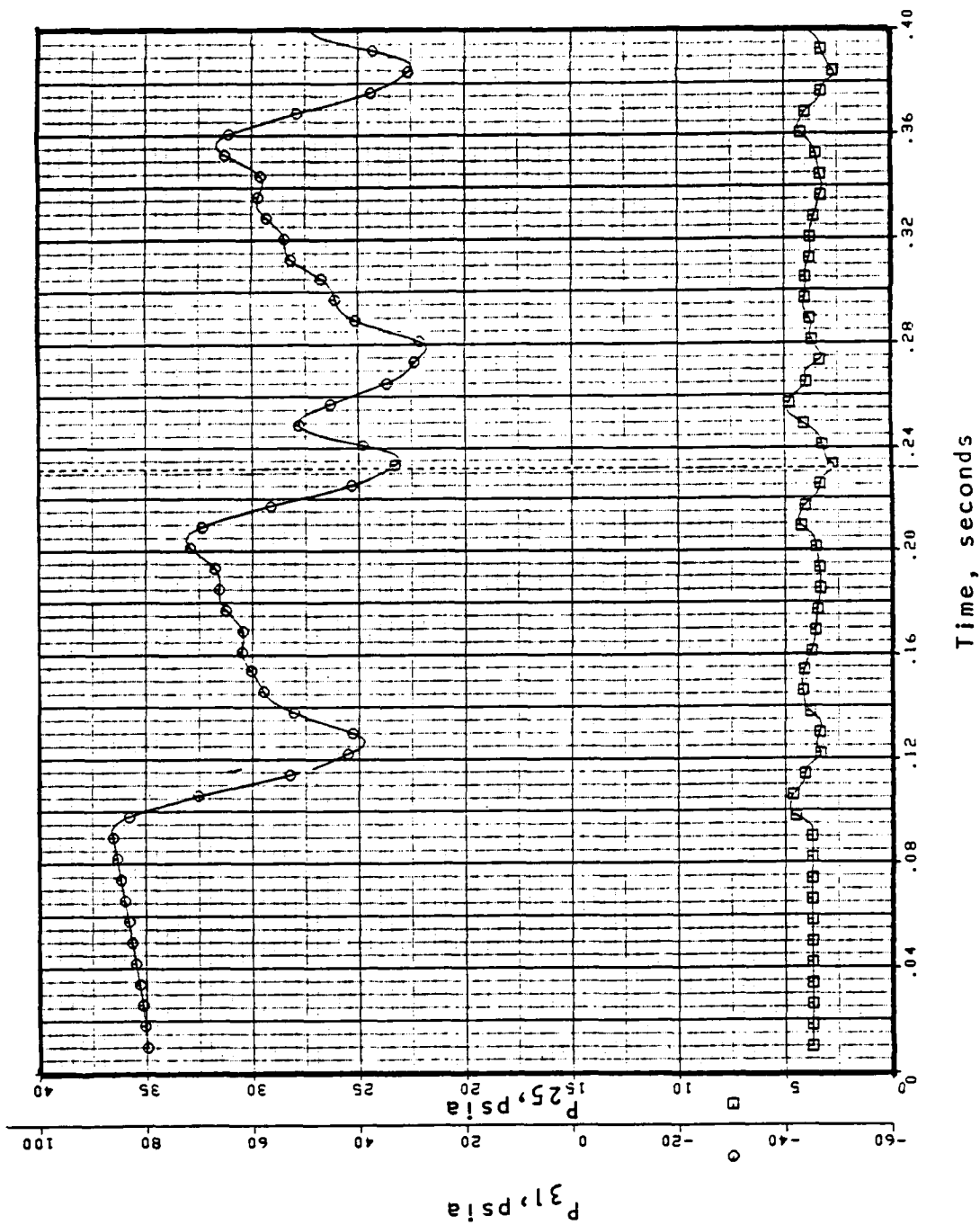


Figure 44. Inlet and Exit Pressure, 98.5%  $N_c$  Stall Inception, Model Data.

Inlet temperature and pressure increases due to the unsteady operation of an upstream refrigeration unit were also neglected due to complexity constraints. This rise in inlet temperature in particular greatly affected the recovery portions of the surge cycles. Figure 43 shows the compressor recovering along the original unstalled speed line and stalling close to the original stall point. The test results, previously shown in Figure 8, show the recovery and subsequent stalls taking place along an entirely different speed line. This was due to the inlet temperature increase which caused a decrease in corrected speed and thus, lowered the pressure ratio and airflow of unstalled operation.

The inability of the model to reproduce the exact surge cycle signature observed during the compressor test does not negate the validity and usefulness of the model. The model was able to reproduce either rotating stall or surge depending only on speed. The differences between test data and model output are to a large extent attributable to necessary simplifications of the compressor rig/facility system.

## 8.0 CONCLUSIONS AND RECOMMENDATIONS

The post-stall compressor test, data reduction, and in-stall compressor characteristic estimation effort documented in this report represents a new direction in high-speed compressor testing and analysis. For this reason, as many questions were raised as answers were found. This effort was of value not only because of the wealth of previously unobtainable high-speed post-stall data that was obtained, but also because of the lessons learned in conducting this sort of test and data analyses.

The airflow rake/ZOC system worked very well in providing compressor inlet and exit pressures, temperatures, and airflows of sufficient quality and resolution so as to allow credible parameter estimates. Nevertheless, improvements to the design of this instrumentation have been proposed, particularly modifications which will allow change out of faulty airflow rake transducers with minimal test scheduling impact. Also, new data reduction systems are in development which will permit on-line data digitization and airflow calculations. In addition, compressor rig test system modifications will be made to minimize the effects of the facility systems and ducting on the post-stall transients.

In spite of the system dynamics superimposed on the post-stall compressor transients, estimation of high-speed pressure coefficients at 90 and 98.5 percent corrected speed and the work coefficient at 90 percent corrected speed were obtained. These estimates were validated by comparing them to the  $E^3$  low-speed rotating stall characteristics. The differences between the low-speed and the high-speed characteristics are consistent with analytical predictions. Also, a reconstruction of the instantaneous pressure coefficient was obtained from the estimated quasi-steady pressure coefficient for the 90 percent speed case. One area of further work is time constant estimation. The estimation procedure yields a very large time constant based on low frequency compressor-facility interactions. Future efforts must address this problem, both to improve the estimation model to allow for decoupling system and compressor dynamics, and to modify the facility and test procedure so that these dynamic interactions may be minimized as much as possible prior to data reduction and characteristics estimation.

The incorporation of the  $E^3$  characteristics into the computer model produced encouraging results. The difference between low-speed instability (rotating-stall) and high-speed instability (surge) which has been predicted theoretically and has been observed in compressor and engine testing was successfully reproduced by this model.

**PRECEDING PAGE BLANK NOT FILMED**

APPENDIX A

High Speed Post-Stall Transients

**PRECEDING PAGE BLANK NOT FILMED**

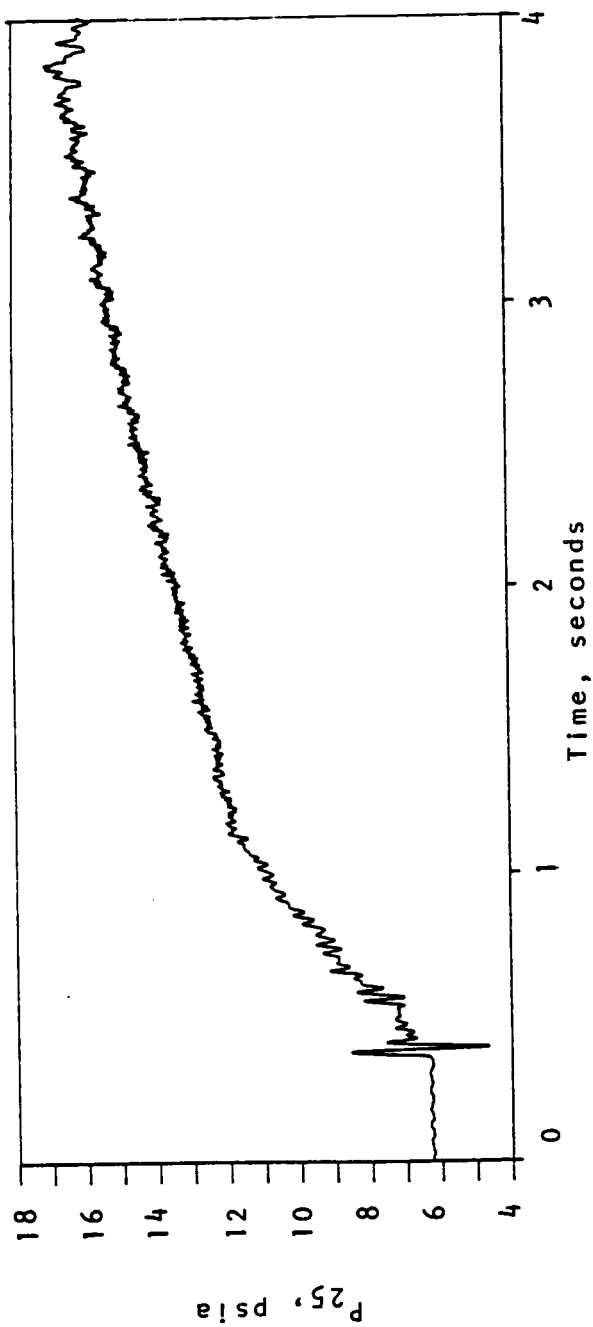


Figure 45. Compressor Inlet Pressure, 90%  $N_c$  Instability.

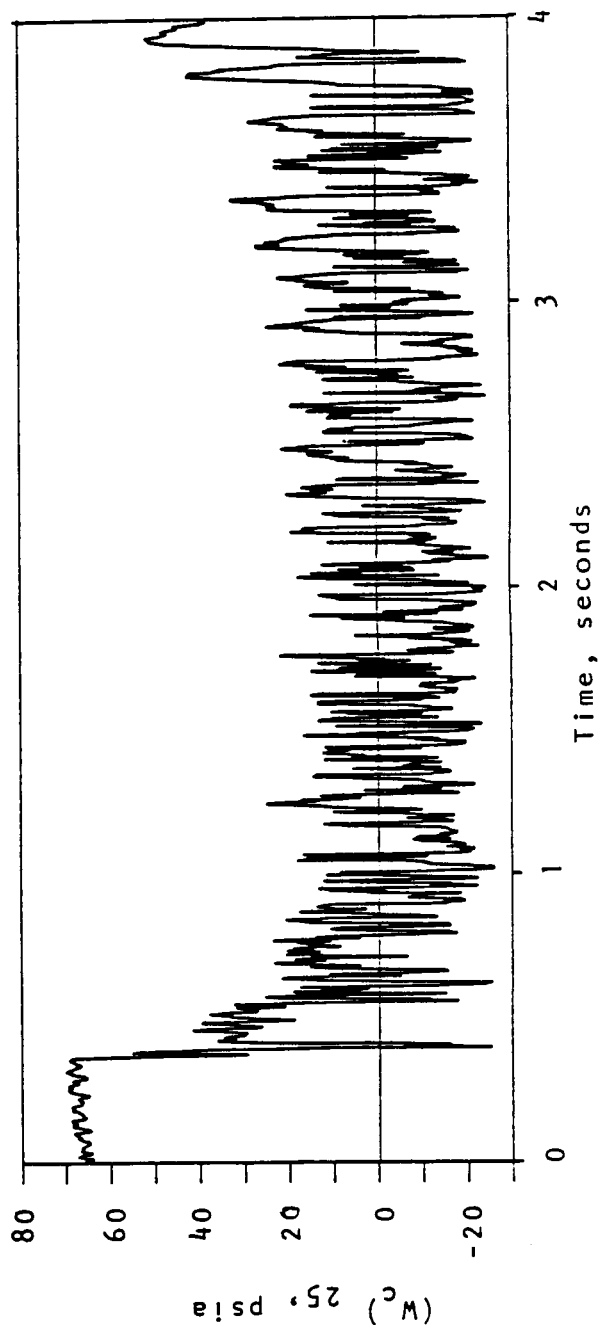
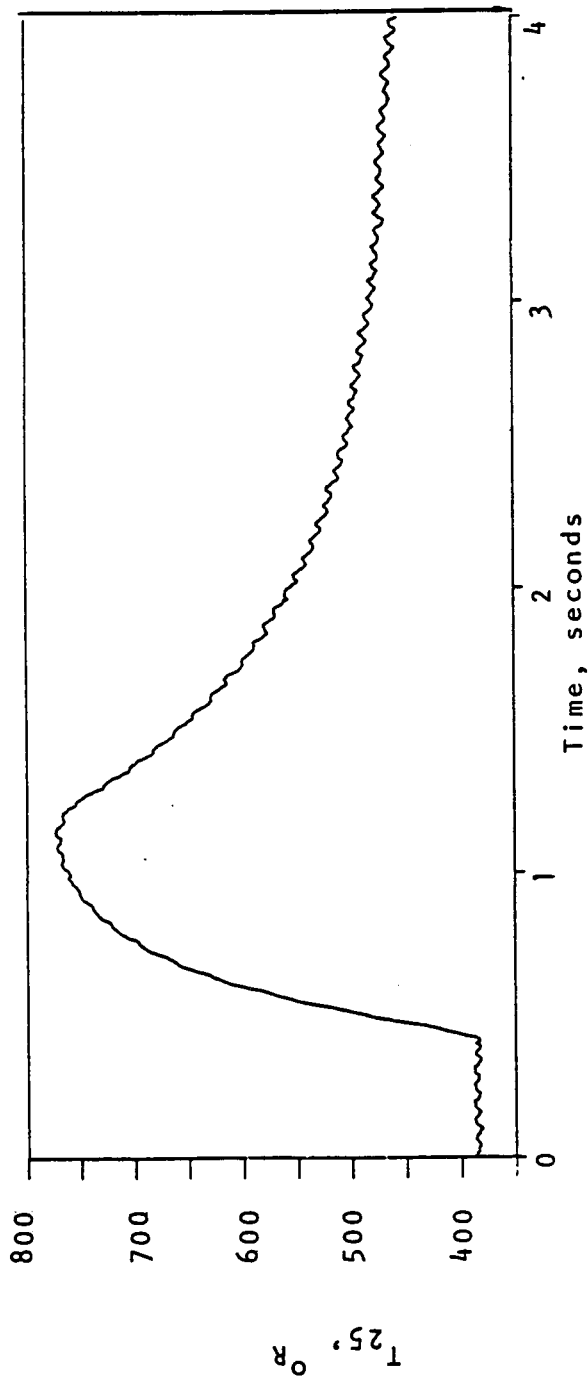


Figure 46. Compressor Inlet Corrected Airflow, 90%  $N_c$  Instability.



75

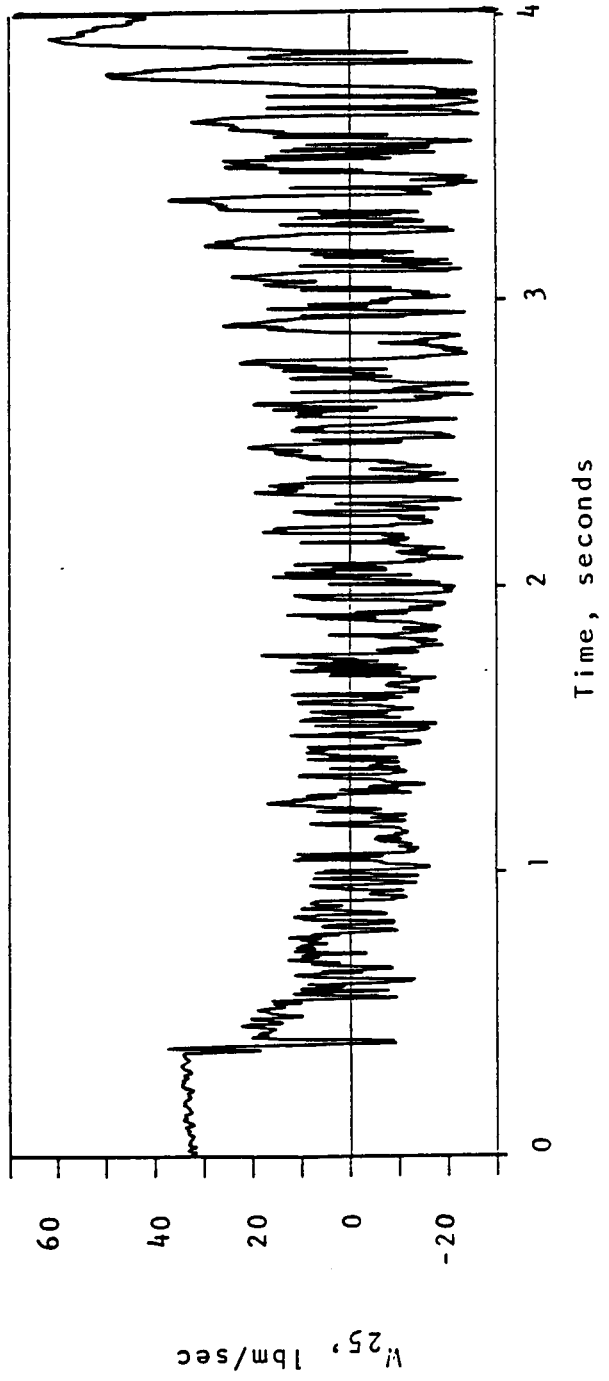


Figure 48. Compressor Inlet Physical Airflow, 90%  $N_c$  Instability.

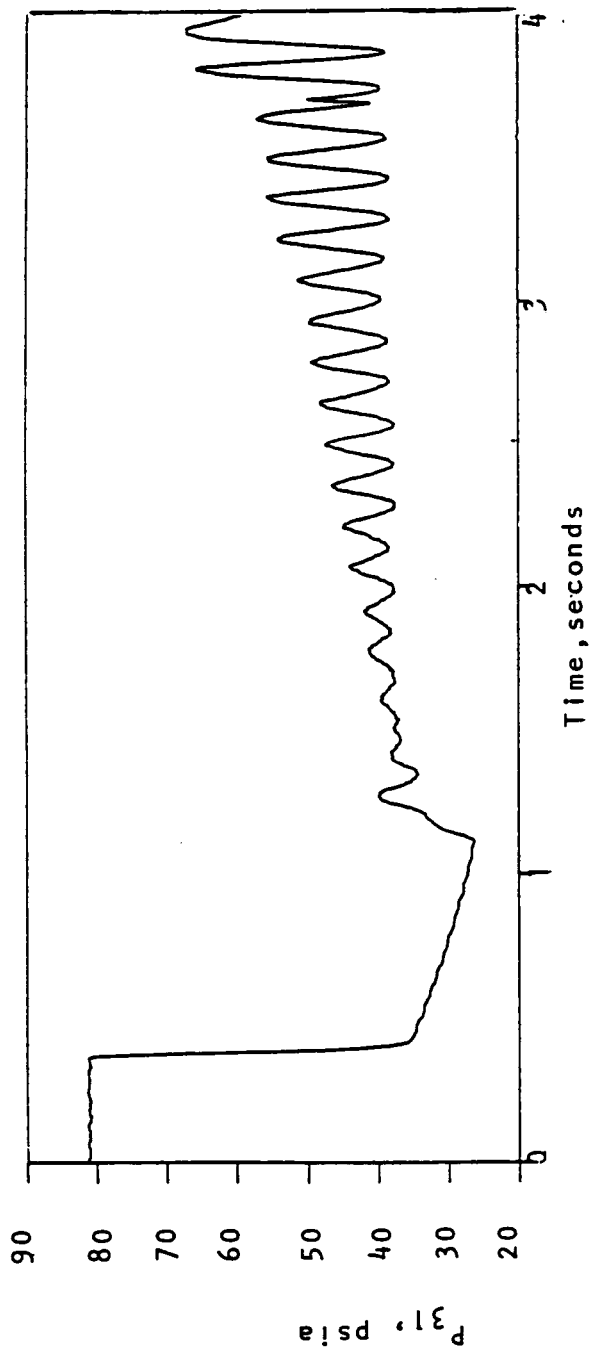


Figure 49. Compressor Exit Pressure. 90%  $N_c$  Instability.

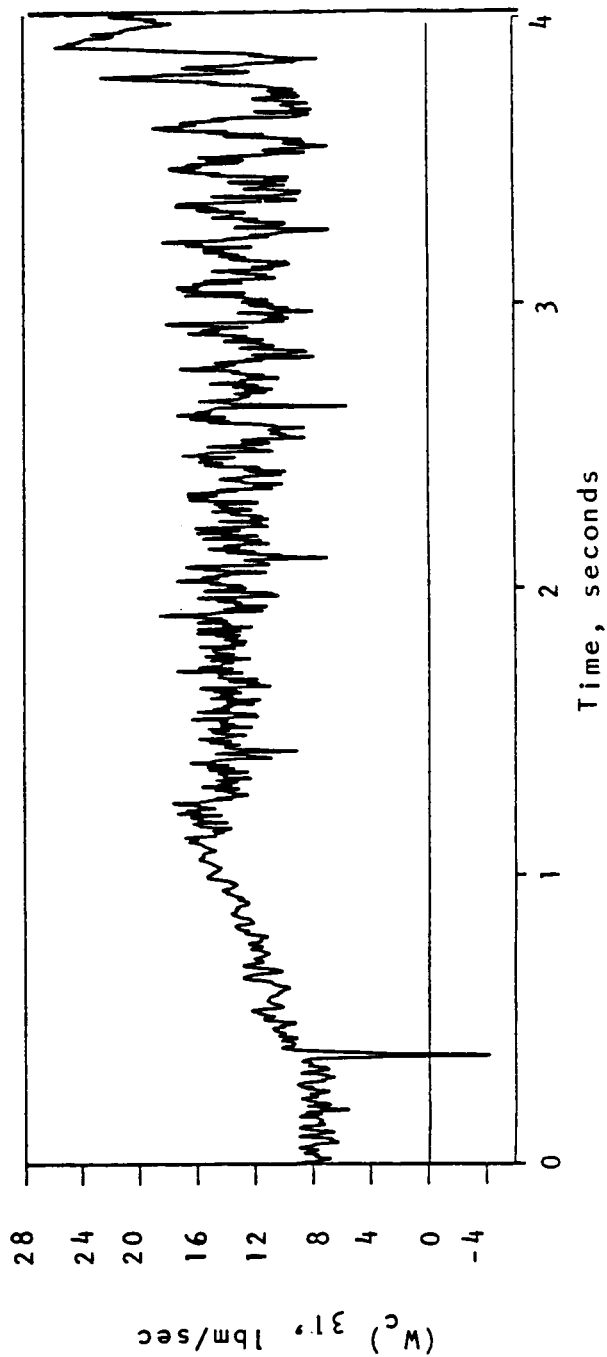


Figure 50. Compressor Exit Corrected Airflow, 90%  $N_c$  Instability.

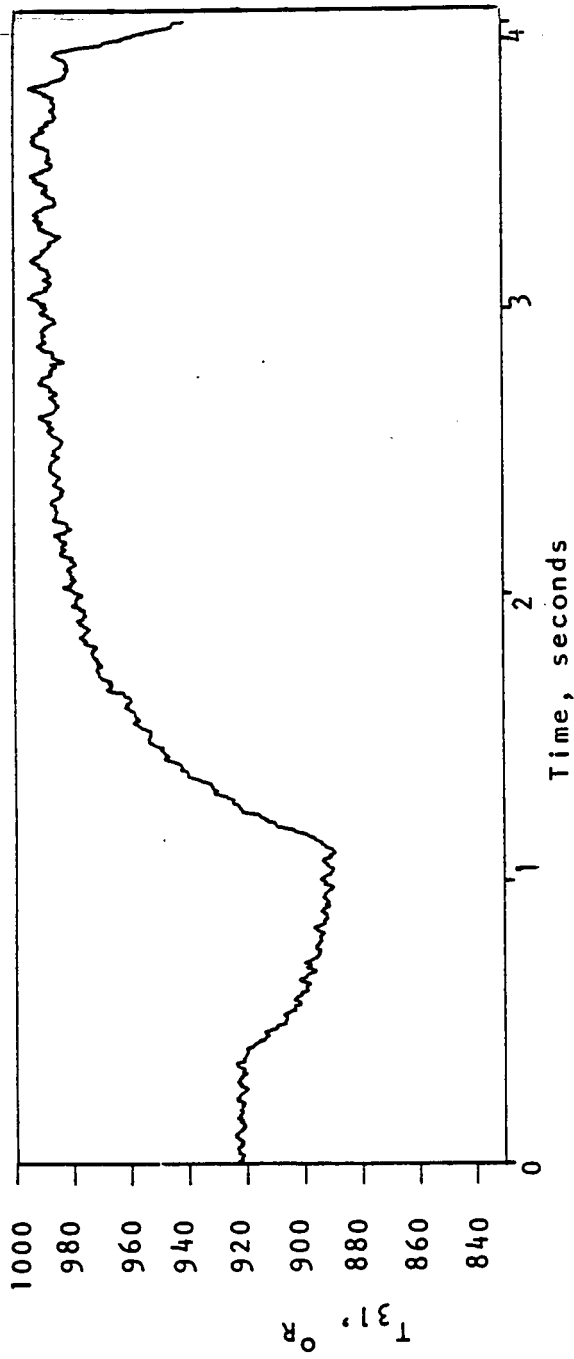


Figure 51. Compressor Exit Temperature, 90%  $N_c$  Instability.

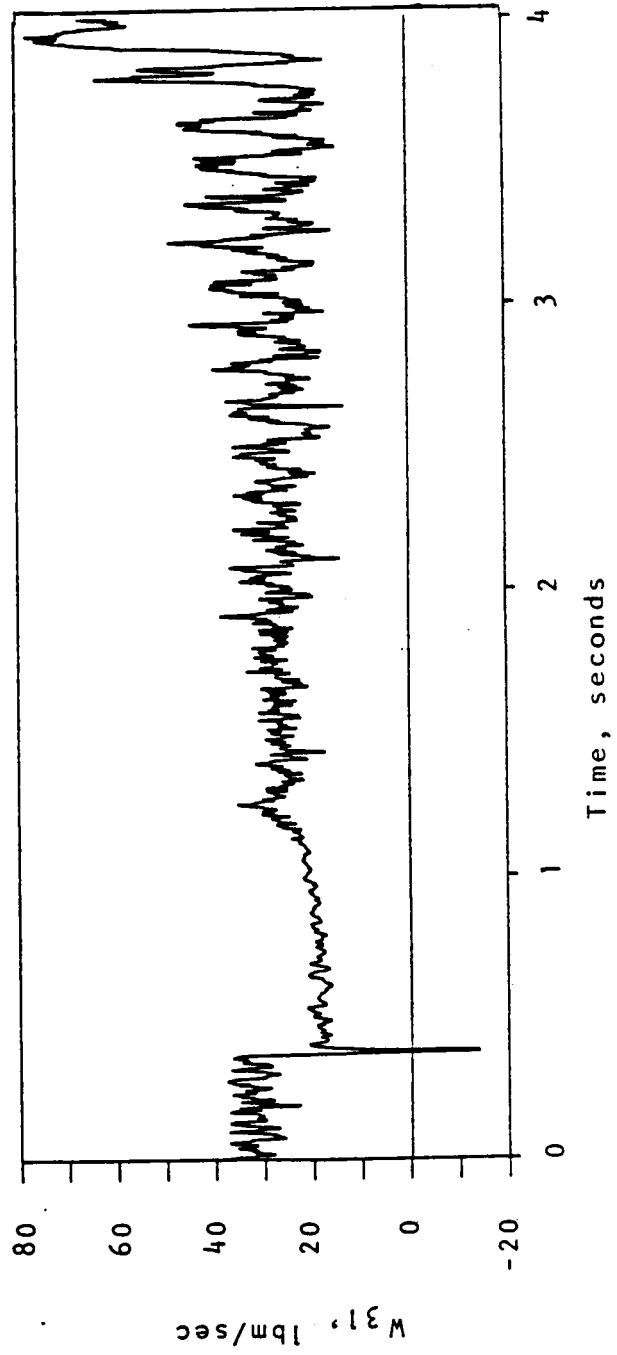


Figure 52. Compressor Exit Physical Airflow, 90%  $N_c$  Instability.

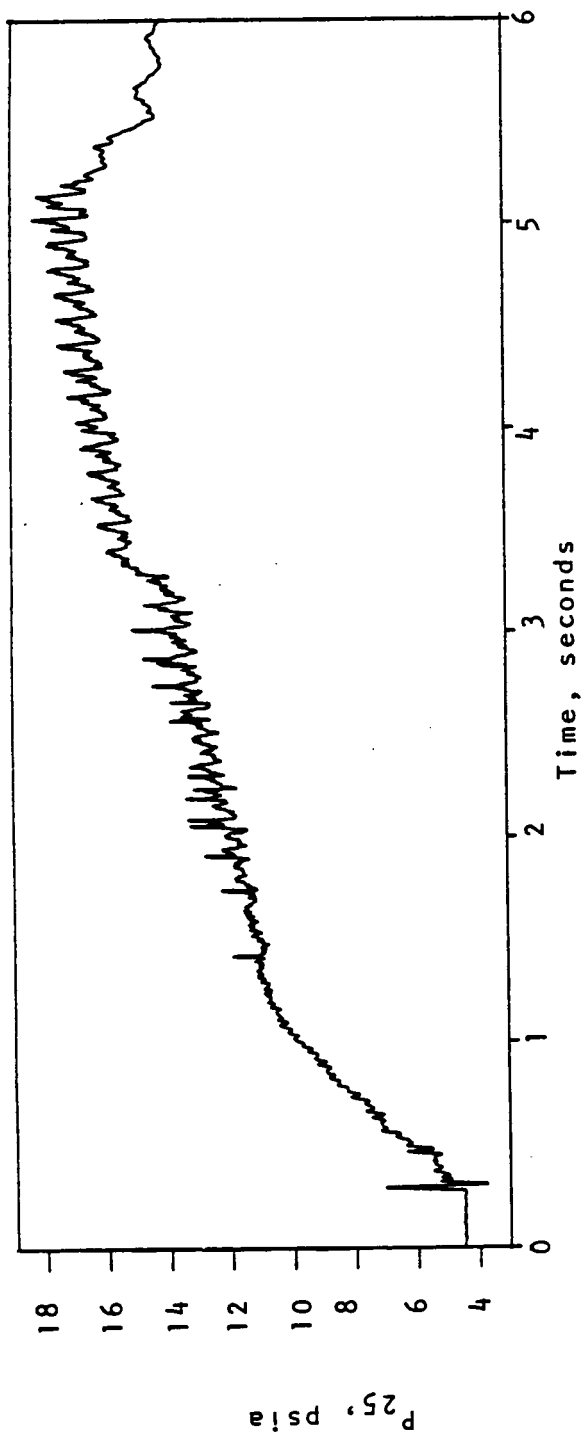


Figure 53. Compressor Inlet Pressure, 95%  $N_c$  Instability.

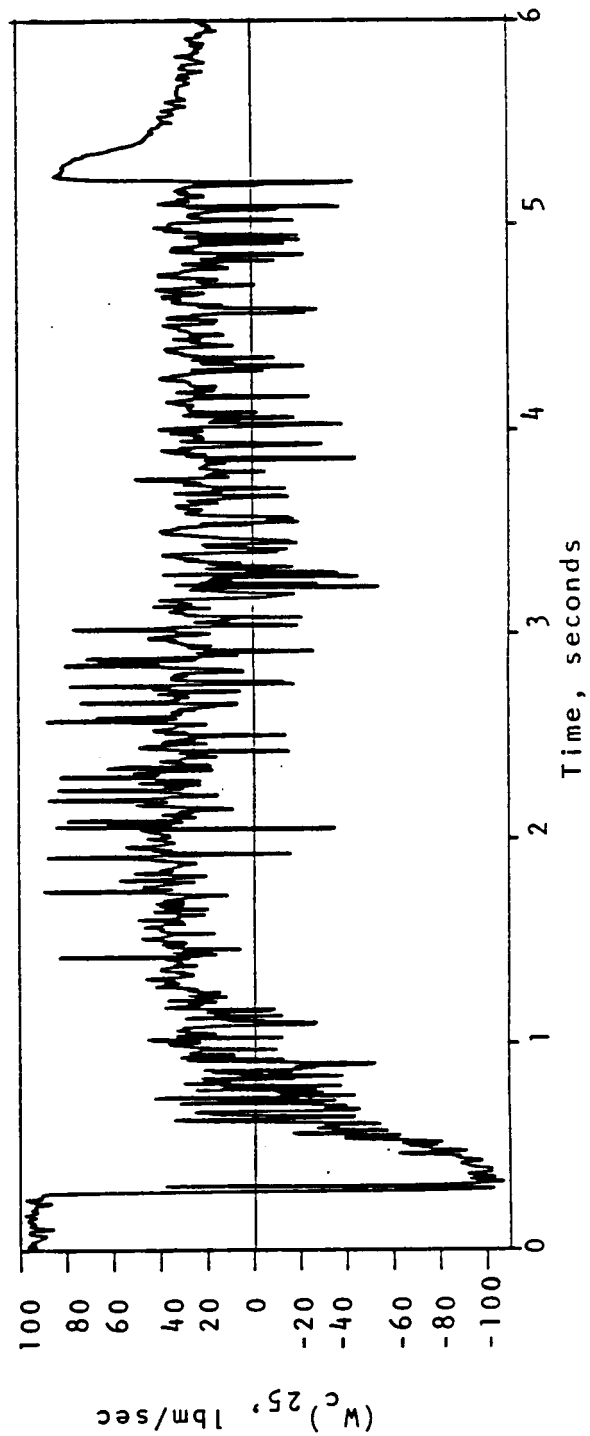


Figure 54. Compressor Inlet Corrected Airflow, 95%  $N_c$  Instability.

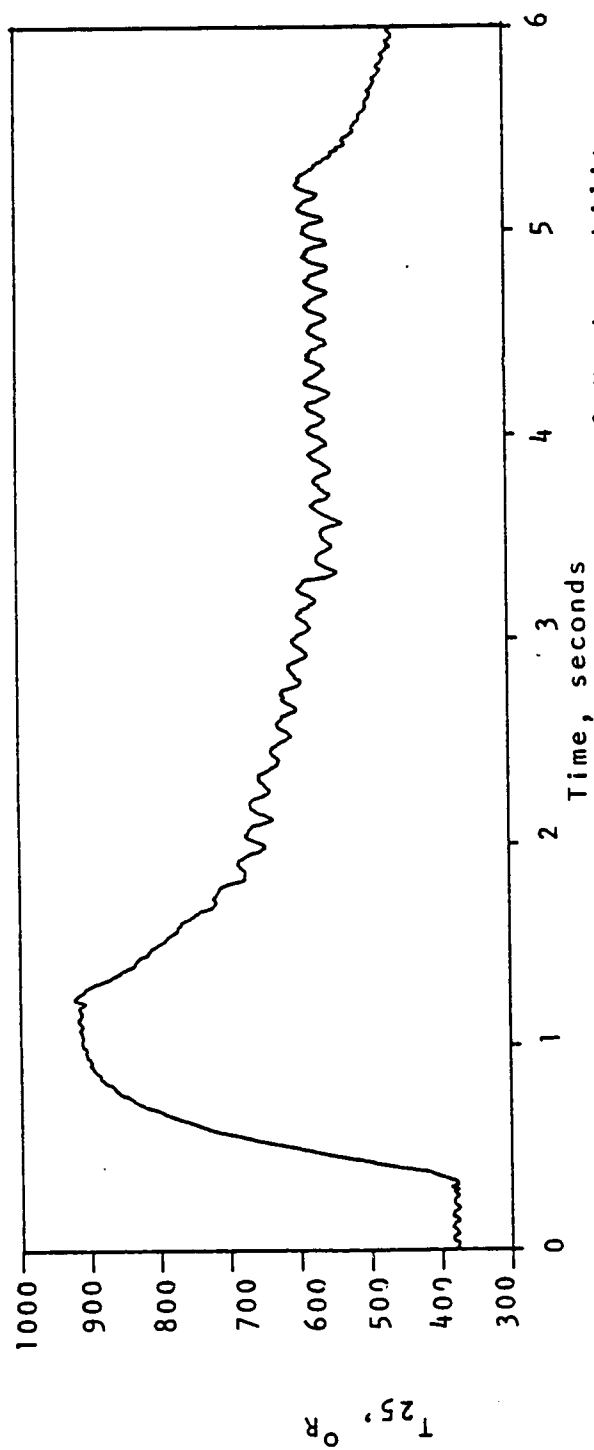


Figure 55. Compressor Inlet Temperature, 95%  $N_c$  Instability.

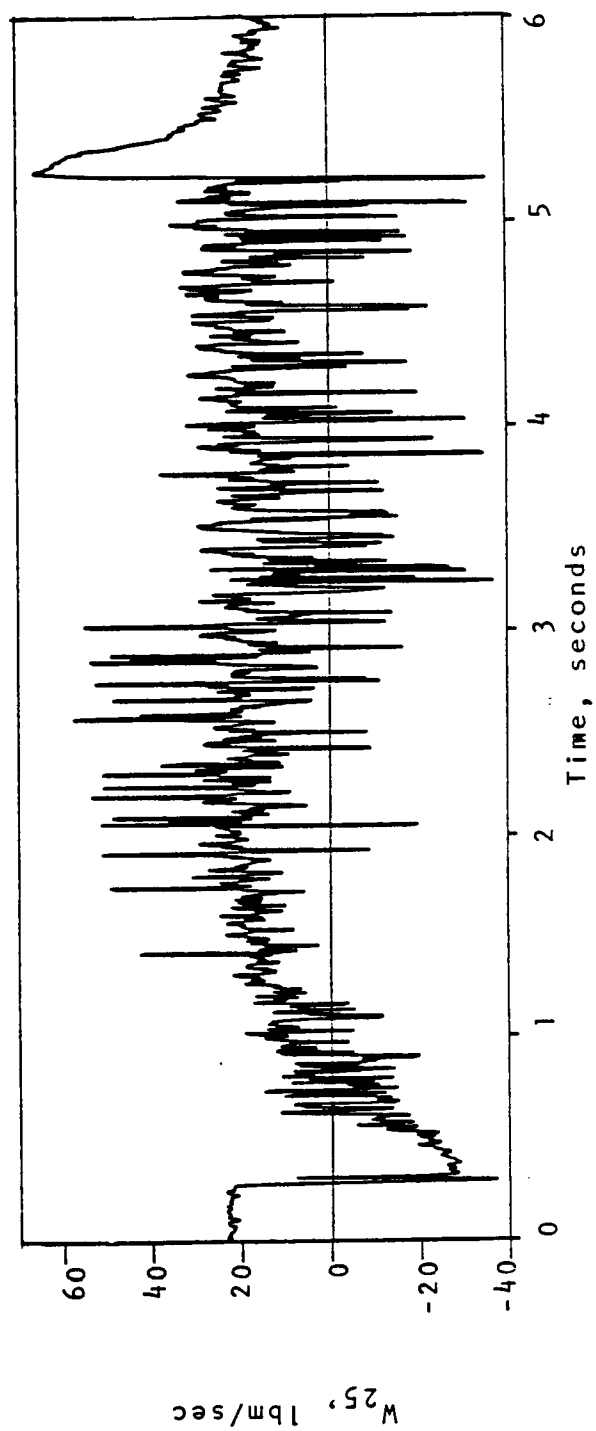


Figure 56. Compressor Inlet Physical Airflow, 95%  $N_c$  Instability.

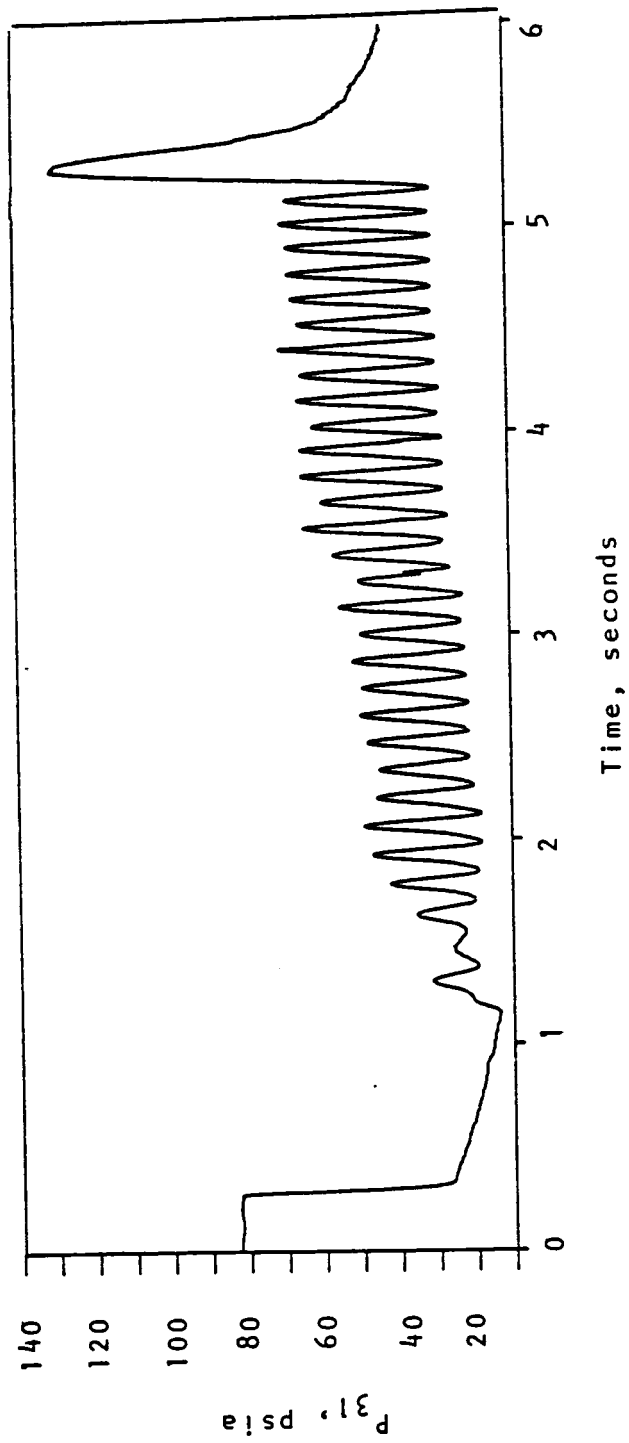


Figure 57. Compressor Exit Pressure, 95%  $N_c$  Instability.

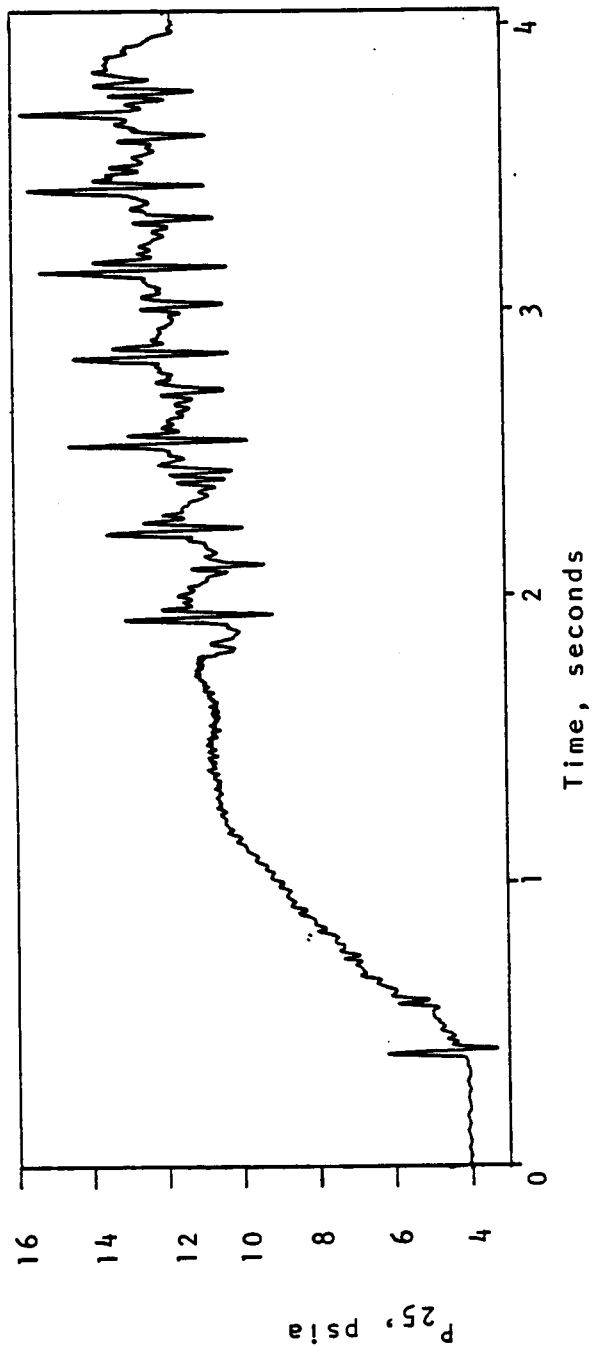


Figure 58. Compressor Inlet Pressure, 95%  $N_c$  Instability, Stators Open  $5^\circ$ .

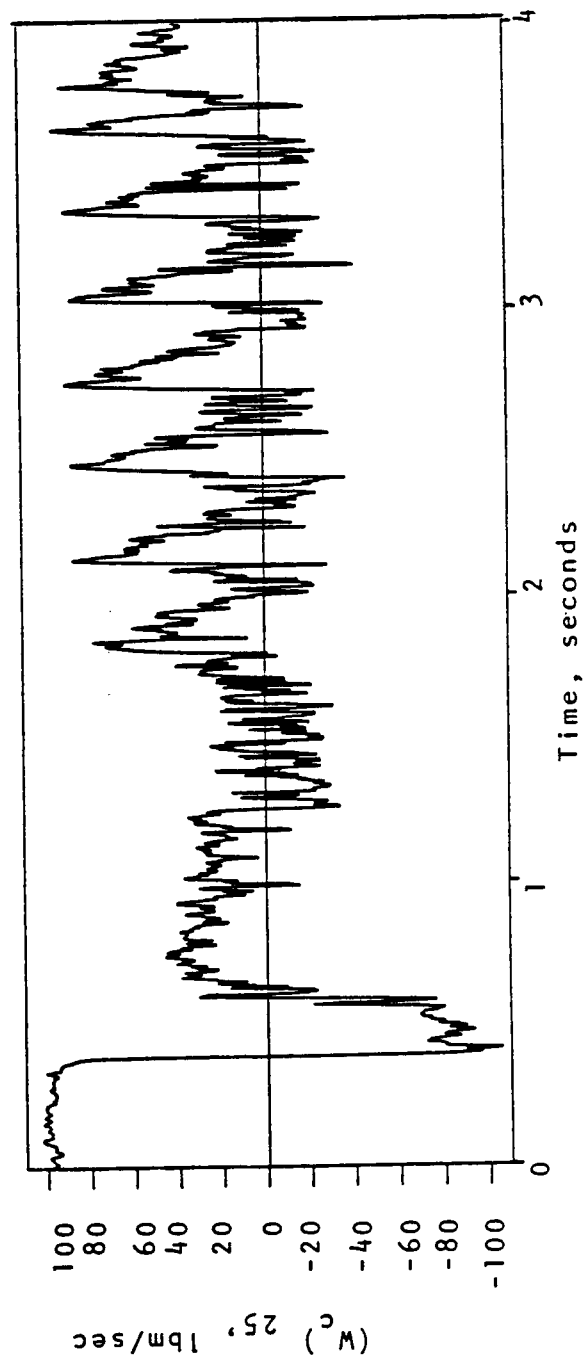
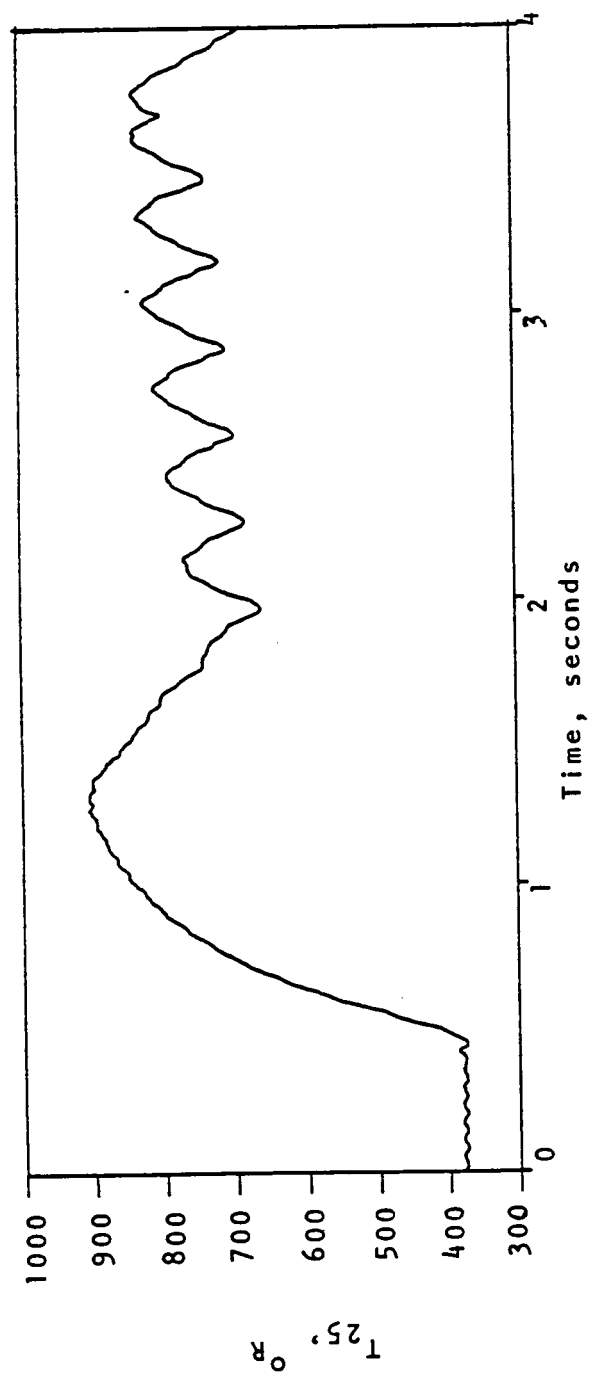


Figure 59. Compressor Inlet Corrected Airflow, 95%  $N_c$  Instability, Stators Open  $5^\circ$ .



82

Figure 60. Compressor Inlet Temperature 95%  $N_c$  Instability, Stators Open  $5^{\circ}$ .

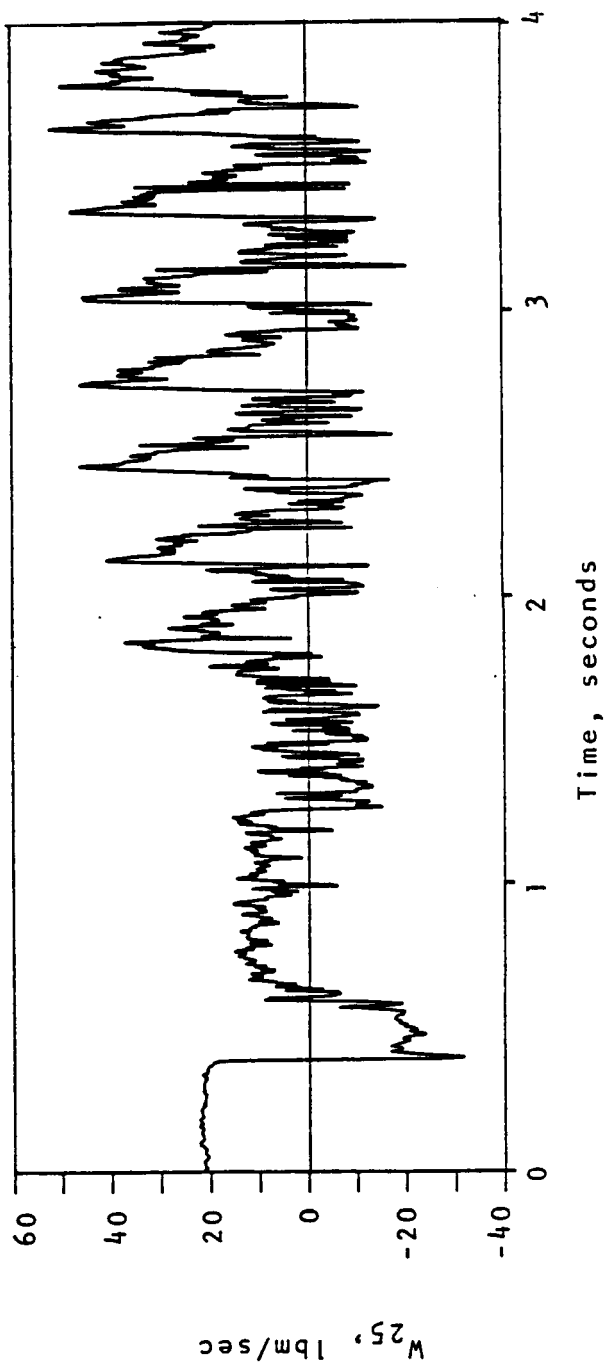


Figure 61. Compressor Inlet Physical Airflow, 95%  $N_c$  Instability, Stators Open  $5^{\circ}$ .

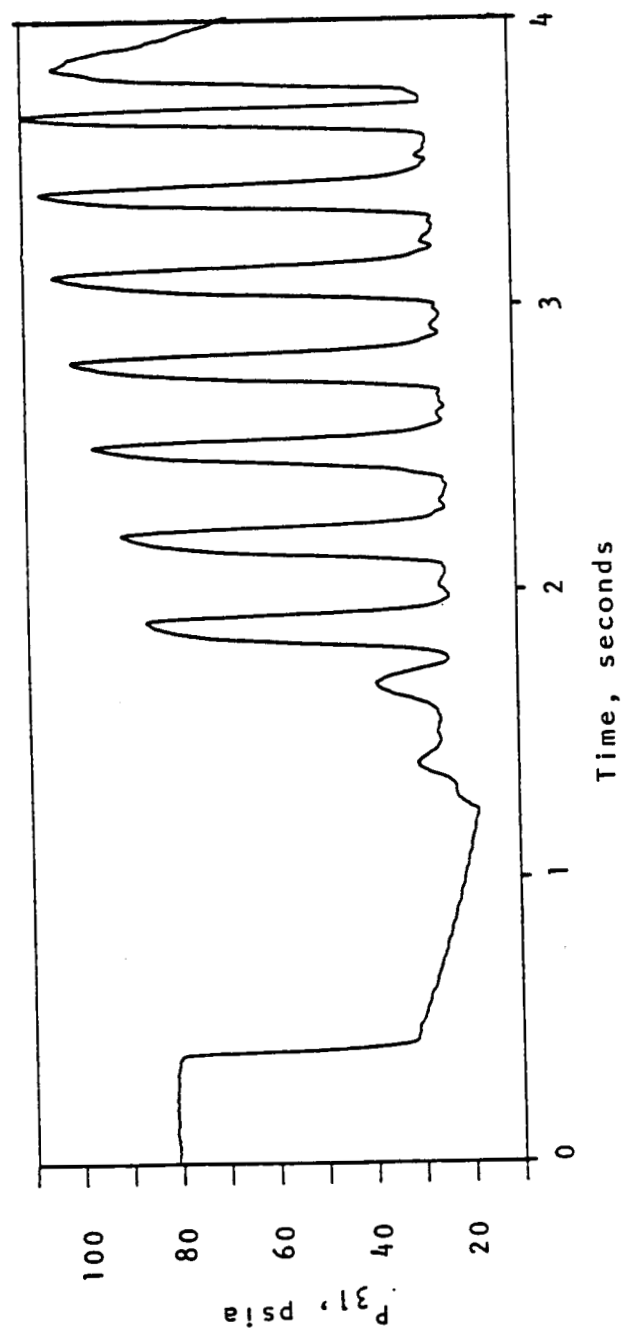


Figure 62. Compressor Exit Pressure, 95%  $N_c$  Instability, Stators Open 5°.

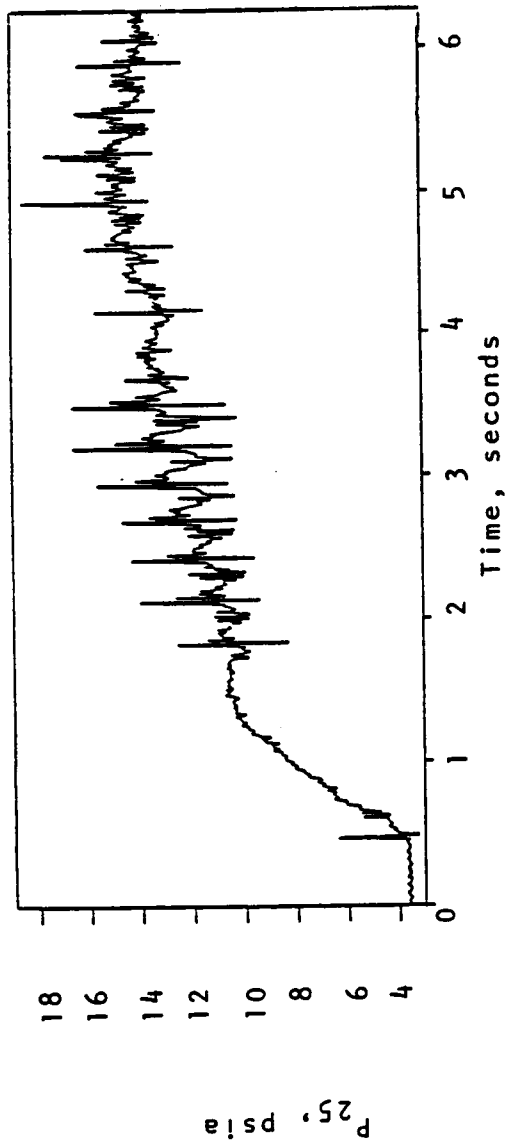


Figure 63. Compressor Inlet Pressure, 98.5%  $N_c$  Instability.

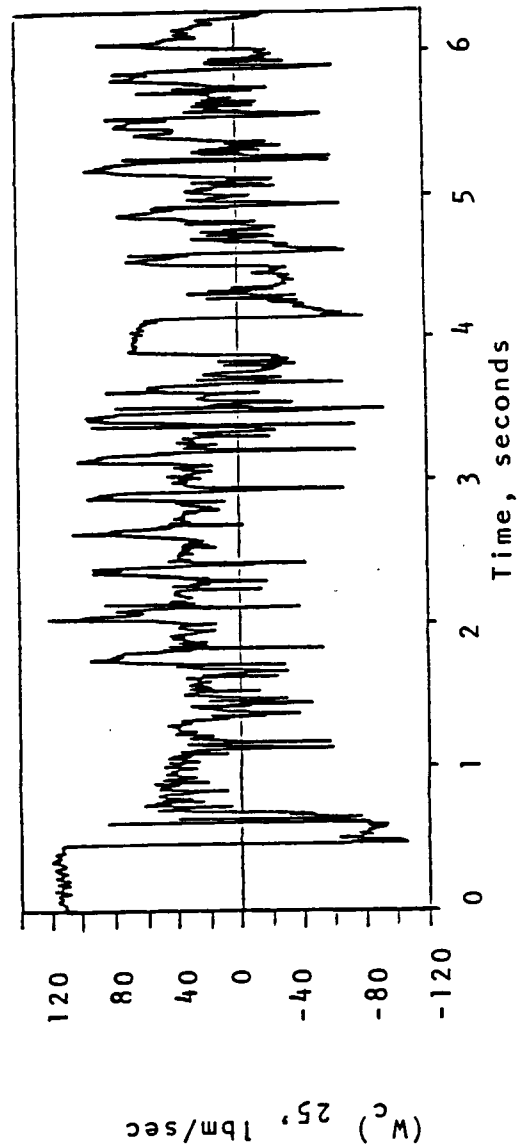


Figure 64. Compressor Inlet Corrected Airflow, 98.5%  $N_c$  Instability.

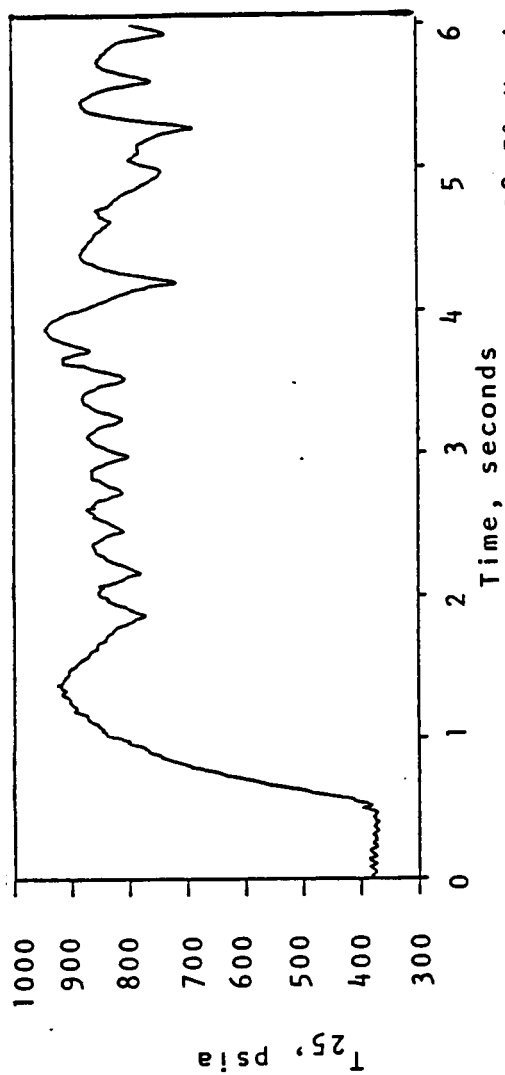


Figure 65. Compressor Inlet Temperature, 98.5%  $N_c$  Instability.

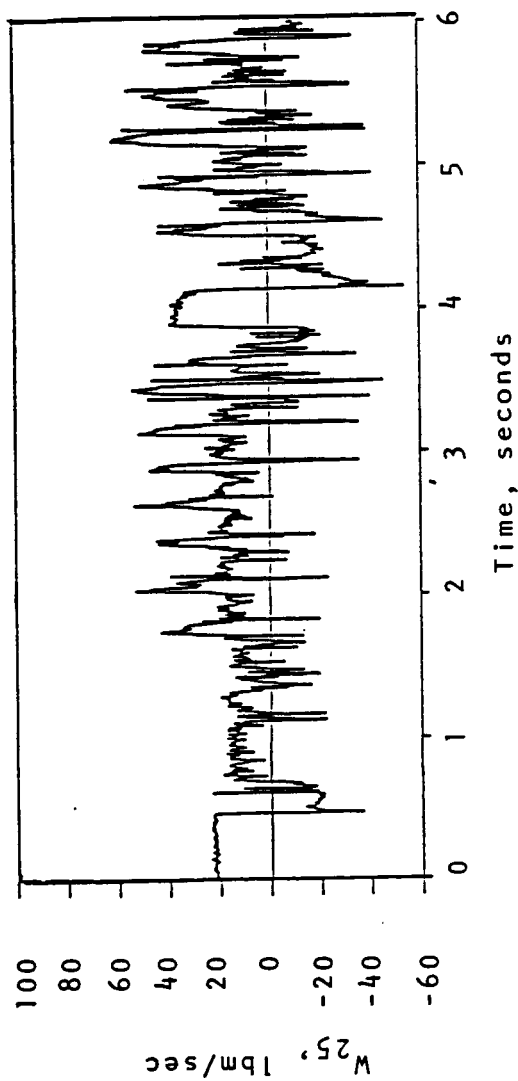


Figure 66. Compressor Inlet Physical Airflow, 98.5%  $N_c$  Instability.

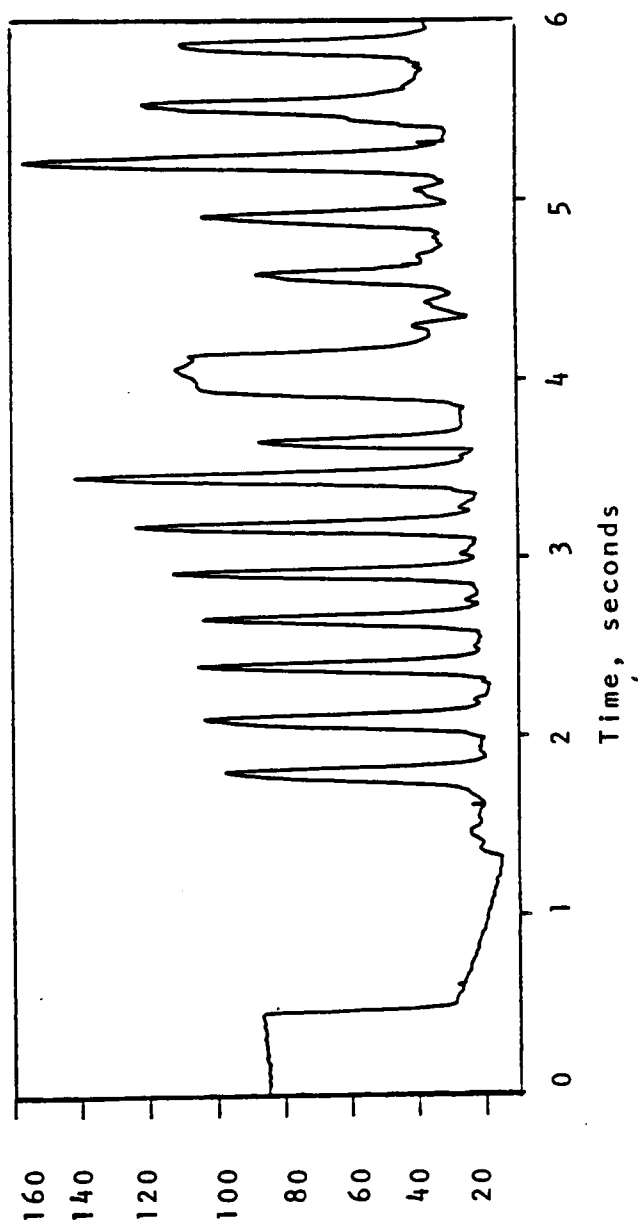


Figure 67. Compressor Exit Pressure, 98.5%  $N_c$  Instability.

## REFERENCES

1. Hosny, W. M., Lenhardt, C. H., Lin, H. T., Lovell, R. C., Steenken, W. G., "Energy Efficient Engine (ICLS/10C) High Pressure Compressor Component Performance Report", NASA-Lewis Research Center, NASA CR-174955, August 1985.
2. Greitzer, E. M., "Surge and Rotating Stall in Axial Flow Compressors. Part 1: Theoretical Compression System Model," ASME Paper No. 75-GT-9, November 1974.
3. Astrom, K. J., "Maximum Likelihood and Prediction Error Methods", Automatic 16, pp 551-574, 1980.
4. Weislander, J., "IDPAC Commands - User's Guide", Report TFRT-3157, Dept. of Automatic Control, Lund Institute of Technology, Lund, Sweden, 1976.
5. Nunes, K. B. Rock, S. M., Identification of Quasi-Steady Compressor Characteristics from Transient Data", NASA-Lewis Research Center, NASA CR-174685, September 1984.
6. Greitzer, E. M., Moore, F. K., "A Theory of Post-Stall Transients in Axial Compression Systems: Part II - Application", ASME Paper No. 85-GT-172, March 1985.

## Distribution

### Government Agencies

NASA Headquarters  
600 Independence Avenue, SW  
Washington, DC 20546

Attn: R/R. S. Colladay  
RJ/C. C. Rosen  
RP/J. R. Facey  
RS/L. A. Harris

NASA Lewis Research Center  
21000 Brookpark Road  
Cleveland, OH 44135

Attn: J. A. Ziemianski	MS 86-1
F. J. Kutina	MS 86-1
C. C. Ciepluch	MS 77-10
P. G. Batterton	MS 86-1
G. K. Sievers	MS 86-7
M. J. Hartmann	MS 3-7
L. J. Kiraly	MS 23-3
J. F. Groeneweg	MS 86-7
J. C. Williams	MS 500-211
A. J. Strazisar	MS 5-11
R. W. Niedzwiecki	MS 77-6
R. G. Willoh	MS 100-5
J. J. Reinmann	MS 77-10
L. J. Bober	MS 86-7
A. G. Powers	MS 86-4
J. J. Coy	MS 86-4
R. E. Coltrin	MS 77-10
C. L. Ball	MS 77-6
E. A. Willis	MS 86-1
E. J. Graber	MS 86-7
L. Reid	MS 77-10
E. T. Meleason	MS 77-10
D. A. Sagerser	MS 77-10
R. D. Hager	MS 86-7 (10 copies)
Library	MS 60-3 ( 2 copies)
Report Control Office	MS 60-1
Tech. Utilization Office	MS 7-3
J. R. Mihalow	MS 77-8
AFSC Liaison Office	MS 501-3
Army R & T Propulsion Lab	MS 77-12

NASA Ames Research Center  
Moffett Field, CA 94035

Attn: R. P. Bencze MS 227-6  
R. C. Smith MS 227-6

NASA Langley Research Center  
Hampton, VA 23665

Attn: C. Driver MS 352  
D. G. Stephens MS 462  
L. J. Williams MS 286

NASA Scientific and Technical Information Facility  
P.O. Box 8757  
B.W.I. Airport, MD 21240  
Attn: Accession Dept. (20 copies)

NASA Dryden Flight Research Center  
P.O. Box 273  
Edwards, CA 93523  
Attn: D-OP/R. S. Baron

Department of Defense  
Washington, DC 20301  
Attn: R. Standahar, 3D1089 Pentagon

Wright-Patterson Air Force Base  
Dayton, OH 45433  
Attn: AFWAL/PO/Col. J. Radloff  
AFWAL/POTA/M. F. Schmidt  
AFWAL/POT/H. I. Bush  
ASD/EN/Col. L. G. vanPelt  
ADS/SR/K. I. Collier

Eustis Directorate  
U. S. Army Air Mobility  
R & D Laboratory  
Fort Eustis, VA 23604  
Attn: J. White  
J. Gomez, Jr.

Navy Department  
Naval Air Systems Command  
Arlington, VA 20360  
Attn: G. Derderian, AIR-310-E

Naval Air Propulsion Test Center  
Trenton, NJ 08628  
Attn: P. J. Mangione, MSPE-32  
R. Valeri, MSPE-34

U. S. Naval Air Test Center  
Code SY-53  
Patuxent River, MD 20670  
Attn: E. A. Lynch

USAVRAD Command  
P.O. Box 209  
St. Louis, MO 63166  
Attn: R. M. Titus

Department of Transportation  
NASA/DOT Joint Office of Noise Abatement  
Washington, DC 20590  
Attn: C. Foster

Federal Aviation Administration  
Noise Abatement Division  
Washington, DC 20590  
Attn: E. Sellman, AEE-120

## Engine Manufacturers

AVCO Lycoming  
550 S. Main Street  
Stratford, CT 06497  
Attn: H. Moellmann

Detroit Diesel/Allison Division  
P.O. Box 894  
Indianapolis, IN 46206  
Attn: B. Wallace

Detroit Diesel/Allison Division  
333 West First Street  
Dayton, OH 45402  
Attn: F. H. Walters

Garrett Turbine Engine Company  
111 South 34th Street  
P.O. Box 5217  
Phoenix, AZ 85010  
Attn: R. Heldenbrand

Garrett Turbine Engine Company  
Torrance, CA 90509  
Attn: F. E. Faulkner

Garrett Turbine Engine Company  
1 First National Plaza  
Suite 1910  
Dayton, OH 45402

General Electric Company/AEG  
1 Neumann Way  
Evendale, OH 45215  
Attn: K. W. Schuning  
T. F. Donohue

General Electric Company/AEG  
1000 Western Avenue  
Lynn, MA 01910  
Attn: R. E. Neitzel

Pratt & Whitney Aircraft Group  
United Technologies Corporation  
Engineering Division  
400 Main Street  
East Hartford, CT 06108  
Attn: W. Gardner  
I. Mendelson  
C. Reynolds

Pratt & Whitney Aircraft Group  
United Technologies Corporation  
Military Products Division  
P.O. Box 2691  
West Palm Beach, FL 33402  
Attn: R. E. Davis

Pratt & Whitney Aircraft Group  
United Technologies Corporation  
23500 Center Ridge Road  
Suite 280  
Westlake, OH 44145  
Attn: A. Leiser

Teledyne CAE, Turbine Engines  
1330 Laskey Road  
Toledo, OH 43612  
Attn: R. H. Gaylord

Williams International  
2280 West Maple Road  
Walled Lake, MI 48088  
Attn: R. vanNimwegen  
R. Horn

#### Airframe Manufacturers

Boeing Aerospace Company  
P.O. Box 3999  
Seattle, WA 98124  
Attn: D. S. Miller  
H. Higgins

MS 40-26

Boeing Commercial Airplane Company  
P.O. Box 3707  
Seattle, WA 98124  
Attn: Dr. C. G. Hodge  
J. Farrell

Boeing Company  
Wichita Division  
P.O. Box 7730  
Wichita, KS 67277  
Attn: D. Tarkelson

Douglas Aircraft Company  
McDonnell Douglas Corporation  
3855 Lakewood Boulevard  
Long Beach, CA 90846  
Attn: R. T. Kawai  
M. Klotzsche

Gates Learjet Corporation  
P.O. Box 7707  
Wichita, KS 67277  
Attn: E. Schiller

General Dynamics Convair  
P.O. Box 80844  
San Diego, CA 92138  
Attn: S. Campbell

Grumman Aerospace Corporation  
South Oyster Bay Road  
Bethpage, NY 11714  
Attn: N. F. Dannenhoffer

Lockheed-California Company  
Burbank, CA 91502  
Attn: J. F. Stroud  
R. Tullis

D/75-42  
D/75-21

Lockheed-Georgia Company  
86 S. Cobb Drive  
Marietta, GA 30063  
Attn: W. E. Arndt

D/72-17, Zone 418

McDonnell Aircraft Company  
McDonnell Douglas Corporation  
P.O. Box 516  
St. Louis, MO 63166  
Attn: G. Phariss

Rockwell International  
International Airport  
Los Angeles Division  
Los Angeles, CA 90009  
Attn: A. W. Martin

#### Airlines

American Airlines  
Maintenance and Engineering Center  
Tulsa, OK 74151  
Attn: C. Wellmershauser

Delta Airlines, Inc.  
Hartsfield-Atlanta International Airport  
Atlanta, GA 30320  
Attn: J. T. Davis

Eastern Airlines  
International Airport  
Miami, FL 33148  
Attn: E. Upton

Pam American World Airways, Inc.  
JFK International Airport  
Jamaica, NY 11430  
Attn: R. Valeika

Trans World Airlines  
605 Third Avenue  
New York, NY 10016  
Attn: K. Johnson

United Airlines  
Maintenance Operations Center  
San Francisco International Airport  
San Francisco, CA 94128  
Attn: J. Goodwine

Others

Aerospace Corporation  
R & D Center  
Los Angeles, CA 90045  
Attn: Library

Brunswick Corporation  
2000 Brunswick Lane  
Deland, FL 32720  
Attn: A. Erickson

Drexel University  
College of Engineering  
Philadelphia, PA 19104  
Attn: A. M. Mellor

Fluidyne Engineering Corporation  
5900 Olson Memorial Highway  
Minneapolis, MN 55422  
Attn: J. S. Holdhusen

Hamilton Standard  
United Aircraft Corporation  
Windsor Locks, CT 06096  
Attn: B. Gatzen

MS 1-2-11

International Harvester  
Solar Division  
2200 Pacific Highway  
San Diego, CA 92112  
Attn: Library

Massachusetts Institute of Technology  
Department of Astronautics and Aeronautics  
Cambridge, MA 02139  
Attn: Library

Massachusetts Institute of Technology  
Department of Structural Mechanics  
Cambridge, MA 02139  
Attn: J. Mar  
A. Epstein

Penn State University  
Department of Aerospace Engineering  
233 Hammond Building  
University Park, PA 16802  
Attn: Dr. B. Lakshminarayana


Rohr Corporation  
P.O. Box 878  
Foot and H Street  
Chula Vista, CA 92012  
Attn: Library

TRW, Inc.  
TRW Equipment Group  
23555 Euclid Avenue  
Cleveland, OH 44117  
Attn: I. Toth

University of Michigan  
Gas Dynamics Laboratories  
Aerospace Engineering Building  
Ann Arbor, MI 48109  
Attn: Dr. C.W. Kaufmann

University of Tennessee Space Institute  
Tullahoma, TN 37388  
Attn: Dr. V. Smith

Westinghouse Electric Corporation  
P.O. Box 5837  
Beulah Road  
Pittsburgh, PA 15236  
Attn: Library

1. Report No. CR 179521		2. Government Accession No.		3. Recipient's Catalog No.	
4. Title and Subtitle E <sup>3</sup> 10C Compressor Test Analysis of High-Speed Post-Stall Data				5. Report Date October 1986	
				6. Performing Organization Code 535-03-01	
7. Author(s) S. D. Dvorak, W. M. Hosny, W. G. Steenken				8. Performing Organization Report No. R86 AEB	
				10. Work Unit No.	
9. Performing Organization Name and Address General Electric Company Aircraft Engine Business Group Cincinnati, OH 45215				11. Contract or Grant No. NAS3-24211	
				13. Type of Report and Period Covered Topical	
12. Sponsoring Agency Name and Address NASA Lewis Research Center Cleveland, OH 44135				14. Sponsoring Agency Code	
15. Supplementary Notes					
16. Abstract The objective of this program was to determine in-stall characteristics from high-speed post-stall transients. The transient, surge-cycle nature of high-speed post-stall operation precludes the possibility of obtaining in-stall characteristics in a steady-state manner, as is possible during low-speed post-stall operation, which is characterized by quasi-steady rotating-stall behavior. For this reason, maximum likelihood parameter estimation techniques were used to obtain the quasi-steady high-speed characteristics from transient data. This involved, first of all, obtaining the necessary data from a specially instrumented compressor that was tested well beyond its limits of normal operation. The unsteady, post-stall data thus obtained was then digitized and processed through a simplified analytical model to construct the input-output relationship necessary for estimation. The in-stall characteristics were determined using this estimation procedure at two different high-speed conditions, 90 and 98.5 percent corrected speed. The estimated characteristics were found to be robust in the presence of measurement noise and unmodelled system dynamics, but the compressor response-time constants, which were also estimated, were more sensitive to these same disturbances. The experimentally determined low-speed in-stall characteristics and the estimated high-speed in-stall characteristics were then incorporated into a one-dimensional compressor simulation model developed as a parallel effort to the compressor testing and data reduction effort. The results of this model yielded predictable results consistent with its level of sophistication.					
17. Key Words (Suggested by Author(s)) High Pressure Ratio Compressor In-Install Data Compressor Model Development			18. Distribution Statement 		
19. Security Classif. (of this report) Unclassified		20. Security Classif. (of this page) Unclassified		21. No. of pages 87	
22. Price*					